2022

Lipid bilayer phase separations, cholesterol, and their effect on the amyloid precursor protein C99

BOSTON UNIVERSITY

GRADUATE SCHOOL OF ARTS AND SCIENCES

Dissertation

LIPID BILAYER PHASE SEPARATIONS, CHOLESTEROL, AND THEIR EFFECT ON THE AMYLOID PRECURSOR PROTEIN C99

by

GEORGE A. PANTELOPULOS

A.S., Community College of Philadelphia, 2013
B.S., Temple University, 2015

Submitted in partial fulfillment of the

requirements for the degree of

Doctor of Philosophy

2022

Approved by

First Reader

John E. Straub, PhD
Professor of Chemistry

Second Reader

Qiang Cui, PhD
Professor of Chemistry

Third Reader

David F. Coker, PhD
Professor of Chemistry

Fourth Reader

Karen N. Allen PhD
Professor of Chemistry

Dedication

I dedicate this thesis to George Leoutsacos Lewis (1911-1997), my maternal *papou*.[1] Stories of his papou's life have served as my foundational example of a self-actualized person. His career success as scientist is evidenced in many awards such as his election as an AAAS fellow for his work at the DuPont Experimental Station. Prideful and funny stories about the intersection of papou's life with famous scientists allowed me to feel connected to the whole of scientific history.[2] It was the balance of papou's career success with the use of his earnings from wages and patents to pay for the University education of his siblings, activism and financial support for human rights with organizations such as the NAACP, and his general respect and love for all humans. Though the conditions of America and it's institutions have changed substantially from papou's time, I aspire to live life in a similar fashion to his own. As such, I also dedicate of my life to joyful and novel scientific pursuits along with contributions toward the self-actualization of each person.

[1] *Papou* is a greek word for "grandfather."

[2] Stories such as Linus Pauling (who I believe he knew from his work on polymer chemistry and chemical physics at DuPont) visiting his family and extolling the wonderous health benefits of taking Vitamin C, or the time he quite literally ran into Albert Einstein at Princeton and was chided for running through the hallways.

[The] crippling of individuals I consider the worst evil of capitalism.
Our whole educational system suffers from this evil.

An exaggerated competitive attitude is inculcated into the student,
who is trained to worship acquisitive success
as a preparation for his future career.

Albert Einstein

Acknowledgments

I thank my mom, Daphne Pantelopulos, for regaling me with many stories about my *papou*, George Leoutsacos Lewis, when I was growing up. I thank both my dad, Anthony Pantelopulos, and my mom for their sincere support of all of my academic pursuits, and for the example of his incredible patience. I thank my mom for the examples of her curiosity and openness, which inspired the development of my scientific personality. I thank my *yiayia* and *theia* Georgia for their love and support growing up. May they rest in peace. I thank my older brother Anastasios, who served as my second-greatest inspiration growing up. His dedication to truth, justice, and communication were essential to my development. I also thank John Kollias, a critical member of the local Greek community who spent much of his time engaging the inquisitive youth in discussions of history, politics, and philosophy up to his passing. There are many people who I must thank from my time an undergraduate student in Philadelphia. I would like to thank philosophy professor Hank Dmochowski and retired actuary Frank Murphy, who took me under their wings when I was a student at the Community College of Philadelphia. Hank's effortless application of the Socratic Method in live discussion with students in his Ethics course was inspirational. Likewise my time spent with Frank also built self-esteem in math, though we spent most of our time talking about classical and medieval history. It is also thanks to them that I gained the confidence to go into science despite a half-finished high school education.

I thank professor John Snyder for selecting me out of hundreds of applicants to the BU Chemistry NSF REU program, which was my first chance to enter a chemistry lab and participate in research. I thank professor Ramesh Jasti, who allowed me to work in his group that summer. I give great thanks to professor Vincent Voelz of Temple Unviersity, who provided me more time and attention than anyone could ask

for from an undergraduate research advisor, and the rest of the Voelz group for their companionship. I thank professor Andrew Price for his excellent Inorganic Chemistry course in which I and my fiancée Chung Tran met. I thank Dana Dawson and Samuel Markson for their focused and kind support during the development of my NSF Graduate Research Fellowship proposal, from which I was awarded my first major research fellowship. I thank Tatiana Poladko and Atnre Alleyne for granting me and Chung the chance to teach TeenSHARP students from local public schools over the summer. And of course I thank all Theoretical and Physical Chemistry professors of Chemistry of Temple University, their graduate students, and the department staff.

There are many people I must thank from my time as a graduate student both in Boston and in Japan. First I must thank the three anonymous reviewers who found my application worthy of an NSF Graduate Research Fellowship, which supported three years of graduate research. I give the greatest thanks to my PhD advisor, Professor John E. Straub who supported my application to the Chemistry Department PhD program and my NSF GRFP application. John provided me with a remarkable degree of freedom that fostered the ability to work independently while supplying support via fostering critical group discussions, his extensive knowledge of literature, and his high standards for publishing. Likewise, John provided opportunities to shape the direction of the lab by involving me and other members of the group in the full development and writing process of major research grants for the group, which were successfully funded.

I thank the old and new members of the Straub group with whom I have worked and held many discussions: Qing Lu, Asanga Bandara, Afra Panahi, Ryo Urano, Shanshan Song, Lin Xu, Jonathan Harris, Meera Kumanan, Ayan Majumder, Harrison Reiter, Seulki Kwon, and Conor Abraham. I thank the other Theoretical Chemistry Professors David Coker, Tom Keyes, Ksenia Bravaya, and Qiang Cui and all of the students and post-doctoral scholars who work with them with whom I shared companionship. I thank physics professors Eugene Stanley and Anders Sandvik for courses in graph theory, econophysics, computational physics, and mathematical methods. I also thank professor Karen Allen for serving as the chair of both my PhD advancement and dissertation committees.

In Japan, I thank Dr. Yuji Sugita of RIKEN for his incredible support of my research and participation as a guest of his group. I was very fortunate to first work for six months in Dr. Sugita's group through the support of the NSF GROW program in

collaboration with the JSPS post-doctoral fellowships program. This was followed up in the next year for another six months in the Sugita group via RIKEN as a short-term international program associate, and then, in the following year, six additional weeks as a guest of the Sugita group. I also thank the Japanese Theoretical Chemistry community at-large who I met throughout my time as a guest of the Sugita group. I thank Nagoya University Professors Yuko Okamoto, Susumu Okazaki, Masataka Nagaoka, and Wataru Shinoda for several interesting meetings. I also thank the members of Florence Tama's group at both Nagoya University and RIKEN for many conversations as well. And finally I give a very special thank you to Tetsuro Nagai and his family, with whom I have had the pleasure of both collaboration and friendship since my first summer as a graduate student.

In the Boston area, I give a huge thank you to all of my friends who comprised the "Boston Mojank" Riichi Mahjong group. The near-weekly meetups at our apartment in Central Square were a magical time that I will always cherish. Likewise, I thank my longtime friends from the American Touhou Project community for our mutual friendship and ongoing support for over a decade. And finally, I give my greatest thanks my fiancée Chung Tran for her love and support, and I look forward to our future together.

LIPID BILAYER PHASE SEPARATIONS, CHOLESTEROL, AND THEIR EFFECT ON THE AMYLOID PRECURSOR PROTEIN C99

GEORGE A. PANTELOPULOS

Boston University, Graduate School of Arts and Sciences, 2022

Major Professor: John E. Straub, PhD, Professor of Chemistry

ABSTRACT

The Amyloid Cascade hypothesis provides a molecular-level mechanism for the etiology of Alzheimer's Disease (AD) and proposes a central role for the genesis and aggregation of Aβ protein. Aβ protein is the product of cleavage of the amyloid precursor protein (APP), a single pass transmembrane protein, by secretases and is found in a variety of isoforms, with longer isoforms being linked to the early onset of AD. The isoform distribution is dependent on membrane environment, mutations, and post-translational modifications.

Lipid rafts are characterized by lipids induced into the liquid ordered phase by cholesterol, enhancing membrane thickness and lateral lipid density. Protein preference for rafts can control protein kinetics, and has been implicated in determining whether APP is processed by α– or β-secretase in the plasma membrane. In addition to inducing lipid rafts, cholesterol is hypothesized to directly modulate APP, the C-terminal fragment of APP (C99), and γ-secretase structure and function via direct interaction. To date, the molecular details involved in these fundamental events involved in Aβ genesis have yet to be resolved using experimental approaches, suggesting a critical role for computation.

This thesis presents the results of investigations of lipid phase separation and cholesterol and their effects on C99 using molecular dynamics simulation. To gain insight into the nature of lipid rafts, studies characterizing the simulation system sizes required for observation of phase separation, exploring the effect of cholesterol con-

centration on phase separation and lipid phases, and examining the applicability of different lipid and cholesterol models for the simulation of lipid phases and protein structure were performed. To gain insight into the fundamental properties of C99, studies exploring the structure of full-length C99, the interaction of cholesterol with C99 in various mutational states, the effect of membrane thickness on the C99 extramembrane domains, and the structure of C99 monomer and dimer were performed. Taken together these studies advance our molecular-level understanding of the nature of cholesterol, the role of cholesterol in lipid phase separation, the effect of cholesterol on C99, and the structure of the full-sequence C99 monomer and dimer that play a critical role in the evolution of AD.

Contents

List of Tables

List of Figures

Chapter 1

Introduction

1.1 Amyloid Beta and Alzheimer's Disease

Plaques and neurofibrillary tangles in the brain tissue of Alzheimer's Disease (AD) patients have been implicated in AD since initial observations in demented patients at the turn of the 20th century.[8] These plaques were determined to be principally composed of Aβ protein. Aβ are fragments of the amyloid precursor protein (APP). In 1991 it was proposed that a biochemical cascade starting from APP and ultimately resulting in formation of these Aβ plaques is responsible for the genesis of AD.[9–11] The Amyloid Cascade Hypothesis was proposed when many key details leading to production of Aβ plaques were still undetermined. Since then, the principal protein domains, cellular compartments, and lipid domains involved in the production of Aβ have been identified. Moreover, the composition of plaques have been found to be rather complex, composed of Aβ of various lengths, many post-translational modifications to Aβ, and various extracellular matrix proteins, lipids and cholesterol.[12] Aβ fibrils, the core of Aβ plaques, have been found to adopt many polymorphic fibril structures, determined by various extracellular conditions.[13]

Despite the ultimate genesis of Aβ plaques in many cases of AD, plaques have been found to be unnecessary to the onset of AD.[14] Instead, Aβ oligomers, precursors to Aβ plaques in the amyloid cascade,[15] have been identified as the pathogenic Aβ agent in AD.[16] This Amyloid Oligomer Hypothesis was proposed in 1998, based on the observation that Aβ oligomers reduce nerve cell potentiation, mental plasticity, and ultimately cause neurodegeneration, stated as follows[17]

> "We hypothesize that impaired synaptic plasticity and associated memory dysfunction during early stage Alzheimer's disease and severe cellular degeneration and dementia during end stage could be caused by the biphasic impact of Aβ-derived diffusible ligands acting upon particular neural signal transduction pathways."

Aβ oligomers have since become widely accepted as the Aβ agent responsible for neurogedeneration through thousands of peer-reviewed investigations.[16] There are also many alternative hypotheses of AD that involve Aβ such as the Inflammation Hypothesis, in which microglia (neural macrophages) induce inflammation upon sequestering Aβ plaques which leads to tissue damage,[18,19] and the Oxidative Stress Hypothesis, in which Aβ-copper interaction produces reactive oxygen species, inducing cellular oxidative stress.[20] There is also recent work evidencing that Aβ aggregates on the surface of membranes[21] and can fibrilize and potentially rupture the membrane,[22–24] or can oligomerize to form ion channels and disrupt ion homeostasis.[25–27]

Of alternative AD hypotheses, the Tau Hypothesis is most prominent. Tau protein fibers form the microtubules of axons, the junctions between neurons. Hyperphosphorylation of Tau protein causes formation of disordered neurofibrillary tangles observed in AD patients, which disrupt axon structure and thus the connection of neurons, directly leading to neurodegeneration.[28] Hyperphosphorylation of Tau has also been directly connected to Aβ oligomers, and it may be that the amyloid and Tau disease pathways are synergistic.[29,30] There is also evidence to suggest that brain insulin deficiency, such in diabetes, may trigger hyperphosphorylation of Tau and reduce clearance of Aβ aggregates.[31–33]

Aβ comes in isoforms of various length. The 40-residue isoform, Aβ_{40}, is the most common, followed by Aβ_{42}, and then various other isomers in much smaller proportion between 33 and 49 residues in length.[12] Aβ_{42} came to be regarded as a more toxic isomer than Aβ_{40} because the ratio of Aβ_{42}/Aβ_{40} is substantially enhanced in individuals who have hereditary mutations that manifest AD, so-called Familial Alzheimer's Disease (FAD) mutations.[34–36] Aβ_{42} is more prone to oligomerization and fibrillization due to the enhanced stabilization of β-sheets by residues 41 and 42.[37] Furthermore, FAD mutations in Aβ enhance aggregation.[38] Therefore, there has been much interest in determining how Aβ isomers of different lengths are produced. This requires understanding the amyloid cascade up to the point at which Aβ is secreted from the cell.

1.2 Proteins of the Amyloid Cascade

We will first approach the amyloid cascade through discussion of the protein signaling cascade that results in the production of Aβ. This begins with the amyloid precursor

protein (APP), canonically a 770-residue protein evidenced to perform many functions including cell-cell signaling for synaptogenesis, regulation of copper, sphingomyelin and cholesterol homeostasis, and promotion of extracellular matrix development.[39] Residues 1-671 of APP are evidenced to mostly consist of intrinsically disordered domains separating two spectroscopically-resolved structured domains, E1 (residues 28-189)[40,41] and E2 (374-565)[42,43], and a single-pass transmembrane (TM) domain in residues 699-724 (Figure 1·1.A).[44] The sequence of Aβ_{42} is contained in residues 672 to 713. APP is canonically processed near the TM domain by two separate secretases, α- or β-secretase, each from the ADAM and BACE sheddase protein families and predominantly performed by ADAM10[45,46] and BACE1,[47,48] respectively. Alternative APP processing can occur in ectodomain[49], endodomain[50], and Aβ domain[51] residues, but potential roles of these proteolyses in AD genesis are unclear.

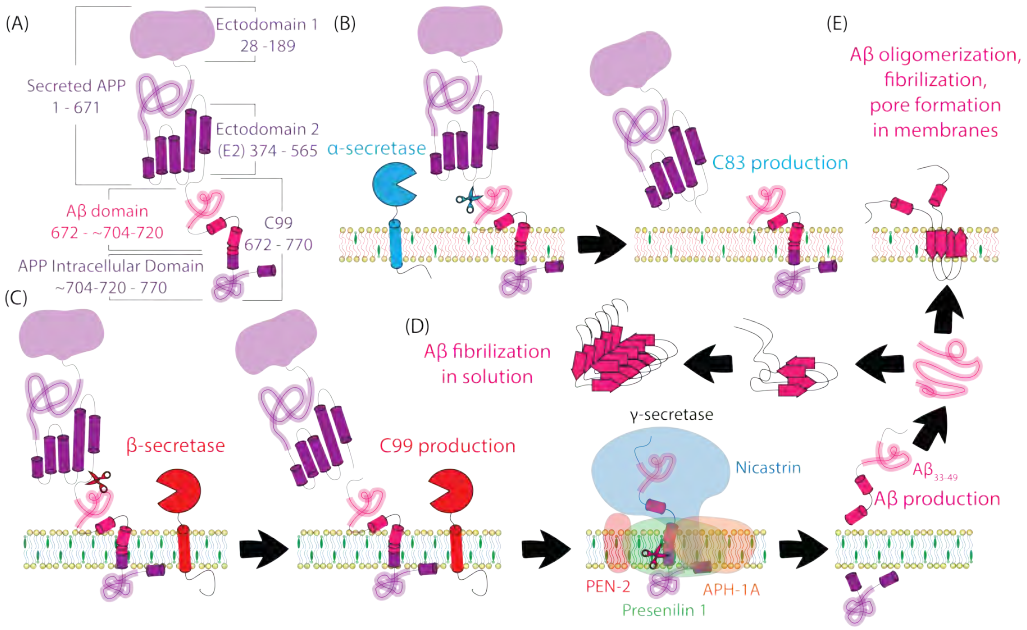

Figure 1·1: Cartoon illustrations of (A) domains of the APP protein, (B) the complementary pathway up to production of C83, (C) the amyloid pathway including production of C99 and Aβ, (D) the termination of the amyloid cascade in formation of Aβ fibrils, (E) the termination of the amyloid cascade in formation of Aβ aggregates on the membrane surface. APP, ADAM10, and BACE1 are represented in purple, blue, and red. Aβ is displayed in pink. The γ-secretase complex nicastrin, PEN-2, APH-1A, and presenilin 1 domains displayed in blue, pink, orange, and green. L_o (liquid ordered) domains represented with blue, ordered saturated lipid tails and a higher concentration of cholesterol, L_d (liquid disordered) domains represented with red, disordered unsaturated lipid tails and a lower concentration of cholesterol.

ADAM10 performs "α-cleavage" on APP at residue 687, producing secreted APP α (sAPPα) and the 83-residue TM protein C83 from the remaining 83 C-terminal residues of APP. C83 does not contain residues 1-16 of Aβ, and thus cleavage of APP by α-secretase ends the amyloid pathway, and instead proceeds along the complementary pathway (Figure 1·1.B).[52] BACE1 performs "β-cleavage" on APP at residue 672, producing secreted APP β (sAPPβ) and the 99-residue TM protein C99, which contains the Aβ sequence starting from residue 1, and which has a juxtamembrane and C-terminal helix which have been resolved via NMR (Figure 1·1.C).[5,7,53] C99 is encapsulated by the multi-pass transmembrane protein complex γ-secretase, which performs a multi-step cleavage to produce Aβ. γ-secretase is composed of presenilin 1 (PS1), presenilin enhancer 2 (PEN-2), anterior pharynx-defective 1A (APH-1A) transmembrane proteins and the ectodomain protein nicastrin (NCT).[54] Residues Asp257 and Asp385 of PS1 catalyze proteolysis of the C99 TMD every 3- or 4-residues up the sequence until release of the product Aβ. This process starts at the membrane-solution interface at residue 48 or 49, the C-terminal end of the C99 transmembrane domain. Aβ of 49 down to 33 residues in length can be produced from this cleavage, though Aβ_{40} is the principal product, at approximately 85% product.[55] The produced Aβ can terminate the amyloid cascade by formation of fibrils and oligomers in solution or, potentially, in membrane (Figure 1·1.D,E).

These proteins have multiple other known functions aside from proteolysis of APP. ADAM10 is known not only to proteolyze C99, but many other proteins.[56] Mouse knockout experiments have shown that ADAM10 is required for cell viability.[57] A notable example among critically-important proteins processed by ADAM10 is Notch protein, which performs essential roles in signaling for cell differentiation, proliferation, and apoptosis.[58] BACE1 is known to be particularly important for healthy axon myelination, potentially causing various mental disorders, though BACE1 knockout mice are viable and can reproduce.[59,60] γ-secretase is also know to be essential in many functions, acting as a acting as an enzyme for over 90 protein substrates, among which is Notch.[61] Much like ADAM10, γ-secretase PS1 domain knockout mice are not viable.[62] The many and diverse critically important functions of these proteins has made development of drugs to prevent progression of AD via modulation of Aβ production challenging.[63]

Familial Alzheimer's Disease mutations, which cause early-onset AD (onset at under 65 years of age), occur in APP, PS1, and presinilin 2 (PS2), a homologue of PS1.[64]

Mutations to ADAM10 can attenuate APP processing and potentially lead to late-onset AD.[65] It is not yet known if there are BACE1 mutations that affect AD.[66] In APP most FAD mutations appear in the C99 domain near the β-secretase cleavage site, the copper binding site (important for copper reduction), the α-secretase cleavage site, and the γ-secretase cleavage site.[67,68] There are many FAD mutations to the PS1 domain of γ-secretase as well, though these mutants are located in various locations in PS1 such that it is more difficult to imagine the biophysical mechanism by which they modulate Aβ production.[69]

Mutations to APP in the C99 domain can affect the localization of APP to different subcellular compartments, ultimately affecting the propensities for α- or β-cleavage.[70] The localization and propensity for APP, ADAM10, BACE1, and γ-secretase to subcellular compartments and the lipid composition and pH of these compartments are of central importance to determining the products of these biochemical cascades.

1.3 Role of cellular compartments in the Amyloid Cascade

APP, BACE1, ADAM10, and γ-secretase proteins mature from the endoplasmic reticulum (ER) to the Golgi apparatus and are transported to the plasma membrane (PM) via secretory vesicles along the constitutive secretory pathway.[71–73] ADAM10 is particularly enriched in the PM,[74] where 90% of APP cleavage occurs,[75] resulting in secretion of sAPPα and production of C83.[74] The majority of APP and BACE1 secreted to the PM are internalized within minutes via clathrin-mediated endocytosis[76–79] to early endosomes (EE).[80–82] A fraction of APP and BACE1 is recycled from EE back to the PM and another fraction remains in the EE which mature to late endosomes (LE). LE eventually traffic APP either back to the Golgi apparatus or to the lysosome for degradation.[83–85] γ-secretase complexes containing the PS1 domain primarily traffic to the PM, performing the majority of C99 production late in the secretory pathway.[86]

Unlike cytoplasmic and extracellular environments, endosomal compartments are acidic.[87] pH lowers from $\sim$6.5 to 4 pH as endosomes develop from EE to LE to lysozomes.[88] The acidic environments of these endosomes are crucial for BACE1 enzymatic activity, which has been shown to operate in a range from 4-6 pH.[89–91] The active pH range of γ-secretase is 6-8.4 pH, enabling the processing of C99 in endosomes and the PM,[92] though much γ-secretase activity is evidenced to occur in

the endoplasmic reticulum.[93,94] The majority of Aβ is evidenced to reside in the cytosol following production and prior to secretion.[95] In addition to controlling activity of BACE1 and γ-secretase, lower pH is evidenced to promote the formation of Aβ oligomers[96] via protonation of Glu22,[97] which stabilizes the characteristic β-turn defined by hydrogen bonding of Glu22-Lys28. This β-turn likely serves as the nucleus for Aβ aggregation.[15] Figure 1·2 summarizes the subcellular comparments in which processing occurs.

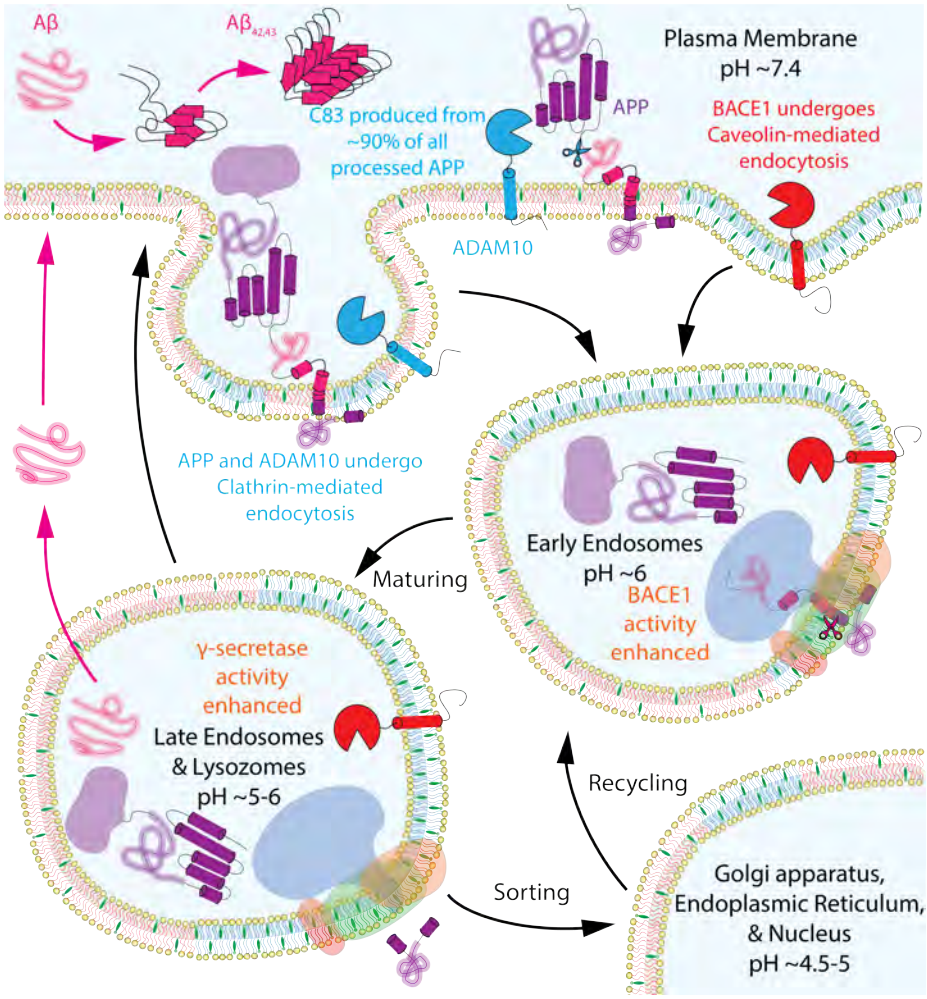

Figure 1·2: Illustration of subcellular compartments involved in the amyloid and complementary cascade pathways. APP, ADAM10, and BACE1 are represented in purple, blue, and red, respectively. Aβ is displayed in pink. The γ-secretase complex nicastrin, PEN-2, APH-1A, and presenilin 1 domains displayed in blue, pink, orange, and green, respectively. L_o domains represented with blue, ordered saturated lipid tails and a higher concentration of cholesterol, L_d domains represented with red, disordered unsaturated lipid tails and a lower concentration of cholesterol.

1.4 C99 Structure

Solution NMR measurements employing zwitterionic bicelles and micelles provide the primary source of information on the structure of C99 in a variety of membrane mimicking environments.[5,6,98] In these *in vitro* environments, there is evidence that residues 1-14 (see Figure 1·3) of the N-terminal domain (NTD) are disordered, residues 15-25 of the N-terminus have helical propensity (N-helix), residues 26-28 form a turn (N-turn), residues 29-52 form the helical transmembrane domain (TMD), residues 53-90 of the C-terminus form a disordered region (C-loop), and residues 91-99 of the C-terminus form a helix (C-helix).[5,6] Insertion of residues in the membrane evidenced by EPR[5] and NMR[6] measurements suggest that in some systems the C-helix and N-helix domains rest on the membrane surface, while the proximities of the NTD and C-loop domain to the membrane remain unclear.

The structure of the TMD is believed to be critical to the mechanism of recognition and cleavage of C99 by γ-secretase. The process of cleavage of C99 by γ-secretase begins with the "ε-cleavage" step, forming Aβ_{48} or Aβ_{49}, which are then further cleaved via "ζ-cleavage" to form Aβ_{45} and Aβ_{46}. These fragments are subsequently processed by "γ-cleavage" to predominantly form Aβ_{38}or Aβ_{42}, and Aβ_{40} or Aβ_{43}, respectively.[99] C99 features a glycine zipper motif, $G_{29}xxxG_{33}xxxG_{37}$, in the TMD, which is frequently observed in dimer-prone single-pass TM proteins.[100,101] It is further evidenced to be a component of putative cholesterol binding site on C99,[53,102] a finding that is important because cholesterol has been hypothesized to recruit C99 to γ-secretase.[53,103,104] Mutation of G29 and G33 in this motif reduces Aβ_{42} production,[105] and is expected to reduce C99 homodimerization.[106] Proximate to the N-terminal portion of the GxxxG repeat motif lies a "GG hinge" at $G_{37}G_{38}$ in the TMD, previously identified by molecular dynamics simulations[107,107] and conjectured to be important to processing by γ-secretase.[108] Hydrogen-deuterium (H-D) exchange studies observed side chain[108] and α-helix[109] hydrogen bonds to be substantially weaker near the GG hinge, suggesting the amide bonds are readily available for γ-cleavage. Thickening of the membrane reduces the relative amount of Aβ_{42} and Aβ_{43} produced while leading to an overall increase in γ-secretase activity.[110,111] Increasing the curvature of membrane is found to increase the magnitude of fluctuation of the GG hinge and the overall tilt of the TMD.[112] It is likely that magnitude of fluctuations in the hinge may enhance Aβ_{42} and Aβ_{43} production.[5] Additionally, simulation studies

have revealed[107,113,114] that the GG hinge is an important structural feature for C99 dimers, with the angle of the hinge varying for several distinct dimerization motifs. It has further been noted that the membrane thickness can preferentially stabilize and environmentally select specific C99 dimer conformations.[105,113–115] Beyond the hinge lies $G_{38}xxxA_{42}$, another glycine zipper motif often found in TM dimers,[106] important for C99 homodimerization.[116] The GxxxG repeat motif appears to facilitate C99 dimer formation in thicker membranes while the competing GxxxA motif supports dimers most often observed in thinner membrane and micelle.[98] At the C-terminal end of the TMD, residues A42, T43, V44, I45, V46, T48, L52, and K53 all feature several mutations found in AD.[117] Some mutations decrease the propensity for homodimerization,[118] and enhance Aβ_{42} production.[119] A "lysine anchor" formed by the triple repeat $K_{53}K_{54}K_{55}$ is evidenced to register at the C-terminal end of the TMD membrane surface.[120]

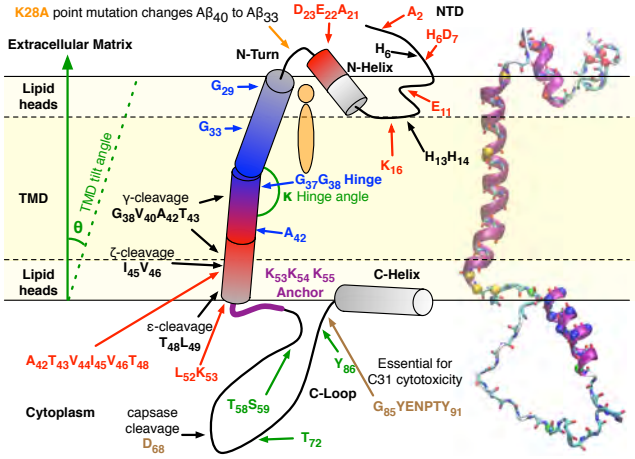

Figure 1·3: Yellow represents hydrophobic core of the membrane. Red residues contain FAD mutations. Blue residues are critical to formation of C99 dimers. Green residues may be phosphorylated. Purple residues form the lysine anchor. Black indicates γ-secretase cleavage sites and metal binding residues. Brown residues are critical for C31 formation and cytotoxicity. Cylinders represent domains with significant helical propensity. θ and κ angles describe the TMD tilt and GG hinge angle. θ angle increases with thinning or curving of the membrane surface, and κs increases with curving of the membrane surface. Black solid lines mark membrane surface and black dashed lines represent membrane hydrophobic core. Orange lipid marks the putative cholesterol binding site. Also shown is an atomistic structure of C99 predicted from TALOS+ using LMPG micelle backbone chemical shifts and secondary structure assigned with STRIDE. Cα within the atomistic structure are labeled as N-terminal familial AD mutation (red), residues 28, 37, 38, 53, 54, and 55 (orange), phosphorylatable residues Cα (green), and C-helix (blue).

While the C99 transmembrane domain (TMD) structure has been the focus of experimental and computational studies, the structure of the extra-membrane residues has received relatively little attention in spite of the evidence that changes to the extra-membrane domains of C99 are crucial to determining the production of Aβ and onset of AD. The N-terminus of C99 almost certainly interacts with the nicastrin domain of γ-secretase.[121] Within the N-loop (or N-turn) domain, $S_{26}N_{27}K_{28}$ Ala point mutation of K28 has a dramatic impact on APP processing, switching formation of Aβ_{40} to Aβ_{33}, implicating this turn in the γ-secretase interaction.[120] The juxta-membrane (JM) domain, K_{16}LVFFAED$_{23}$ plays a role in inhibiting γ-secretase binding[122] and interacting with cholesterol.[5,53,102,123] The mutation K16N is known to make APP untenable for binding by α-secretase[124,125] Furthermore, membrane insertion of residues in the JM domain appears to sensitively depend on pH.[102,123] The JM domain also features mutants A21G,[126] E22Q,[127] E22K,[128] E22G,[129] E22Δ,[130] and D23N,[131] all found to occur in AD patients. Within residues 1-15 the disordered N-terminal domain (NTD) features the E11K mutation, which was found to enhance Aβ production.[132] The mutations D7H,[133] D7N,[134] H6R,[134] and A2V[135] were found in patients with early onset of AD, suggesting a role for these residues in interaction with γ-secretase. Additionally, histidine residues in the N-terminus H6, H13, and H14 are known to bind with Cu and Zn metals, found in high concentration in amyloid plaques.[136] Additionally, Aβ_{42} forms a complex with the C99 N-terminus when C99 is membrane-bound, which enhances C99 homo-oligomer formation.[137]

In the C-loop there are several phosphorylatable residues, identified at T58, S59, T72,[133] and Y86.[138] The phosphorylation of S59 enhances trafficking of APP to the golgi apparatus.[139] It has been noted that Ala point mutation at T72 may enhance the production of Aβ_{40} and Aβ_{42},[140–142] impacting interaction of APP with some enzymes.[143] Y86 has been identified to be phosphorylated at higher concentrations in the brains of AD patients, and is suspected to prevent the interaction of APP with adaptor proteins.[141]

The C-loop and C-helix are known to interact with several proteins in the cytoplasm, forming complexes in which these domains adopt an α-helical structure.[144] The C99 sequence binds to many cytoplasmic proteins including the G protein G0 with residues H61-K80,[145] the adaptor protein Fe65 with residues D68-N99,[146] the adaptor protein X11 with residues Q83-Q96,[147] the adaptor protein mDab1 with a similar residues to X11,[148] and the kinase Jip-1 with residues N84-F93.[149] The C-terminus is cleaved

by caspases at D68 to form C31, a cytoplasmic protein found in AD patients and evidenced to signal apoptosis.[150] Aβ-C99 complex-enhanced C99 oligomerization increases the production of C31.[137] Mutation of D68 to Ala prevents production of C31, abrogating cytotoxic function.[151] Additionally, residues 85-91 (GYENPTY) are found to be essential for cytotoxic activity of C31, and are involved in interactions with many cytoplasmic proteins.[137] Because the C99 N-terminus contain many mutations that play a role in the etiology of AD, the N-terminus contains the Aβ domain, and the C-terminal domains bind to so many cytoplasmic proteins, the C99 extramembrane certainly form a variety of stable secondary and tertiary structures. The conformational ensemble of the C99 monomer and homodimer likely contain signatures of such secondary and tertiary structures despite appearing to be random coil in NMR chemical shifts.

1.5 Lipid Rafts and Endocytosis

Localization of proteins to the membranes of the same subcellular compartment is necessary but not sufficient for the dimerization of two proteins to facilitate proteolysis. Within the same membrane there can be a separation of lipids and proteins to dense domains which further compartmentalize the spaces in which protein-protein associations are likely to occur. These dense domains in membranes, often called "lipid rafts", are thought of as unique platforms for facilitating protein function by providing a confined location to enhance specific protein-protein interactions.[152] Lipid rafts have been observed *in vitro*[153] and *in vivo*.[154,155] Raft domains are primarily characterized by a lateral condensation of saturated lipid acyl chains upon association with cholesterol, defining the liquid ordered (L_o) lipid phase, unique from the liquid disordered (L_d) lipid phase which characterizes the membrane bulk. The L_d and L_o phases are both stable at physiological conditions, and are two of many lipid bilayer phases.[156]

There is general consensus in the literature that γ-secretase and BACE1 partition to lipid raft domains, and that APP and ADAM10 partition to the non-raft membrane bulk[157–162] However, the partitioning of these proteins can strongly depend on palmitoylation, which has been quantitatively determined to enhance protein partitioning to lipid rafts.[163] Palmitoylation of APP Cys186 and Cys187, for example, is evidenced to partition APP to lipid raft domains while also enhancing APP homodimerization

via E1 domains and may be a primary means by which APP comes to associate with BACE1.[164,165]

Clathrin-mediated and caveolin-mediated are the two primary mechanisms of endocytosis from the plasma membrane which are known to affect the processing of APP. Clathrin-mediated endocytosis principally involves the formation of triskelia of Clathrin protein that form a lattice, causing the membrane to bud and eventually pinch off part of the PM, forming a vesicle, and releasing this vesicle which develops into an early endosome.[166,167] Caveolin-mediated endocytosis principally involves the coating of lipid raft domains by cavins and caveolins, which facilitate budding and eventual development to early endosomes.[168] ADAM10 and APP are both evidenced to bind to the AP2 adaptor protein and other adaptins, which binds proteins for clathrin-mediated endocytosis.[48,72,84,169,170] BACE1 is evidenced to undergo caveolin-mediated endocytosis via binding to flotillin-1 protein in caveolae.[171]

As such, it seems that APP overwhelmingly co-localizes with ADAM10 in the PM bulk, resulting in the production of C83 in the PM or in EE formed via clathrin-mediated endocytosis. The remaining population of APP may co-localize with BACE1 in lipid rafts of the PM, in EE or LE formed by caveolin-mediated endocytosis. It may be that the majority of APP which are processed by BACE1 are palmitoylated, facilitating the partitioning of APP to lipid raft domains and thus co-localization of APP and BACE1 in endosomes resulting from caveolin-mediated endocytosis. The structural and composition differences between the L_o phase of lipid rafts and the L_d phase of the lipid bulk also likely play a role in modulating protein structure and function.

1.6 The Liquid Ordered Phase

In general, it has been observed that the liquid ordered (L_o) phase manifests as a continuous phase transition in binary and higher-order lipid mixtures of saturated lipids with cholesterol as cholesterol concentration increases. This occurs by the local condensation of saturated lipid tails with sterol molecules, which increase alignment of carbon-carbon bonds along the lipid acyl chains with the normal of the membrane plane. Cholesterol is the most common sterol in mammilian cellular membranes and is employed as the sole sterol in model lipid bilayer experiments. The alignment of acyl chains also results in a longitudinal thickening of the membrane. These features can

be detected by various experimental methods, most classically via NMR spectroscopy to characterize the average carbon-carbon bond angle and scattering techniques to characterize lipid packing, as well as through more modern approaches employing vibrational spectroscopy, atomic-force microscopy, and interferometry. Vist and Davis presented the first phase diagram characterizing the L_d to L_o phase transition of binary mixtures of di-C 16:0 PC (1,2-di-palmitoyl-sn-glycero-3-phosphocholine, DPPC) and cholesterol at various temperatures using NMR.[172] It was observed that the L_o phase is gradually introduced to the system, coexisting with the L_d phase, as Chol concentration increased up to approximately 20 mol%. Similar observa-tions of this continuous phase transition as Chol concentration increases to 20 mol%have been made for other mixtures with saturated lipids.[173–177] MD simulations have been particularly useful for exploring the atomistic details of lipid mixtures and have demonstrated that on the microscopic level the L_o phase features subdomains of hexagonally-packed lipid tails separated by interstitial cholesterol and lipids, which are validated via comparison with experimental order parameters.[178,179]

The L_o phase is also distinct from the lipid gel (S_o) phase, which is thicker than the L_o phase due to longitudinally aligned carbon-carbon bonds along the lipid tail which are laterally hexagonally-packed. The S_o phase is particularly distinct from the L_o phase because it manifests from a first order phase transition from the L_d phase at a critical melting temperature (T_m), though this temperature is substantially lowered in lipid mixtures and more complex bilayers such that it is completely inaccessible in physiological conditions. In mixtures of Chol and saturated lipid, increasing Chol concentration is evidenced to lower T_m so much that the first order phase transition that would signify the transition from the L_o to S_o phase is completely abolished, suggesting that the L_o-S_o phase transition does not exist.[173–177] Rather, it seems that the small hexagonally-packed domains of lipid tails within L_o phases are adopting conformations very similar to those observed in the S_o phase, and that the L_o phase is something of a mixture of small S_o phase-like lipid domains separated by interstitial Chol and L_d phase-like lipids (Figure 1·4). Order parameters useful for describing these phases are discussed and introduced in Chapter 2.

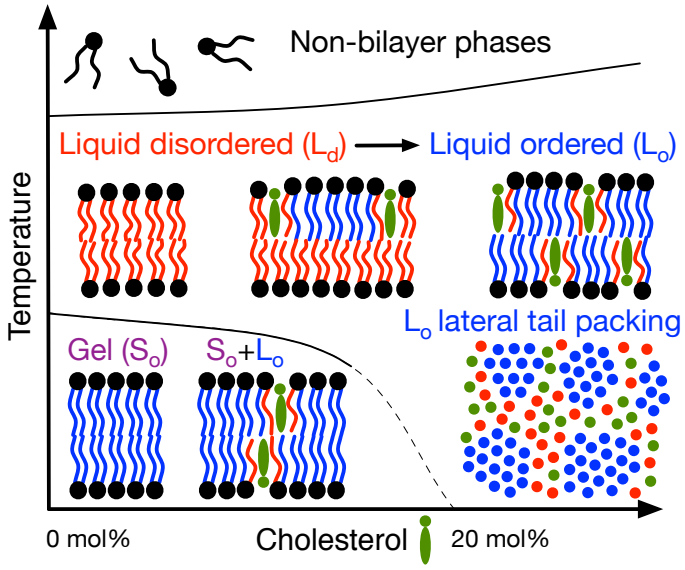

Figure 1·4: Relative phase diagram of temperature, saturated lipid (black head group) concentration, and cholesterol (green) concentration at sufficient concentrations of aqueous solvent to facilitate lipid bilayer formation. Solid lines define demarcate relative first order phase transition temperatures. L_d phase lipid tails (red) are shorter and more disordered, S_o phase lipids (blue) are elongated and hexagonally-packed laterally. The L_o is characterized as combination of domains of elongated and laterally hexagonally-packed lipids similar to S_o phase lipids separated with interstitial cholesterol and L_d phase lipids.

1.7 Lipid Phase Separation

Lipid phase separations form in mixtures of saturated lipids, unsaturated lipids, and cholesterol when saturated lipid and cholesterol concentrations are high enough to form the L_o phase. Phase diagrams of ternary mixtures of one species of saturated lipid, one species of unsaturated lipid, and a sterol as a function of temperature are determinable via various experimental techniques including using fluorescence spectroscopy,[180–197] X-ray scattering,[3,180,198–202] atomic force microscopy (AFM),[181,202–204] NMR,[189,196,197,205,206] interferometric scattering,[207] and Raman spectroscopy,[2,208] Generally, at physiological temperatures ternary mixtures are observed to phase separate around equimolar, 1:1:1 molar concentrations of saturated lipid, unsaturated lipid, and cholesterol, defining a miscibility gap region inside the phase diagram in which systems are observed to form large, macroscopically-observed phase separations in the system (Figure 1·5). At low ($\lesssim$45 mol%) and high ($\gtrsim$45 mol%)

Chol concentrations macroscopic phase separations disappear. Above about 66 mol% cholesterol, cholesterol crystallizes and crashes out of the solution, such that typical membranes can only accommodate up to 66 mol% cholesterol,[209–212] above which Chol forms crystals in solution,[175,213] though there are cellular membranes that can exceed this, such as the ocular cell membrane.[214]

Formation of domains of lipids in bilayers has been called "lipid phase separation," "lipid domain formation," or "lipid raft formation," each of which has distinct meaning.[215] In general, these terms are used to describe the binary liquid-liquid phase separation that features coexistence of L_d and L_o phases in the membrane. Over the past 15 years, many investigations have focused on ternary mixtures of Chol with one high and one low melting temperature (Tm) lipid species.[216] Multiple points on phase diagrams of macroscopically-observable lipid bilayer phase separations resulting from mixtures of saturated lipids, unsaturated lipids, and cholesterol have been observed using fluorescence spectroscopy,[180–197] X-ray scattering,[3,180,198–202] atomic force microscopy (AFM),[181,202–204] NMR,[189,196,197,205,206] interferometric scattering,[207] and Raman spectroscopy,[2,208] allowing us to achieve a general concept of ternary lipid mixture phase diagrams.

In Figure 1·5 we briefly summarize the current picture of ternary phase diagrams. At relatively lower T (or higher Tm) So is evidenced to exist as a macroscopic phase separated state via fluorescence experiments, AFM, and NMR. So can disappear at physiological temperatures due to presence of Chol[173–177] or unsaturated lipids,[217–220] which lower the Tm of saturated lipids. At high ($\gtrsim$40 mol%) Chol concentrations macroscopic phase separations disappear. Critical fluctuations in domain mixing manifest at one or two points in ternary phase diagrams, depending on whether the immiscible region is open or closed due to lack or presence of the So phase.[185,197,221–224] Modern fluorescence,[183,225] X-ray,[4,199] and AFM experiments[203,204] have shown that nanoscopic ordered and disordered domains coexist outside of the miscibiliy gap around 1:1:1 ratio mixtures, as Chol appears to never truly induce the Lo phase in un-saturated lipids. X-ray scattering experiments have revealed that 60 nm diameter domains of pure Chol domains can coexist with domains of saturated and unsaturated lipids at these high mol% Chol compositions.[175,202,226,227] Beyond the 66 mol% solubility limit of Chol in bilayers,[209–212] Chol forms anhydrous crystals in solution.[175,213] Additionally, though the main phase transition (S_o to L_d) is first order, phase transitions from L_d to L_o and L_o to Chol domains seem to be continuous.

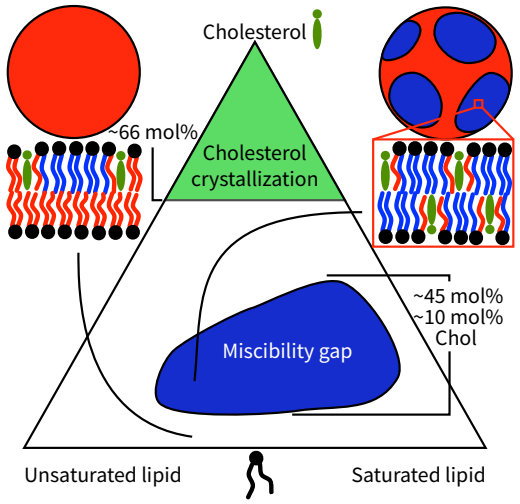

Figure 1·5: Cartoon phase diagram representative of many mixtures involving saturated lipids, unsaturated lipids, and cholesterol at fixed temperature and concentration in aqueous solution in the lipid bilayer phase displaying the miscibility gap region where phase separation is observed. Illustrations of the longitudinal conformation of lipids in L_o domains in phase separated and miscible systems demonstrate why nanoscopic domains are miscible and difficult to detect at lipid concentrations that do not phase separate. Above 66 mol% concentration relative to lipids, cholesterol crystallizes.

Just outside of the miscibility gap, modern fluorescence,[183,225] X-ray,[4,199] and AFM experiments[203,204] have identified a coexistence of nanoscopic lipid domains, rather than a homogeneous lipid phase. Such nanoscopic domains disappear as the concentration of DPPC and Chol in systems becomes near-zero. At high cholesterol concentrations the observation of pure cholesterol domains has also been evidenced via interpretations of X-ray spectra, suggesting that domains of pure cholesterol crystals can be embedded and freely float in the membrane.[175,202,226,227] Another curious type of domain that may exist are maze-like arrangements of cholesterol interlaced with lipid tails[177,210] that may form at very high cholesterol concentrations due to the affinity of the cholesterol homodimer[228,229] and the unfavorability of cholesterol-lipid hydrogen bonding.[230]

The kinetic mechanism of lipid phase separation is generally classified into a few processes.[231] In a lipid mixture, the minority phase (either L_o or L_d phase, depending on system composition) first nucleates as lipid nanodomains. These nanodomains merge into microdomains in their local environment, then these microdomains merge with other microdomains either via Ostwald ripening, in which microdomains of widely

varying sizes gradually merge into one macrodomain, or via coalescence, in which microdomains of approximately equal sizes rapidly merge into one macrodomain. Coalescence occurs when the two phases will be of approximately equal overall surface area in the membrane. Ripening occurs when there is a phase that will take up a significantly smaller surface area than the opposite phase. These differentiable macroscale processes of ripening or coalescence have been characterized in many systems via fluorescence and atomic force microscopy.[232–234] Nanodomains of the L_o phase in systems outside of the miscibility gap are kinetically stable, though the system composition is insufficiently high in saturated lipid and cholesterol to facilitate formation of microdomains.

The strong preference of Chol to partition to L_o phase domains over L_d phase domains is another curious observation, and has led to speculations about the role of lipid rafts as platforms for facilitating specific protein-cholesterol interactions.[235] It is evidenced that there is a Chol L_o:L_d phase partitioning of approximately 4:1 and 2:1 in 20 and 40 mol% Chol based on experiments in phase separating DPPC:DOPC 1:1 mixtures including Chol. Supported monolayer Raman microscsopy experiments performed by Donaldson and Aguiar determined L_o:L_d partitioning of Chol in 20, 33, and 50 mol% Chol at 3.9:1, 1.5:1, and 2.2:1, respectively.[2] Similarly, Ma et al. determined Chol L_o:L_d partitioning to be 39.9, 3.63, 2.60, 2.17, and 2.13 at 10, 16, 20, 25, and 30 mol% Chol.[236] The variable partitioning of cholesterol between L_o and L_d phases as a function of Chol concentration manifests due to the apparently high affinity of Chol for small domains of saturated lipids, and may allow for formation of small L_o domains even with very minor concentrations of Chol and saturated lipid.

The preferences of protein partitioning to L_o or L_d domains is of general interest in understanding how lipid rafts may facilitate protein function, as well as how post-translational modifications can affect protein affinity for lipid domains. Generally, lipidation modifications, particularly palmitoylation, are evidenced to increase the affinity of proteins for lipid raft domains. Partitioning coefficients describing protein preference for association with L_o or L_d domains have been measured using fluorescence microscopy experiments.[155,163]T here is much room for exploration into where and how proteins localization to regions of phase separated systems, how proteins behave during the phase separation process, and how phase separation controls enzyme kinetics.

1.8 Suggestions for Cholesterol Effect on C99 and Aβ

The onset of Alzheimer's disease (AD) has long been correlated to enhanced levels of cholesterol resulting from diet, genetic predisposition, or aging.[237–244] Enhancements to cellular cholesterol concentration are also evidenced to upregulate Aβ synthesis.[239,245] Cholesterol has been proposed to modulate C99 conformation through a C99-cholesterol complex. The C99-cholesterol complex was first suggested by Sanders and co-workers based on observations of shifts in the 1H-15N 2D NMR spectra of C99 as a function of the concentration of cholesterol analogue β-CholBIMALT in LMPG micelles.[98,104] Subsequent experiments by Barrett et al.[5] in DMPC:DHPC bicelles led to the proposal that C99 binds to cholesterol via the glycine- rich face of the N-terminal region of the transmembrane domain (TMD). The same glycine rich face plays a role in stabilizing C99 homodimers.[100,107,114] It was further proposed that the binding site is completed by formation of the C99 juxtamembrane helix. Further studies by Song et al. characterized the equilibrium constant of C99-Chol association, as -2.1 kcal/mol via fitting changes in chemical shift as a function of protein and cholesterol concentration to a phenomenological kinetic model.[53] The observed association is weaker than typical protein backbone-water hydrogen bonds.[246]
Cholesterol is also evidenced to enhance the interaction of Aβ with the surface. Via AFM Gao et al. and Kandel et al. demonstrated that Aβ pores can be activated within Chol concentrations in which phase separation are observed in a ternary mixture, and deactivate when the Chol concentration increases to the point where phase separation disappears.[247,248] Fantini et al. demonstrated that cholesterol:GM1 binary mixtures and cholesterol:GM1:POPC ternary mixtures, which are in the L_o phase and phase separate, respectively, stabilize GM1 conformations which form strong hydrogen bond interactions with Aβ, facilitating aggregation of the membrane surface.[249] Rather than specific interaction with cholesterol, it may be that cholesterol plays its role in controlling the amyloid cascade almost exclusively through the L_o phase alone. It may be that the L_o phase is principally responsible for modification to the behavior and conformation of APP, C99, and Aβ that are so frequently attributed to specific interactions with Chol. Such investigative work requires experiments or molecular simulation approaches that can reliably capture atomistic details of cholesterol and protein in lipid bilayers.

1.9 Investigations Presented in this Thesis

In this thesis, I explore several basic questions regarding lipid phase separation, C99 structure, and the role of cholesterol in both phase separations and modulating C99 structure using molecular dynamics simulation. In Chapter 2 analysis and simulation methods developed and deployed for these studies are described. In Chapter 3, finite-size effects on phase separation in quasi-two-dimensional periodic systems are analyzed to understand system sizes required to simulate the phenomenon. In Chapter 4, the effects of varying cholesterol concentrations on lipid phase separations are investigated, revealing complex phase behavior. In Chapter 5, the effect of both introducing the L_o phase via addition of cholesterol and effect of pH and FAD mutants on the conformational ensemble of $C99_{16-55}$ are investigated, finding C99-Chol interaction to be much less specific than previously believed. In Chapter 6, simulations modifying the thickness of implicit solvent lipid bilayers on the conformational ensemble of full-length C99 are presented, and suggest roles for β-strands in complex protein-protein interactions involving C99. In Chapter 7, large-scale simulations of the full-length C99 monomer and homodimer in all-atom explicit solvent are presented and are used characterize the nature of their conformational ensembles. In Chapter 8, a perspective on future simulation work to understand the role of phase separations on C99 is presented along with a sample of preliminary work demonstrating partitioning of C99 to the interface between L_o and L_d domains. These simulation results are analyzed and discussed in context of a variety of experimentally-measured data and interpretations on a case-by-case basis.

Chapter 2

Methodology

Characterization of phase separations, C99 conformational ensembles, and roles of cholesterol in effecting both of these, requires the use of a variety of analysis methods. Several of the analysis methods employed are either innovations on conventional approaches or completely novel approaches to analyze lipid and protein structure. In this chapter, order parameters used throughout this thesis are defined with helpful illustrations and specific atom names used in most analyses.

2.1 Lipid Order Parameter Analysis

2.1.1 Assignment of cholesterol to leaflets

Cholesterol translocates between lipid leaflets, performing a flip such that the alcohol group is oriented towards aqueous solution which is evidenced to most likely occur at the midplane between lipid leaflets. The complete process of cholesterol translocation between leaflets is often simply referred to as a "flip-flop". Cholesterol flip-flop rates have been estimated to occur between nanosecond and seconds pending system conditions, method, and interpretation of measurement.[250] In the MARTINI coarse grained model and CHARMM36 or Slipids all-atom MD simulations, cholesterol flip-flop is observed to occur at rates of $10^{5-8}\ s^{-1}$ and $10^{1-6}\ s^{-1}$, respectively.[251–254] Due to flip-flop between leaflets, which is often observed in coarse-grained simulations and multiple microsecond-long all-atom simulations, Chol molecules need to be assigned to lipid leaflets within each frame for proper analysis. In such simulations, we assessed whether the head group of cholesterol was closest to an upper or lower leaflet lipid head group (the phosphorous atom for phosphatidylcholine lipids) within up to 1.5 nm in distance, and assigned cholesterols to the leaflet of that closest lipid for analysis.

2.1.2 Lateral lipid mixing entropy and miscibility point

To quantify how laterally mixed each leaflet of a lipid bilayer is, an entropy of mixing is occasionally employed in the study of lipid mixtures.[255,256] We define the lipid mixing entropy by employing Voronoi tessellations of the xy-plane positions of representative atoms from lipid or cholesterol heads or tails and, in the case of proteins, from the 4-residue alpha helical turn of a protein TMD closest in height to the surrounding representative atoms from lipids and cholesterol. In particular, we assess the mixing entropy to measure the degree of phase separation in the lipid bilayer by evaluating the observed likelihood of contacts formed between lipids of the same type, p_1 (*e.g.* DPPC-DPPC), and between lipids of different type (*e.g.* DPPC-DUPC) as

$$S_{\text{mix}} = -p_1 \log_2 p_1 - p_2 \log_2 p_2. \tag{2.1}$$

Within this mixing entropy, it is useful to determine the critical value at which a lipid bilayer is phase separated. In fluorescence microscopy experiments on vesicles including fluorescent probes that spatially label the L_o or L_d phase, the point of miscibility is defined as the point at which fluorescence is 50% of the maximum fluorescence observed in phase separated domains. A similar point of 50% miscibility can be derived for application to our mixing entropy with Voronoi tessellations. Because each lipid tail has six nearest neighbors on average, we can build a lattice model on which we represent each lipid leaflet with a finite number of sites.[228,257] At approximately equal concentrations of saturated and unsaturated lipids, the phase separation will manifest as a stripe under periodic boundary conditions, as will be demonstrated in Chapter 3. Stripe shape phase separated periodic systems in which x- and y-dimensions are of equal length, L, and N sites, will be characterized by two interfaces of length $L = d\sqrt{N}$, where d is the lattice spacing. The domains of each system are totally pure, only containing one type of lattice site. Each of the interfaces features $1/3$ interactions with lipids of the opposite phase and $2/3$ interactions with lipids of the same phase. Thus mixing entropy of a perfectly phase separated stripe of such a system can be defined in terms of $p_1 = (N - 2\sqrt{N} + 2\frac{2}{3}\sqrt{N})/N$ and $p_2 = (2\frac{1}{3}\sqrt{N})/N$ as illustrated in Figure 2·1.A.

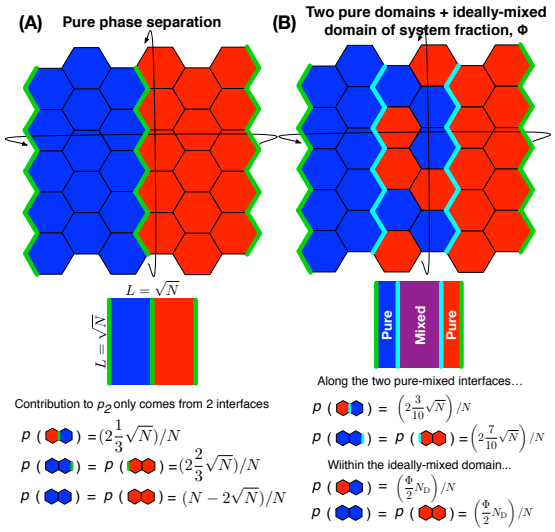

Figure 2·1: (A) Illustration of a pure binary phase separation on a periodic hexagonal lattice. The two types of lipids are represented in red and blue, respectively, and the interfaces between domains are drawn with a bold green line. (B) Illustration of pure domains in a binary mixture coexisting with an ideally-mixed domain composing (Φ) percent of the system. The two types of lipids are represented in red and blue, respectively, the interfaces between pure domains are drawn with a bold green line, and the interfaces between ideally-mixed and pure domains are drawn with a bold cyan line.

We can add an ideally-mixed phase of some fraction, Φ, to the system which contains both L_o and L_d phase type lipids. Two interfaces of the system will define the boundary of L_o phase and L_d phase to the mixed phase, and one interface will define the boundary between the L_o and L_d phases. The two new interfaces would feature 3/10 (7/10) contacts between lipids of opposite (same) phase type. The number of lipids not present in domains (not at these three interfaces) is $N_D = N - 3\sqrt{N}$. The number of lipids present within the mixed domain, $N_D\Phi$, contribute equally to p_1 and p_2. The mixing entropy of a system which experiences a stripe-shaped phase separation as % miscibility Φ is thus defined by $p_1 = \left((N_D - N_D\Phi) + \frac{1}{2}N_D\Phi + \frac{2}{3}\sqrt{N} + 2\frac{7}{10}\sqrt{N}\right)/N$ and $p_2 = \left(\frac{1}{2}N_D\Phi + \frac{1}{3}\sqrt{N} + 2\frac{3}{10}\sqrt{N}\right)/N$, as illustrated in 2·1.B.
In these equations, S_{mix} depends on both Φ and N, for which most solutions will converge to the thermodynamic limit by approximately 10,000 lipids per leaflet, which happens to also be the thermodynamic limit of phase separation in MARTINI model simulations of phase separation described in Chapter 3.

2.1.3 Area per lipid tail

One of the key features of the L_o phase is the nonadditive condensation of the xy-plane as cholesterol is added to the lipid bilayer.[257,258] Conventionally, the area per lipid is determined by dividing the area of the xy-plane by the number of lipids in each leaflet. However, this is not sufficient for differentiating the area for each molecular species in mixtures or for systems containing multiple phases. The area per lipid tail and cholesterol can be calculated in regard to specific molecular species using the areas of Voronoi tessellations of atoms of these molecules that best represent the most well-packed layer of the lipid bilayer.

2.1.4 Lipid lateral packing and orientational order

The phases of 2D systems are often characterized by use of the Nelson-Halperin 2D bond-orientational order parameter,[259] famously used to study the solid, hexatic, and liquid phases of hard disk systems.[260] Within a 2D system of N particles, the n-fold orientational order of each particle, Ψ_n^k (indexed by k) is evaluated using the angles of n nearest-neighbor particles (each indexed by l) measured using a constant reference vector, as

$$\Psi_n^k = \frac{1}{n} \sum_{l \ \epsilon \ nn(k)}^{n} \exp[in\theta_{lk}] = \frac{1}{n} \sum_{l \ \epsilon \ nn(k)}^{n} \cos(n\theta_{lk}) + i \sin(n\theta_{lk}). \tag{2.2}$$

Typically, the 6-fold order parameter

$$\Psi_6^k = \frac{1}{6} \sum_{l \ \epsilon \ nn(k)}^{6} \exp[i6\theta_{lk}] \tag{2.3}$$

is of greatest interest, as most 2D systems sit on a hexagonal lattice in the solid state. Ψ_6^k was computed based on the position of lipid and cholesterol tail atoms or center of protein 4-residue helical turn that represent the most well-packed z-axial layer in the lipid bilayer. The six nearest neighbors (l) of each point (k) were found using the Cartesian coordinates of the k and l points fitted to a plane using their singular value decomposition prior to the measurement of Ψ_6. The reference vector, $\vec{r}$, was positioned at k, pointed along the x-axis, and was fitted to the same plane as the k and l points. It is necessary to use this for quasi-2D systems like a lipid bilayer for which the local plane of best fit can be different from the xy-plane due to the shape

of the curvature of the membrane surface.

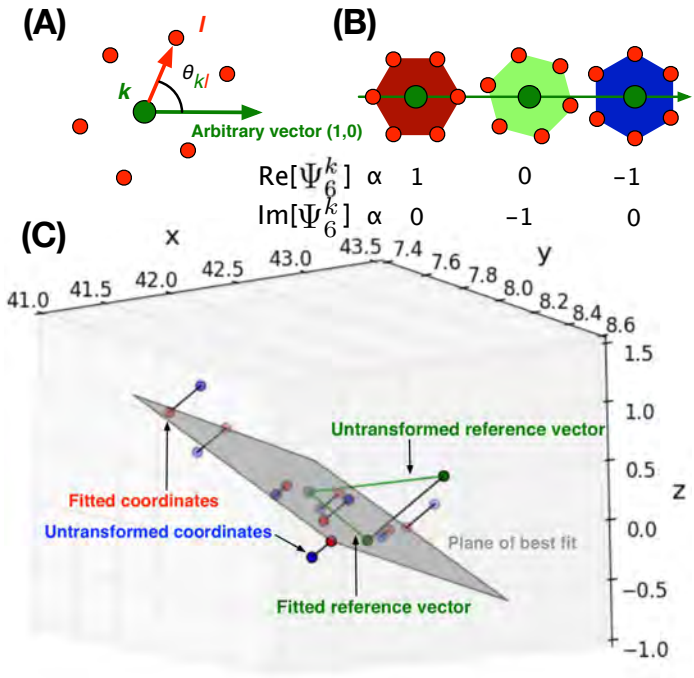

Figure 2·2: (A) Illustration of a particle k and its six nearest neighbors, indexed by l, along with the reference vector, which is often selected to be (x,y) = (1,0). (B) The orientation of the l six nearest neighbors around k are described over a range of 60 degrees by the complex value of Ψ_6^k. If $|\Psi_6^k| = 1$ the six nearest neighbors have precisely 60 degrees of separation from each other in θ_{kl}, like the corners of a hexagon. (C) Representative plane-fitting of C2A and C2B DPPC lipid and R3 cholesterol tail atoms around a DPPC C2A tail atom from a MARTINI simulation, used to measure Ψ_6^k.

The complex value of Ψ_6^k describes the orientation of the nearest neighbors around particle k relative to the reference vector. The absolute value of Ψ_6^k describes how similar the orientation of the six nearest neighbors of particle k is to a hexagon, *e.g.* $\theta_{lk} \in \{0, 60, 120, 180, 240, 300\}$, which form a perfect hexagon whose orientation is characterized by $\Psi_6 = 1 + i0$ and which is perfectly symmetric, characterized by $|\Psi_6^k| = 1$ Figures 2·2.A and 2·2.B illustrate how Ψ_6^k is measured and Figure 2·2.C provides a demonstration of projecting points to a plane of best-fit. In a 2D crystal, all particles will have $|\Psi_6^k| = 1$ and the same complex value of Ψ_6^k. In a solid phase, all particles have nearly $|\Psi_6^k| = 1$ and the pair correlation function of Ψ_6^k will decay over a long distance. In a hexatic phase, all particles have an intermediate value of

$|\Psi_6^k|$ and the pair correlation function of Ψ_6^k will decay over a moderate distance. In a fluid phase $|\Psi_6^k|$ will not have a high value and the pair correlation function of Ψ_6^k will decay over a short distance. The MC simulation work of Bernard and Krauth provides a good demonstration of the use of Ψ_6^k in describing 2D hard disk phases.[260]

2.1.5 Lipid longitudinal order

Lipids are an example of an anisotopic (long and thin) molecule which can form a liquid crystal upon reaching a sufficient concentration in solution. For this reason sometimes the most ordered lamellar bilayer phase of lipids is called the liquid crystalline phase. There are many non-lamellar phases of lipids which are stable at concentrations and temperatures not explored in this thesis, such as miscible, micellar, hexatic, and cubic phases of lipids depending on lipid concentration and temperature.[261] The most famous example of a concentration-dependent phase transition is the Onsager model for the isotropic-nematic phase transition, in which it is demonstrated that a lamellar (nematic) phase becomes more thermodynamically stable than an isotropic phase as the concentration of the molecular species increases due the increase in translational entropy afforded by packing molecules into a lamellar phase.[262] Dramatic phase transitions such as the isotropic-nematic phase transition are described by the angle θ between the long axis $\vec{u}$ of molecules to and a reference vector $\vec{n}$, typically the z-axis of the system along which the nematic phase is oriented. The average second order Legendre polynomial of $\cos\theta$,

$$P_2(\cos\theta) = \frac{1}{2} < 3\cos\theta^2 - 1 >, \tag{2.4}$$

often simply referred to as P_2, is used as the order parameter to describe the isotropic-nematic and other liquid crystal phase transitions. For lipids, we often measure P_2 by using the vector defined by the carbonyl carbon of each lipid head and the terminal carbon of each lipid tail, and using either the z-axis or the normal vector for the plane of best fit to the six nearest lipid neighbors as the reference vector. A similar measure of lipid longitudinal order is the carbon-hydrogen S_{CH} order parameter, for which P_2 is measured for each type of carbon-hydrogen bond on lipid tails.[263] S_{CH} is measured experimentally from quadripolar splitting in deuterium[264] and dipolar splitting carbon-13 labeling NMR experiments.[265] Example vectors defining P_2 and S_{CH} are illustrated in Figure 2·3.

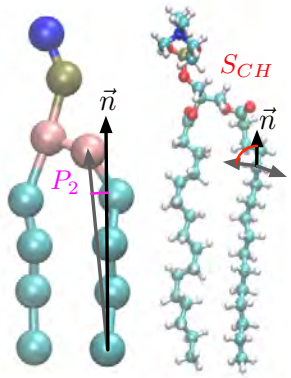

Figure 2·3: Illustration of example vectors defining P_2 in MARTINI DPPC with GL2-C4B beads and S_{CH} in CHARMM36 DPPC with C35-[H5X/H5Y].

2.1.6 Lipid domain clustering and formation mechanism

There are many interesting questions that might be asked about the size of intra-leaflet lipid domains, inter-leaflet contacts interactions with lipid domains, and the effect of lipid domain size on lipid structure. We assign intra-leaflet clusters of lipids and cholesterol using the hierarchical single-link clustering algorithm,[266] employing representative atoms of lipid tails and cholesterol. Both in atomistic and coarse-grained models, we use an intra-leaflet distance cutoff of 5.8 Å to assign DPPC and cholesterol to a cluster. Clusters of DPPC and cholesterol will develop into L_o domains once a sufficiently large cluster is formed (explored in Chapter 3). Clusters of DUPC and cholesterol can define L_d domains and are clustered using a 7.0 Å cutoff. These distance cutoffs are selected to accurately capture the growth of the largest lipid domains during the phase separation process.

The time dependence of a phase separation scales as $n(t) \propto t^{\alpha}$ where n is the number of lipid tails or cholesterol assigned to the domain. The growth coefficients measured in time-resolved spectroscopy in a variety of experimental conditions have been observed in a range of $0.15 \leq \alpha \leq 1.0$.[267] Typical values of α manifest Ostwald ripening or coalescence mechanisms of domain formation depending on whether the system is composed of approximately one phase of ≤ 30 or $\geq 70\%$ (ripening; $\alpha = 1/3$) or one phase between 30% and 70% (coalescence; $\alpha = 1/2$).

Order parameters of lipids can be examined as a function of n, the number of intra-leaflet domain lipid and cholesterol tails. Likewise, the order parameters and number (m) of lipid tails and cholesterol in the opposing leaflet that make inter-leaflet contact with the intra-leaflet domain of n lipids can also be examined. This is done using

a distance cutoff from any lipid or cholesterol in the intra-leaflet domain to any lipid or cholesterol in the opposing leaflet. The size of intra-leaflet domains, inter-leaflet contacts of the same lipid type with the domain, and the order parameters of these lipids can be used together to create a detailed description of domain structure with sufficient sampling. Figure 2·4 illustrates some potential clusters of DPPC and cholesterol and maxima and extrema in n and m.

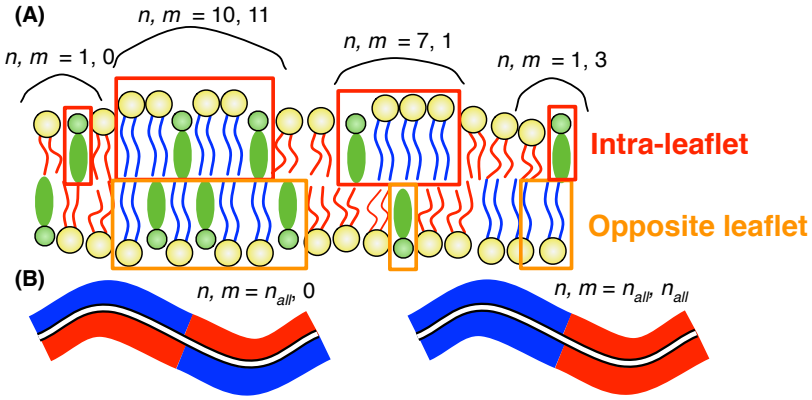

Figure 2·4: (A) Example clusters of n intra-leaflet lipid tails and m inter-leaflet contacts of DPPC (blue tails) and cholesterol (green) in a mixture with the unsaturated lipid DUPC (red tails) and (B) Extrema in size of intra-leaflet cluster and inter-leaflet leaflet contacts where n_{all} is the number of DPPC lipid tails and cholesterol in a leaflet.

2.1.7 Lipid overlap between leaflets

The aforementioned domain clustering method can be used to gain an impression of overlap between lipid domains via examination of $p(n, m)$. However, this measurement is particularly sensitive to the arbitrary cutoff used to determine the number of inter-leaflet lipids and cholesterol in contact, m. An alternative approach to measuring the overlap of DPPC (or DUPC) and cholesterol of the same type between leaflets is to perform a Monte Carlo (MC) integration of the Voronoi tessellations of the lipid bilayer. The fractional area occupied by lipids and cholesterol occupying the space in the xy-plane across leaflets, Λ, is evaluated using M test points for MC integration per frame to evaluate the sum

$$\Lambda = \frac{1}{M}\sum_{i}^{M}(x,y)_i \tag{2.5}$$

$$H(x,y)_i = \begin{cases} 0, (x,y)_i \notin T^{upper}_{DPPC+Chol} \text{ or } (x,y)_i \notin T^{lower}_{DPPC+Chol} \\ 1, (x,y)_i \in T^{upper}_{DPPC+Chol} \text{ and } (x,y)_i \notin T^{lower}_{DPPC+Chol} \end{cases} \tag{2.6}$$

where Λ is counted as the number of MC points $(x,y)_i$ that fall within tessels of DPPC or cholesterol in the xy-plane of upper and lower leaflets ($T^{upper}_{DPPC+Chol}$ and $T^{lower}_{DPPC+Chol}$) out of the total test points. To calculate the overlap of a random mixture Λ_{random} the chemical identity of lipids within each tessel are randomly shuffled and Λ is re-evaluated. Figure 2·5 illustrates how Λ is calculated.

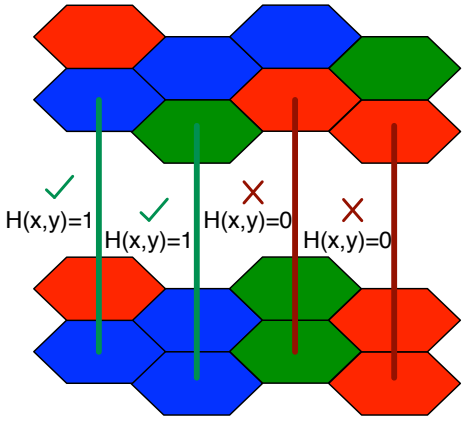

Figure 2·5: Illustration of Monte Carlo integration to solve for Λ on a representative Voronoi tessellation of a DPPC (blue), DUPC (red), and Chol (green) molecules.

2.2 Lipid-Lipid and Lipid-Protein Interaction Analysis

2.2.1 Hydrogen bonds

Within the membrane, the majority of lipid tails contain an ester group, providing a carbonyl and alkoxy oxygen available for accepting a hydrogen bond. Likewise, all lipid head groups contain polar groups that form hydrogen bonds with water. PC head groups in particular provide a phosphate group for hydrogen bond acceptance. Cholesterol has an alcohol group that may form hydrogen bonds on the membrane surface as well, which resides at approximately the same depth in the membrane as

lipid ester groups. These polar groups can form specific interactions with proteins, particularly lysine and arginine residues,[268] of which there are several are present in C99. Though hydrogen bonds observed in non-polarizable force fields are generally inaccurate, it is still useful in some contexts to analyze the hydrogen bonds observed in fixed-charge force fields.[269,270] We have done this by using a somewhat generous 2.5 Å distance cutoff criterion between the donated hydrogen and the accepting oxygen and a 150-180 degree angle criterion for the acceptor-hydrogen-donor angle.

2.2.2 Crick angles

The relative orientation of two or more protein helices has been a feature of interest for both characterization and design of protein-protein complexes.[271] The two Crick angles between two protein helices are defined by (1) the angle formed by the vector originating from the axis of the first helix to the alpha carbon (Cα) of interest to the vector from the axis of the first helix to the second helix, and (2) the angle of the vector originating from the axis of the second helix to the Cα of interest with the vector from the axis of the second helix to the first helix. For the C99 homodimer, a particular alpha carbon of interest, Gly33, which sits at the center of the GxxxGxxxG glycine zipper defining the stable Gly-in dimer motif, may be used to define the C99-C99 Crick angles.[113] The tail of the vectors may be defined as the center of geometry of the alpha carbons of residues 31-35, defining the center of the helical turn. Figure 2·6.A illustrates this definition of the two Crick angles in the C99 homodimer.

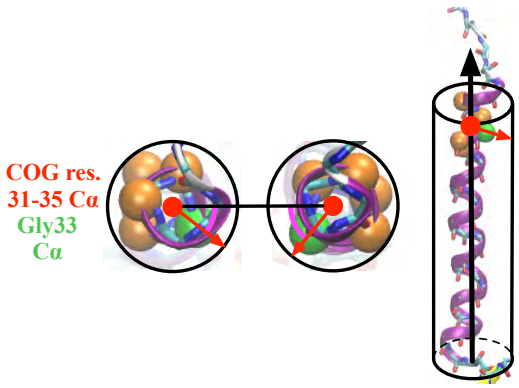

Figure 2·6: Crick angles of C99 homodimer defined with Gly33 alpha carbon (green) and center of geometry of residues 31-35 alpha carbons (orange and green).

2.3 C99 order parameters

2.3.1 C99 helical propensity

Secondary structures in proteins are stabilized by hydrogen bonds involving C=O and N-H in the protein backbone. Alpha helices are stabilized when the C=O from the i^{th} residue accepts a hydrogen bond from the N-H of the $i^{th}+4$ residue, and the substantially more rare 3_{10} and π helices are formed when the N-H donor is the $i^{th}+3$ and $i^{th}+5$ residue. The helical propensity of residues in C99 can be of interest in the TMD due to the glycine repeat of Gly37Gly38 that breaks the helix, creating a hinge. C99 extra-membrane domains can adopt stable and metastable helices depending on system conditions. We define the helical propensity of the i^{th} residue based on the likelihood of whether the residue donates or accepts a hydrogen with any of the $i^{th}-(3,5)$ or $i^{th}+(3,5)$ residue. The same 2.5 Å H-O distance and 150-180 degree N-H-O angle criterion is used here to define a hydrogen bond.

2.3.2 Residue insertion to lipid bilayer

The insertion depth of residues beneath the membrane surface, commonly described using the lipid head groups, provides a simple measure for examining the location of residues. The membrane surface in explicit solvent simulations is defined using the mean z-axis position of lipid phosphates in each leaflet, and in GBSW implicit solvent simulations[272] are defined using the beginning of the polarizable region. The insertion depth is defined by the residue alpha carbon height above the surface, in which negative values specify how far beneath the surface the alpha carbon is inserted. Residue Lys16 of C99 in particular is used as a probe of JM domain insertion in simulations of $C99_{16-55}$.

2.3.3 C99 domain angle order parameters

The structure of the C99 TM domain and JM domain can be captured by definition of a few essential angles between domains. The TMD tilt angle, θ, is defined as the 0-90° angle between the vector that best-fits the heavy backbone atoms of residues 30-52 and the membrane normal (Figure 2·7.A). The 0-90° TMD hinge angle, κ, which is present due to the glycine repeat Gly37Gly38 which can disrupt the TMD alpha helix, is defined by the angle between the vectors that best-fit the heavy backbone

atoms of residues 30-37 and residues 38-52 (Figure 2·7.B). The xy-plane JM domain-GxxxG face angle, ϕ, describes the relative orientation of the JM domain to the C99 GxxxG face if the JM domain resides on the bilayer surface over 0-360°. The GxxxG face vector is defined with the xy-plane center of geometry of residues 31-35 alpha carbons as the tail and the alpha carbon of Gly33 as the head. The JM domain vector is defined as the xy-plane best fit of heavy backbone atoms of residues 17-24, with the head oriented toward Leu17 and the tail oriented toward Val24 (Figure 2·7.C).

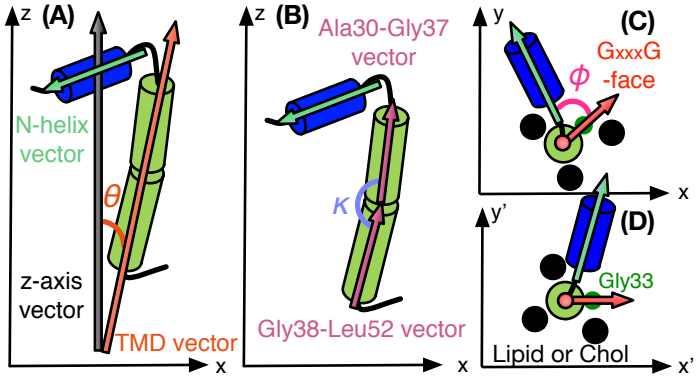

Figure 2·7: Cartoon representations of (A) TMD tilt angle (θ),(B) Gly37Gly38 hinge angle, (C) angle defining relative orientation of the JM domain and GxxxG director vector (ϕ), and (D) rotation about z-axis to align GxxxG director vector along the x'-axis.

2.3.4 C99 complex contacts and density around GxxxG face

Contacts between C99 and other molecules were counted using a 5 Å cutoff distance cutoff between any heavy atom of a C99 residue or any heavy atom of a lipid or cholesterol. The residence time between C99 and lipids or cholesterol is evaluated to determine the distribution of lifetimes for complexes between these molecules and to discriminate long- from short-lived complexes. Significantly long-lived cholesterol or lipid complexes with C99 can reveal the nature of favorable interactions between cholesterol and C99. Of these long-lived complexes, we translate the xy-plane positions of complexed molecules such that they are oriented around the center of the C99 residues 31-35 alpha carbons at (0,0) and rotated such that the Gly33 alpha carbon points along the positive x-axis, defining the new coordinate system x', y'. The transformed coordinates used to represent the complexed molecules are illustrated in Figure 2·7.D.

2.3.5 C99 homodimer distance and handedness

Much like the handedness of protein alpha helices, the superhelix formed by protein aggregates can have a handedness as well. To define the handedness of the C99 homodimer, we employ the dihedral formed by the alpha carbons of Gly29 and Gly37 in both C99s, with the hinge between Gly37 and Gly38 (Figure 2·8). The distance between these homodimers about this dihedral is described by the distance between the center of geometry of the alpha carbons of residues 31-35.

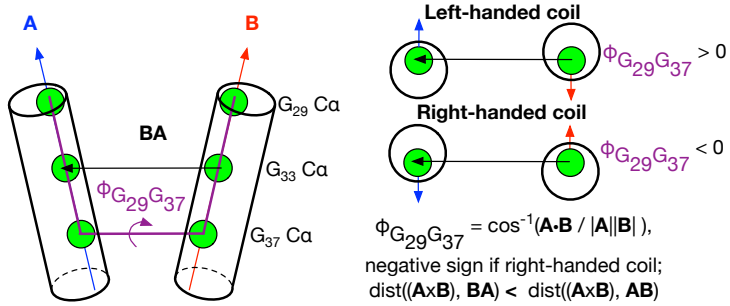

Figure 2·8: Cartoon representation of dihedral angle defining handedness of dimer along the C99 homodimer GxxxG zipper using Gly 29, 33, and 37 of the C99 homodimer.

2.3.6 Software and Molecular Dynamics Methods

Throughout this thesis, the CHARMM36 force field[273–275] is used for all-atom simulations and the MARTINI 2 force field is used for coarse-grained simulations. MD integrator, thermostat, barostat, and cutoff calculation schemes vary in each study presented, and are described within each chapter. Likewise, several molecular dynamics simulation software packages are used: GROMACS,[276,277] CHARMM,[278] and GENESIS.[279,280] One common feature throughout all work presented is the use of anisotropic pressure coupling schemes in all barostats, in which the x- and y- dimensions are constrained to each other and the length of the x-(y-)edge and z-edge are unconstrained.

All analysis methods described herein were enabled through use of NumPy+SciPy,[281] the MDAnalysis python library,[282,283] which is built on NumPy+SciPy and Cython.[284] All figures were created using Matplotlib,[285] Omnigraffle, Adobe Illustrator, and Visual Molecular Dynamics.[286,287]

2.3.7 Replica Exchange with Solute Tempering

The phase space of an all-atom molecular system is always defined by many potential barriers which often make sampling of the phase space take a prohibitively long time for even simple physiologically-relevant systems via MD simulation. Replica Exchange Molecular Dynamics (REMD)[288] is a straightforward methodological approach that has been remarkably effective in enhancing the sampling of phase space in MD simulations for the past 20 years.[289] REMD involves running multiple MD replica trajectories of the same system at various different Hamiltonians or thermodynamic conditions in which a single parameter is tempered such that important free energy barriers in the system will be lowered to enhance sampling within (classically, the temperature is chosen). To ultimately enhance the exploration of phase space in the Hamiltonian of interest (classically, the lowest temperature replica), there is a periodic attempt to swap the Hamiltonians or thermodynamic conditions of pairs of MD trajectories. The Metropolis-Hastings criterion defines the acceptance probability to accept a proposed swap between Hamiltonians or thermodynamic states of two trajectories if the potential energy in two trajectories are similar enough. In the case of REMD where the temperature is tempered, the Metropolis-Hastings acceptance probability is defined as

$$p^{i\leftrightarrow j} = \min\left(1, e^{(U(q_i)-U(q_j)(\frac{1}{k_{\mathrm{B}}T_i}-\frac{1}{k_{\mathrm{B}}T_j})}\right). \tag{2.7}$$

where i and j are the indices of replica trajectories attempting to swap Hamiltonians or thermodynamic conditions. Though temperature REMD has seen widespread use and success over many years, many methods using alternative modifications to the Hamiltonian have been used in REMD simulations have been used successfully. The most popular of these alternative methods is Replica Exchange with Solute Tempering (REST), in which molecular interactions between two parts of the system, the *solute* and the *solvent*, are tempered by effective temperatures in each m^{th} Hamiltonian which scale solute-solute and solute-solvent interactions by a factor relative to ratio of T_0/T_m. Here, T_0 is the effective temperature of the 0^{th} Hamiltonian, in which the interactions are not scaled at all.

Effective temperatures are used in REST because the derivation of the proper exchange criterion is straightforward.[290,291] Recently, REST was extended to a more generalized form in which more than just solute and solvent atoms are defined, but

components of the system potential can be specifically defined as the solute and solvent of the system.[292] For example, in the generalized Replica Exchange with Solute Tempering (gREST) method, dihedrals and Lennard-Jones interactions but not charge interactions on a protein, might be selected as the solute with the rest of the system defined as the solvent solvent to avoid sampling strange conformations and non-zero net charges that may be present in a Hamiltonian of a high effective temperature.

The potential energy of each system in REST is

$$U_{m,i}^{REST} = \frac{T_0}{T_m} U_{solute-solute}(q_i) + \sqrt{\frac{T_0}{T_m}} U_{solute-solvent}(q_i) + U_{solvent-solvent}(q_i) \qquad (2.8)$$

for the i^{th} replica at effective temperature T_m, and potential energies correspond to the current system conformation in trajectory i, $U(q_i)$. gREST has been shown to be particularly useful for sampling the phase space of transmembrane homodimers, for which raising the system temperature is a poor choice for sampling due to the substantial changes in lipid structure and potential dissolution of the lipid bilayer due to high temperatures in simulation.[293]

Chapter 3

Critical Size Dependence of Domain Formation Observed in Coarse-Grained Simulations of Bilayers Composed of Ternary Lipid Mixtures

3.1 Introduction

In molecular dynamics simulations, periodic boundary conditions (PBC) are used with the knowledge that observed thermodynamic and kinetic properties may depend on the finite size of the system.[294–296] In the case of lipid bilayer simulation, PBC effects were first investigated in the context of the spectrum of membrane surface undulations. Lindhal and Edholm found that the x- or y-edge length must be 20 nm or longer, and the system must be equilibrated for 10-100 ns to develop the longest wavelength undulatory modes required to fully characterize the bilayer surface. Klauda et al. found a strong dependence of lipid diffusion on PBC size,[297] though Castro-Román et al. found the effect of PBC on single and multilamellar bilayer structures to be negligible.[298] Additionally Camley et al. have developed a Saffman-Delbrück hydrodynamic model validated by all-atom and coarse-grained simulations, suggesting that lipid bilayer simulations must employ PBCs with near-100 nm edge lengths and thick hydration layers to capture essential bilayer structural fluctuations.[299] These studies suggest that PBCs strongly perturb lipid bilayer fluctuations and dynamics. In the case of domain formation by simple liquid mixtures, Scott et al.[300] have investigated the nature of system size and PBC effects, and Huang et al. investigated system size effects of phase separation in binary mixture lattice models.[301] However, the scaling of PBC effects observed in studies of liquid-liquid phase separation using molecular dynamics simulation do not appear to have been addressed in any context.

We performed molecular dynamics simulations and structural analysis of domain

formation in the well-studied di-C16:0 PC (DPPC), di-C18:2 PC (DIPC), and cholesterol (CHOL) (35:35:30), ternary lipid bilayer mixture using MARTINI coarse-grained lipid models over a wide range of system sizes. Our analysis of domain formation as a function of system size suggests that systems with less than 1480 lipids (740 lipids per leaflet) may not form macroscale domains defined by a distinguishable interface. Moreover, the convergence of structural properties is found to require systems of 10,000 lipids or more. Additionally, via microscopic structural analysis of transleaflet aggregates of L_o domain-forming lipids, we observe the coexistence of micro- and macroscopic ordered domains in systems of sufficient size. To describe the balance of finite size, composition, temperature, and interaction energy on phase separation and domain shape, we develop and apply an analytical Flory-Huggins model parameterized using simulation data and interaction energies derived from experiment. These findings provide insight into the role of system size in determining the morphology and stability of domain formation in multicomponent lipid bilayers and guidance for future modeling studies. Additionally, this work suggests that finite size effects may be critical to the study of phase separation in other multi-component biological systems, such as the formation of the protein coronae, protein fibrils, endoplasmic granules, and vesicles.

3.2 Materials and Methods

3.2.1 MD simulation

Fully atomistic simulations of lipid bilayer phase separation from random mixtures are not feasible with current enhanced sampling methods and computing hardware. As such, we employ the widely-used MARTINI coarse-grained force field, which simplifies the energy landscape of the mixture, accelerates dynamics relative to atomistic models, and provides an order of magnitude gain in both computational efficiency for integration time step and number of particles (Fig. 3·1). While approximate, the MARTINI model has been shown to capture essential properties of a variety of thermodynamic phases, making it useful for understanding structural transitions in lipid membranes.[302,303]

The Melo et al. force field parameters were used for CHOL.[252] DPPC, DIPC, water, Na, and Cl were modeled using the MARTINI v2.0 parameters.[304] Approximately 24 effective solvent molecules per lipid molecule were used so as to fully solvate each lipid

headgroup.[305] To avoid spontaneous freezing of water, 10% of the waters were modeled using anti-freeze parameters. 150 mM NaCl salt was used to model a physiological salt concentration.

All ternary mixtures were prepared by random placement of DPPC, DIPC, and CHOL on a square lattice bilayer with a layer of solvent using the insane.py tool.[306] Steepest descent minimization and MD were performed using the GROMACS 5.0.4 simulation suite.[276] Leap frog integration with 20 fs time step was used. Simulation parameters largely correspond to those of the 'qcommon" parameter set described by De Jong et al.[307] A timestep of 20 fs using leap-frog integration with a 1.2 nm 'group' neighbor list updated every 10 steps was used for integration. Non-bonded interactions are handled using the Gromacs shifting function between 0.9-1.2 nm and 0.0-1.2 nm for Lennard-Jones and Coulomb interactions, respectively. The velocity-rescaling thermostat was used with a coupling time of 1 ps with 295 K temperature, and the semi isotropic Berendsen barostat was used with 1 atm pressure, a coupling time of 2 ps, and a compressibility of $3\text{x}10^{-4}$ bar^{-1}. Coordinates and thermodynamic data were recorded in 1 ns time intervals.

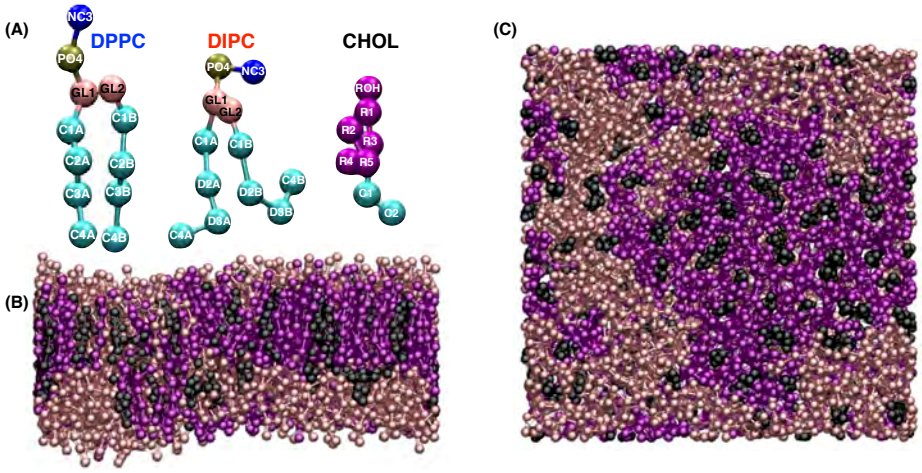

Figure 3·1: (A) MARTINI model lipids and cholesterol with site labels. Slab (B) and top (C) views of N=508 lipid membranes at 11 μs where DPPC, DIPC, and CHOL are pink, purple, and black, respectively.

3.2.2 Analysis

Lipid mixing entropy (S_{mix}) was computed using nearest neighbors determined via Voronoi tessellations of lipid head groups, represented by the PO4 beads of DPPC and DIPC and the ROH bead of CHOL. The Nelson-Halperin 2D bond-orientational

order parameter (Ψ_6) was computed based on the carbon chain of each DPPC, DIPC, and CHOL. Positions of DPPC and DIPC chains were represented by C2A and C2B, and D2A and D2B beads, respectively. The CHOL chain was represented by the centroid of the R1, R2, R3, R4, and R5 beads. The liquid crystal order parameter (P_2) was measured using a vector between GL1-C4A, GL2-C4B beads for DPPC and DIPC and the z-axis as the director. Details regarding the calculation of Ψ_6 and P_2 are provided in Chapter 2.

To identify intra-leaflet aggregates of DPPC and CHOL carbon chains, we performed a hierarchical distance-based geometric clustering analysis. We counted DPPC and CHOL carbon chains as being part of an aggregate if the C2A, C2B, or centroid of the R1, R2, R3, R4, and R5 beads were within 5.8 Å of any other beads. The inter-leaflet contacts were counted if the C4A, C4B (DPPC and DIPC) or C2 (CHOL) beads in the opposing leaflet were within 7.0 Å of any bead defining the aggregate. For analysis of DIPC and CHOL aggregates, equivalent criteria for cluster identification were used except intra-leaflet aggregates were identified using a 7.8 Å distance cutoff.

3.3 Results and Discussion

3.3.1 Achieving structural and spatial equilibrium

To study the formation of phase separated domains we employ a traditional phase separating mixture of DPPC, DIPC, and CHOL (35:35:30).[302,308–316] We performed coarse-grained MD simulations at 295 K initiated from random spatial placement of lipids into a bilayer geometry for a wide range of system sizes. Five 11 μs trajectories were produced for bilayers composed of N=240, 508, 1056, 2046, 3040, and 5406 molecules. 330 μs of sampling were accumulated for this study. These systems reach an apparent equilibrium in their structural properties by 6 μs, as measured by the time-dependence of the lipid mixing entropy (S_{mix}), the norm of their 2D bond-orientational order parameter ($|\Psi_6|$), and liquid crystal order parameter (P_2) (Fig. 3·2). The time evolution of the instantaneous order parameters suggests that the system dynamics is essentially stationary after 6 μs.

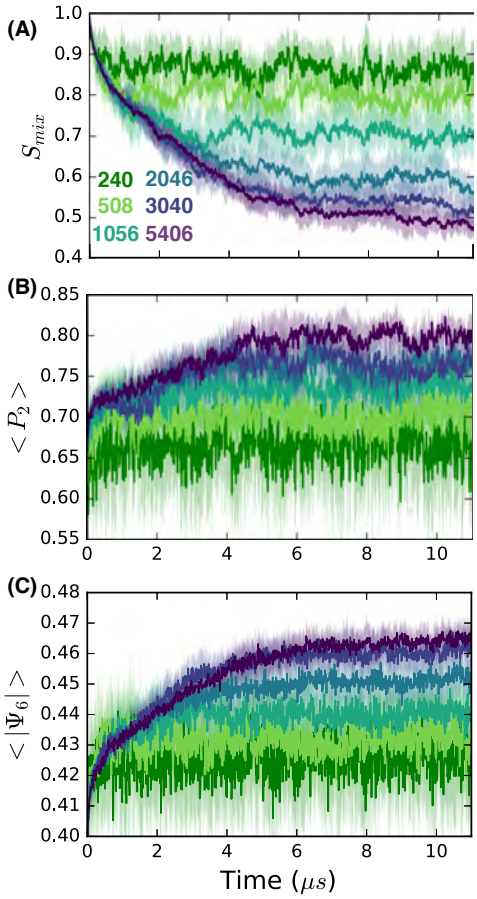

Figure 3·2: Mean and standard deviations in (A) mixing entropy (B) liquid crystal order and (C) absolute value of 2D bond-orientational order averaged over five replicate trajectories.

3.3.2 Critical system size is required for phase separations

The average values of the three order parameters were computed as a function of system size using the dynamics in the observed stationary regime (Fig. 3·3). The average value of each order parameter displays a sigmoidal transition as a function of the log of system size, with a miscible state for small N and a phase separated state for large N. The average order parameters are observed to asymptotically converge at N≈10,000, similar to that observed by Huang and Feigenson for binary lattice mixtures.[301] We identify a critical size (N_c) for each order parameter as the inflection point of the order parameter as a function of system size. We find that for the three order parameters employed, $N_c^{S_{\text{mix}}}$=994, $N_c^{P_2}$=870, and $N_c^{|\Psi_6|}$=1480, close to the N_c=1000 previously predicted by Huang and Feigenson.[301]

We observe that small equilibrated lipid bilayers up to N=1056 do not form macroscopic phase separated domains spanning the system. Larger systems ($N \gtrsim 1480$) appear to form phase separated domains of size limited by the PBC employed. When $N \leq 1056$, liquid ordered domains do not span the system to form striped domains (Fig. 3·4). Based on these observations, we say that $N_c^{|\Psi_6|}$=1480 is the minimum system size required to simulate the formation of phase separated lipid domains. The correlation length of lipid tail orientational order ($\Psi_6(r)$) is apparently short and indicates that both phases retain characteristics of the liquid state, but signifies that a minor population of the L_o phase exhibit orientational correlations over a small, nanoscopic length similar to the lipid gel phase (Fig. 3·5).

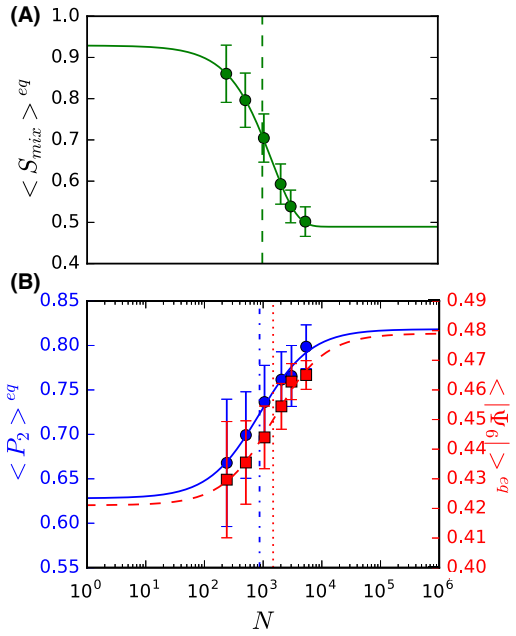

Figure 3·3: Mean and standard deviations at equilibrium of (A) S_{mix} and (B) P_2 of DPPC (blue) and $|\Psi_6|$ of DPPC (dashed-red) averaged over five replicate trajectories. Inflection points are identified by dashed (S_{mix}), dash-dotted (P_2) and dotted ($|\Psi_6|$) lines.

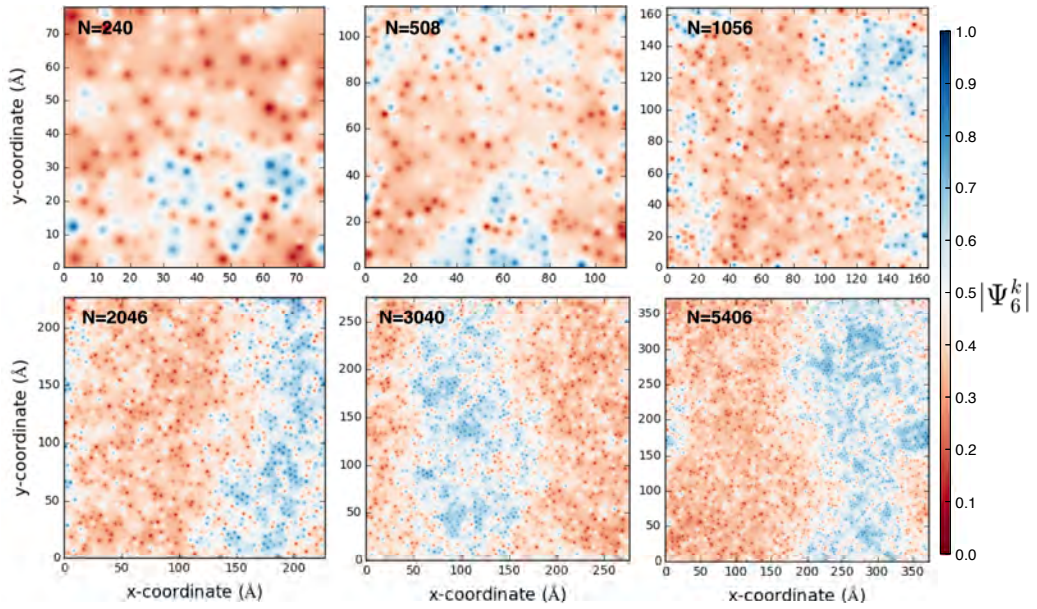

Figure 3·4: Linearly interpolated measurements of absolute-valued 2D bond-orientational order parameter for one leaflet at 6 microseconds in different systems.

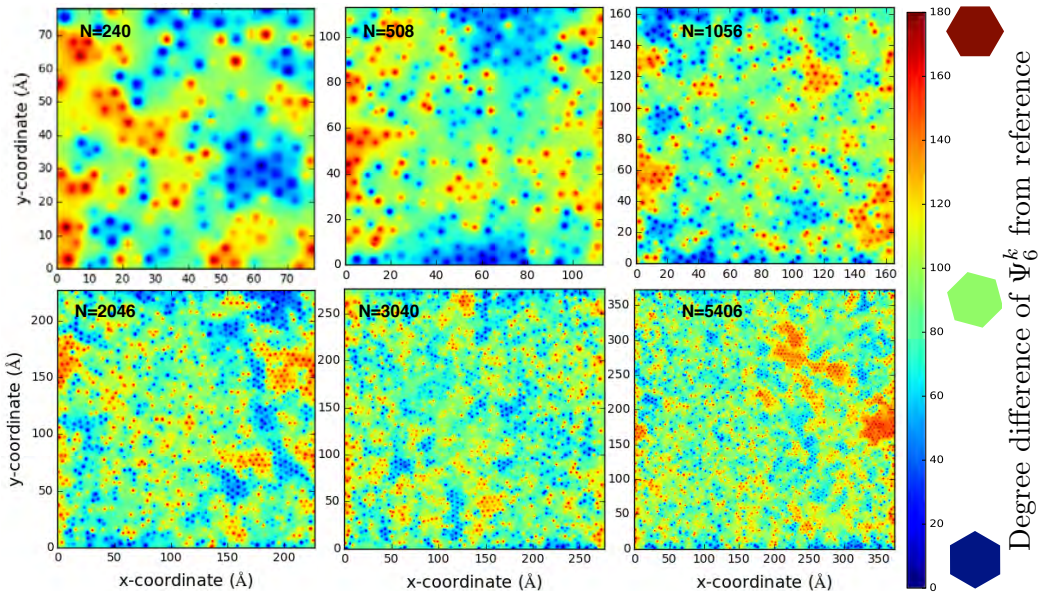

Figure 3·5: Linearly interpolated measurements of the 2D bond-orientational order of C2A, C2B, D2A, D2B, and the centroid of R1, R2, R3, R4, and R5 beads for one leaflet at 6 microseconds in systems of various size. RGB colormap from 0 degree to 180 degree angle of orientation vector from the x-axis.

3.3.3 Binary Flory-Huggins theory defines critical system size for domain formation

The phenomenon of phase separation in lipid bilayers has been considered using a variety of Flory-Huggins type models. Phase diagrams were computed for models of binary[317] and ternary[318] mixtures that included an order parameter based treatment of the liquid-gel melting transition. Additionally, a Flory-Huggins type model has been used to develop a theory of line tension in ternary lipid mixtures, finding the line tension to depend on the composition of the lipid mixture.[319] Finally, McConnell and coworkers developed a model for ternary lipid mixtures in which two components combine and interact interact with the third component.[320] While this last approach captures certain aspects of phase separation in ternary lipid mixtures noted in experiment, it fails to reproduce the more complex phase behavior captured by the more detailed models.

To gain insight into the underlying thermodynamic driving forces, we develop and employ a minimal model for the ternary lipid mixture in that it models the ternary mixtures in terms of two fluid components and bears resemblance to the model of McConnell and coworkers[321] and to the original presentation of the theory.[322] It is used as a minimal model to provide insight into the importance of system size on phase separation and to determine the thermodynamic driving forces determining the minimum system size required to observe phase separated domains. The model lattice consists of two types of lipids sites (O and D), which may be mixed in the miscible state or be phase separated. Furthermore, we assume that the phase separated states may take the form of a stripe domain (with lipids partitioned along a linear interface) or a dot domain (with one lipid partitioned into a circular region). The free energies of mixed, stripe domain, and dot (circular) domain states are

$$F_{\text{mix}} = \frac{z}{2} n_{\text{O}} w_{\text{OO}} + \frac{z}{2} n_{\text{D}} w_{\text{DD}} + N z \chi x_{\text{O}} x_{\text{D}} - T S_{\text{mix}} \tag{3.1}$$

$$F_{\text{stripe}} = \frac{z}{2} n_{\text{O}} w_{\text{OO}} + \frac{z}{2} n_{\text{D}} w_{\text{DD}} + \frac{2L}{d} \chi \tag{3.2}$$

$$F_{\text{dot}} = \frac{z}{2} n_{\text{O}} w_{\text{OO}} + \frac{z}{2} n_{\text{D}} w_{\text{DD}} + \frac{2\pi\sigma}{d}\chi \tag{3.3}$$

where w_{OO} is the bond energy of two interacting O sites, w_{DD} is the bond energy of two interacting D sites, σ is the radius of the dot domain, d is the lattice spacing, z is the coordination number of each lattice site, L is the edge length of the system, n_{O} and n_{D} are the numbers of O and D sites, and χ=$(w_{\text{DO}} - (w_{\text{DD}} + w_{\text{OO}})/2)$. The mixing entropy is written S_{mix}=$-k_{\text{B}}N(x_{\text{D}} \ln x_{\text{D}} + (1-x_{\text{D}}) \ln(1-x_{\text{D}}))$. $\frac{2L}{d}\chi$ is the line tension for the two linear interfaces formed in the stripe domain, and $\frac{2\pi\sigma}{d}\chi$ is the line tension for a circle.

These equations can be simplified by noting that $\frac{L}{d}$=$\sqrt{N}$ so that $\frac{2L}{d}\chi$=$2\chi\sqrt{N}$. For the dot interface, imposing $\pi\sigma^2$=$x_{\text{D}}L^2$ with $\frac{L}{d}$=$\sqrt{N}$ leads to $\frac{2\pi\sigma}{d}\chi$=$2\chi\sqrt{N}\sqrt{\pi x_{\text{D}}}$. Additionally, we recognize that E_0=$\frac{z}{2}n_{\text{O}}w_{\text{OO}} + \frac{z}{2}n_{\text{D}}w_{\text{DD}}$ in each expression, and as such will not contribute to the difference in free energy between competing phases. These simplifications lead us to the expressions

$$F_{\text{mix}} = E_0 + Nz\chi x_{\text{D}}(1-x_{\text{D}}) + Nk_{\text{B}}T(x_{\text{D}} \ln x_{\text{D}} + (1-x_{\text{D}}) \ln(1-x_{\text{D}})), \tag{3.4}$$

$$F_{\text{stripe}} = E_0 + 2\chi\sqrt{N}, \tag{3.5}$$

$$F_{\text{dot}} = E_0 + 2\chi\sqrt{N}\sqrt{\pi x_{\text{D}}} \tag{3.6}$$

where N is the number of molecules in a monolayer, x_{D} is the mole fraction of molecules that form the liquid disordered phase (L_d), ranging from 0 to 0.5, x_{O}=$1-x_{\text{D}}$ is the mole fraction of molecules that form the liquid ordered phase (L_o), z is the coordination number of each molecule, and E_0 is a constant for interaction energies. When χ>0 it is possible for F_{stripe} or F_{dot} to reach a lower energy than F_{mixed}. The stripe phase is more stable than the dot phase for $1/\pi$<x_D<$1-1/\pi$, and $x_D = 1/\pi$ defines the phase boundary between dot and stripe phases. In our simulations x_{D}≈0.45, determined using number of edges between lipid types determined in Voronoi tessellations via the expression $x_{\text{D}} = \frac{N_{\text{DIPC-CHOL}}}{N_{\text{DIPC-CHOL}}+N_{\text{DPPC-CHOL}}} + \frac{N_{\text{DIPC}}}{N}$, and we observe the stripe phase, consistent with the predictions of the model. A most important feature to recognize in this model is that the phase transition between miscible and immisci-

ble states can happen as the number of lipids in the layer, N, in the system increases (Fig. 3·6, 3·7).

This model enables prediction of N_c from experimentally determined χ, as well as determination of χ values from N_c obtained by simulation (Fig. 3·7B). This can be done by the definition of the phase boundaries defined at a the critical size, N_c. At F_{mix}-F_{stripe}=0,

$$N_c^{\mathrm{mix}\leftrightarrow\mathrm{stripe}} = 4\left(zx_{\mathrm{D}}(1-x_{\mathrm{D}}) + \frac{k_{\mathrm{B}}T}{\chi}\left[x_{\mathrm{D}}\ln x_{\mathrm{D}} + (1-x_{\mathrm{D}})\ln(1-x_{\mathrm{D}})\right]\right)^{-2}, \quad (3.7)$$

and at F_{mix}-F_{dot}=0

$$N_c^{\mathrm{mix}\leftrightarrow\mathrm{dot}} = 4\pi x_{\mathrm{D}}\left(zx_{\mathrm{D}}(1-x_{\mathrm{D}}) + \frac{k_{\mathrm{B}}T}{\chi}\left[x_{\mathrm{D}}\ln x_{\mathrm{D}} + (1-x_{\mathrm{D}})\ln(1-x_{\mathrm{D}})\right]\right)^{-2}. \quad (3.8)$$

The χ values corresponding to our simulations occur near the inflection point in $\chi(N)$, suggesting a sensitive dependence of N_c on χ. The χ values reported here are likely larger than other well-studied mixtures in experiment, such as DPPC, DOPC (di-18:1 PC), and CHOL, due to substantial mismatch in degrees of tail saturation. This may explain the past difficulty in observing macroscopic phase separation of such mixtures in simulation studies.

There have been many previous studies of domain formation in ternary lipid mixtures using MARTINI as well as more fine-grained lipid force fields.[232,302,308–316,323–327] Some of the previous simulation work on this phenomenon employed system sizes substantially smaller than the critical minimum system size required for phase separation in this study.[178,232,309,311,312,325,326] As such, it is important to carefully consider how PBC may have influenced observations of phase behavior in these previous studies.

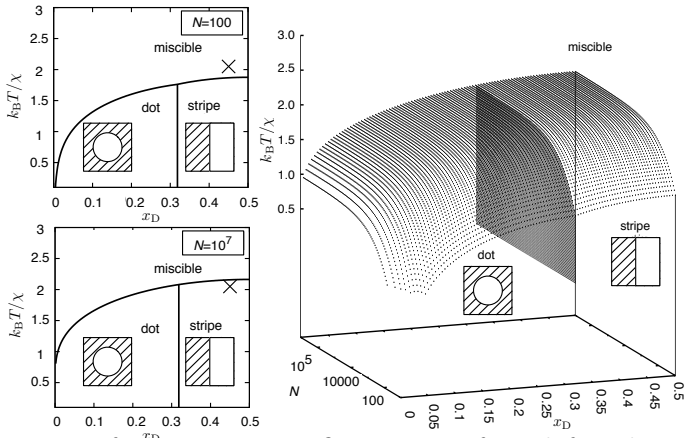

Figure 3·6: Lowest free energy configurations found for the Flory-Huggins model of mixed, stripe, or dot states at T=295 K and z=6 (to approximate realistic lipid packing). The "X" depicts the state of the system considered in this work, which is predicted to be in the miscible state for N=100 and stripe phase separated state for N=10^7 taken to be the thermodynamic limit.

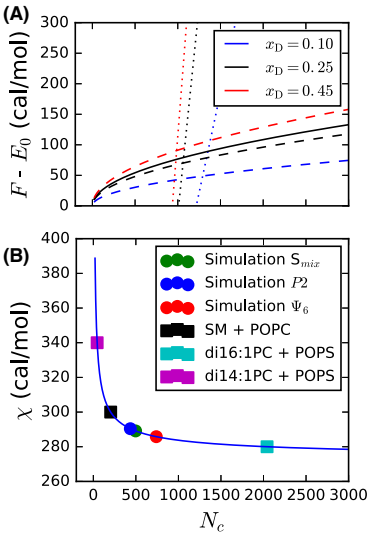

Figure 3·7: We demonstrate the dependence of system size, N, on the mole fraction, x_D. (A) Free energies of mixed (dotted), stripe (solid), and dot (dashed) phases when χ=2.90 cal/mol and T=295 K. z=6 to approximate realistic packing of lipids. (B) Solid line is the critical point between mixed and stripe phases in the Flory-Huggins model (Eq. 3.7) with x_D=0.45, T=295 K, and z=6. Circles are placed on the curve at critical sizes (N_c) obtained from simulation, while squares are placed on the curve at χ values derived by Almeida.[1] Simulation χ values are determined with a lattice spacing of 0.8074 nm and N=5406 with N_c determined from S_{mix}, P_2, $|\Psi_6|$.

3.3.4 Coexistence of micro- and macroscopic liquid ordered domains at equilibrium

To define domains of DPPC and CHOL aggregates we geometrically cluster intra-leaflet DPPC and CHOL carbon chains (of number n) and identify inter-leaflet contacts with DPPC and CHOL (of number m) at equilibrium. Through this analysis, we observe large separations in population between micro- and macroscopic domains once the system becomes large (Fig. 3·8A) By analyzing the number of carbon chains not associated to the largest intraleaflet cluster, we also find that L_d domains in small systems exhibit substantial impurities while L_o domains are similarly pure at all system sizes. Additionally, it appears that sampled values of n and m are linearly correlated, such that an aggregate of n intra-leaflet carbon chains will be in contact with a similar number of m inter-leaflet carbon chains. Analyzing aggregates of size $n+m$, we find microscopic domains as large as 250 carbon chains to be substantially ordered, forming a L_o domain (Fig. 3·8B). This coexistence of micro- and macroscopic domains stands in contrast to the scenario in which ternary mixtures *only* form micro- or macro domains as previously implied.[314,328,329] Similar observations have also been made based on binary mixture simulations of the Pink lattice model for lipid-lipid and lipid-protein mixtures, suggesting that microscopic phase separations can arise even when there is a vanishingly small amount of mismatching lipid.[223,224] Additionally, Javanainen et al. have identified the coexistence of microscopic L_o and L_d domains in all-atom simulations.[179]

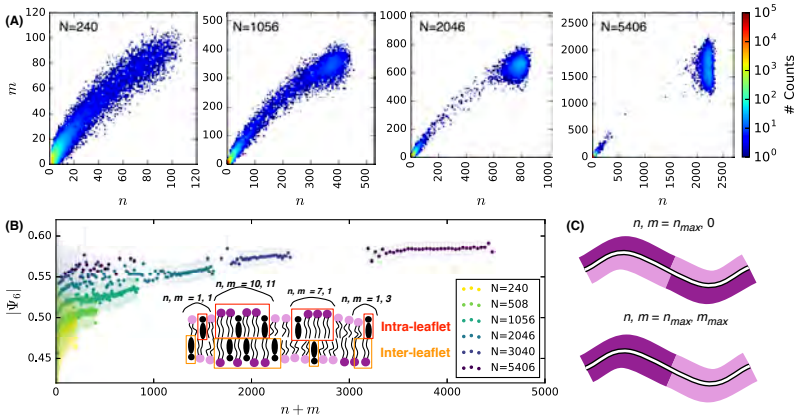

Figure 3·8: (A) Counts of intra- (n) and inter- (m) leaflet carbon chains in DPPC-CHOL aggregates at equilibrium. (B) Mean and standard deviations of $|\Psi_6|$ as dependent on the size of DPPC-CHOL aggregates. Inset illustration describes aggregates in an example configuration. (C) Illustration of extreme cases of registration and anti-registration.

3.3.5 Phases form unique complexes involving cholesterol

To characterize the structure of lipids within the simulated L_o and L_d domains, we provide a critical comparison with the liquid condensed phase of DPPC and CHOL monolayers, analogous to the L_o phase. Kim et al. observed that liquid condensed domains in mixtures of DPPC and CHOL exhibit a high degree of bond-orientational order and a ratio of 6:1 DPPC:CHOL, consistent with formation of a "tiled lattice" of cholesterol carbon chains each surrounded by six DPPC carbon chains.[257] Consistent with this view, we observe substantial bond-orientational order which visually differentiates the L_o and L_d domains (Fig. 3·9).

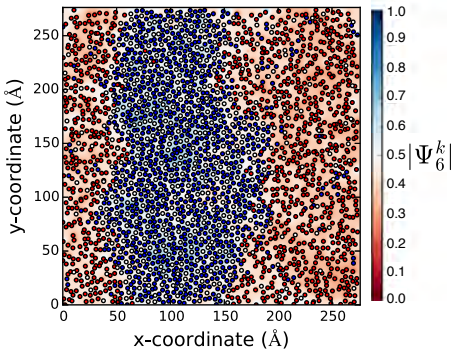

Figure 3·9: Coordinates of DPPC (blue, C2A C2B beads), DIPC (red, D2A, D2B beads), and CHOL (white, centroid of R1, R2, R3, R4 and R5 beads) in one leaflet at 6 μs for N=3040. $|\Psi_6^k|$ values are linearly interpolated.

Distributions of CHOL neighbors were evaluated via Voronoi tessellations, where DPPC:CHOL 6:1 ratios were found to be most prevalent in L_o domains (in which cholesterol only neighbors other cholesterol or DPPC). Approximately equal counts of 5:1 and 7:1 ratios were the next-most populous complexes (Fig. 3·10), the result of point defects in the membrane surface that facilitate bilayer undulations. These ratios are consistent with the spatial distributions observed by Kim et al.[257] in the liquid condensed phase. For smaller system sizes in the L_d phase, a 1:1 DIPC:CHOL ratio is found to be most prominent. As N increases, a second peak at 6:1 DPPC:CHOL develops (in the L_d phase), similar to that of DPPC:CHOL (in the L_o phase) (Fig. S7). We note that the L_o phase exhibits preferential formation of CHOL-CHOL dimers over monomers. This may be of interest in biological processes where CHOL-CHOL dimerization has been proposed to play a role.[229] An example of this is the case of amyloid precursor protein C99-CHOL dimerization which has been proposed to

promote the formation of Aβ_{42} and to compete with CHOL-CHOl dimerization.[6,330] In this scenario, C99-CHOL would be outcompeted by CHOL homodimerization in L_o domains, freeing C99 to interact with γ-secretase, thus forming Aβ. We will return to the topic of C99-CHOL interaction later in Chapter 5.[123]

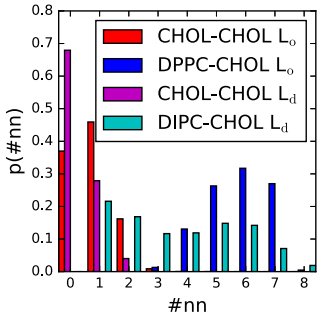

Figure 3·10: Cholesterol nearest neighbor distributions computed using Voronoi tessellation analysis at apparent equilibrium for N=5406. Cholesterol in L_o (L_d) domains are identified as cholesterols with no DIPC (DPPC) neighbors.

3.4 Conclusion

We have investigated the effects of system size on macroscopic phase separation in lipid bilayers. We find that for the commonly investigated ternary lipid mixture, 35:35:30 DPPC:DIPC:CHOL, the system size must surpass 1480 lipids to observe the formation of stripe domains. This minimal number of lipids required for domain formation is likely to be similar or larger for other phase-separating mixtures, a conjecture supported by the predictions of a simple binary Flory-Huggins model. The binary Flory-Huggins model predicts a critical system size for domain formation and offers insight into the role of temperature, interaction energies, and system size in the domain formation process.

We have observed the coexistence of macro- and microscopic L_o domains within a macroscopic domain-forming mixture, in contrast to earlier reports. We have also quantified the effect of inter-leaflet contacts on the formation of domains. Additionally, we observe the spatial distribution of DPPC and CHOL observed in L_o domains to be consistent with the formation of 6:1 DPPC:CHOL complexes. Similar complexes are observed in the L_d phase formed by DIPC:CHOL in sufficiently large systems. Finally, we observe the preferential formation of CHOL-CHOL dimers over monomers in the L_o phase.

Taken together these observations demonstrate the importance of finite size effects in lipid phase separations. The importance of this observation is two-fold. There is a need to consider finite size effects when modeling phase behavior in lipid mixtures that is experimentally observed on the thermodynamic scale. In addition, when considering the biological importance of phase separation, as in discussions of the existence and relevance of liquid-ordered domains, the observations made in this work suggest a lower limit on the size of domain formation in biological membrane.

Chapter 4

Regimes of Complex Lipid Bilayer Phases Induced by Cholesterol Concentration in Ternary Mixtures

4.1 Introduction

Mammalian plasma membranes tend to contain 1:3 to 1:1 ratios of cholesterol (Chol) to phospholipids,[331,332] though phospholipid membranes can accommodate approximately 66 mol% Chol[209–212] and this upper limit is approached in plasma membranes of astrocyte cells in Alzheimer's disease patients.[333,334] At high ($\gtrsim$40) mol% Chol modern fluorescence,[183,225] x-ray,[4,199] and AFM experiments[203,204] have shown that nanoscopic ordered and disordered domains coexist outside of the miscibility gap around 1:1:1 ratio mixtures, as L_o domains of tens of lipids can be stable in the L_d phase bulk membrane.[335] x-ray scattering experiments have revealed that 60 nm diameter domains of pure Chol domains can coexist with domains of saturated and unsaturated lipids at these high mol% Chol compositions.[175,202,226,227] Beyond the 66 mol% solubility limit of Chol in bilayers,[209–212] Chol forms anhydrous crystals in solution.[175,213]

Nanoscale resolution knowledge of both domain composition and phase in both membrane leaflets is currently limited. Strong registration of domains between lipid leaflets has been experimentally quantified,[336] however, this registration is only confirmed for macroscopic phase separations of symmetric bilayers, and likely does not occur in mixtures where smaller domains are observed due to complicated surface energies and inter-leaflet interactions. Many theoretical works have considered the inter-leaflet coupling of lipids and domains, and arguments in favor of inter-leaflet registration or anti-registration of domains have been presented. Preference of domains for local curvature of the membrane surface as well as inter-leaflet interaction between domains can significantly impact the free energy of the membrane. Small, microscopic domains

can form that preferably register or anti-register with domains of the opposing leaflet depending on the relative degree of local curvature.[337–344]

Typically, experimental approaches cannot discern the thermodynamic phase and degree of mixing of both lipid leaflets in bilayers of symmetric leaflet composition. Much work has been done to consider inter-leaflet interactions of domains using bilayers of strictly asymmetric leaflet composition, where inter-leaflet domain registration has been observed.[336,345–347] However, the methods employed, such as use of supported monolayers, may limit the generality of the conclusions of these studies. It is known that Chol strongly prefers to partition to regions of concave curvature.[348] That preferential partitioning may play a role in domain formation and registration.

MD simulations employing the MARTINI coarse grained (CG) model, capable of producing various thermodynamic phases of lipids[303,349] and lipid phase separation,[302,308–315,327,335,350,351] have provided structural insight to inter-leaflet domain interaction. Perlmutter et al. observed the enhanced local curvature of membranes in the presence of anti-registered domains[309] and Fowler et al. found that domain registration may occur via a two-step kinetic process of anti-registered domain formation preceding the formation of registered domains.[350] Additionally, Yesylevskyy et al. demonstrated the preferential partitioning of Chol to regions of locally higher curvature using simulations employing the MARTINI model.[352]

Here we investigate complex phase separation as a function of Chol concentration in ternary mixtures with di-16:0 PC (DPPC) and di-18:2 PC (DIPC) lipids, maintained at DPPC:DIPC 1:1 molar ratios, using CG molecular dynamics simulation employing the MARTINI model. Performing simulations at 0, 3, 7, 13, 22, 30, 42, 53, and 61 mol% Chol, we observe that Chol induces three regimes of domain structure at varying concentrations, denoted I) miscible, L_d phase, II) domain-registered, macroscopically phase separated L_o+L_d domain coexistence, and III) domain-anti-registered, microscopically phase separated coexistence of L_d domains with domains of a newly identified "cholesterolic gel" (S_{oc}) phase featuring "threads" of Chol.

Transitions between the three identified phases are observed to be dependent on Chol concentration with compositionally unstable mixtures separating regimes sampled at 7 and 42 mol% Chol. The mol% of Chol in DPPC:Chol and DIPC:Chol domains are inferred from the number of lipid-Chol contacts out of all contacts. We find DPPC:Chol domains to rapidly become saturated with Chol, achieving 30% DPPC-Chol contacts by 13 mol% Chol in the membrane, prior to any substantial association

of Chol with DIPC. The structure of DPPC, DIPC, and Chol as a function of the percentage of DPPC-Chol and DIPC-Chol contacts is reported in systems at each mol% Chol composition.
This work provides new insight into the role of Chol concentration in complex phase behavior observed and predicted in the past, and provides evidence for a new gel phase that may be thermodynamically stable in membranes of typical Chol concentration.

4.2 Materials and Methods

4.2.1 MD system construction

This mixture of DPPC, DIPC, and Chol in the MARTINI CG model is uniquely capable of forming macroscopic phase separation.[302,308–315,327,335,350,351] The Chol model of Melo et al. was used[252] and all other molecules employed the MARTINI v2.0 force field.[304] The insane.py script developed by the Marrink group was used to form three unique initial conditions for 0, 3, 7, 13, 22, 30, 42, 53, and 61 mol% Chol random bilayer mixtures, keeping DPPC and DIPC equimolar.[306] Effectively 38 waters per lipid were used, and 10% of these used MARTINI anti-freeze parameters to prevent spontaneous nucleation of ice droplets. NaCl at 150 mM concentration was used to approximate physiological salt conditions. We construct all systems with 3040 lipids, such that the PBC will not prevent the observation of domain formation and phase coexistence.[335]

4.2.2 MD Simulation

All simulations were performed with GROMACS 5.0.4.[276] Each initial configuration was minimized using the Gromacs steepest descent minimizer. Simulation parameters largely corresponded to the "common" parameter set described by DeJong et al.,[307] and simulations were performed with the same protocol as our previous work.[335] Non-bonded interactions used the Gromacs shifting function applied from 0.9 to 1.2 nm for Lennard-Jones and from 0.0 to 1.2 nm for Coulomb interactions. The velocity rescaling thermostat of Bussi et al. was used with a coupling time of 1 ps and a reference temperature of 295K,[353] as applied in many past studies of phase separation with this lipid mixture.[308,309,311,312,314,315,335] The semi-isotropic Berendsen barostat was used with 1 atm reference pressure, a coupling time of 1 ps, and $3\text{x}10^4$ bar^{-1}

compressibility, coupling x and y dimensions. The leap-frog integrator was used with a 20 fs time step, employing a "group" neighbor list with a 1.2 nm cutoff, updated every 200 fs. Three replicates of each system were simulated for 11 μs. One set of replicates representing each system condition used San Diego Supercomputer Center (SDSC) Comet resources via the Extreme Science and Engineering Discovery Environment (XSEDE) through startup allocation TG-MCB150142.[354] The other two sets of replicas used the Shared Computing Cluster administered by Boston University's Research Computing Services.

4.2.3 Analysis Details

To analyze the coordinates of lipid head groups in the MARTINI model, we define head groups as the PO4 bead of DPPC and DIPC and the ROH bead of Chol. Lipid tail groups are defined as C2A and C2B for DPPC, D2A and D2B for DIPC, and the centroid of R1, R2, R3, R4, and R5 for Chol. We use xy-plane Voronoi tessellations of DPPC, DIPC, and Chol head groups to determine S_{mix} and nearest neighbors, counting the number of DPPC-Chol and DIPC-Chol contacts in the membrane. Using these tessellations we infer the Chol composition of L_o (L_d) domains at equilibrium (beyond 6 μs) as the percentage of all DPPC-Chol (DIPC-Chol) contacts out of all DPPC-lipid (DIPC-lipid) contacts, noted as <%Chol-DPPC cont.>^{eq} (<%Chol-DIPC cont.>^{eq}). To compute the domain overlap describing a random mixture given the same coordinates, we randomly shuffle the chemical identity of lipids in both leaflets prior to calculation, finding Λ_{random}.

Because the membrane becomes substantially undulated at higher Chol concentrations, using the z-axis as the director vector would not be informative as the structural order of lipid tails is correlated with the membrane surface undulation. In measuring both Ψ_6 and P_2 order parameters, we use a plane of best fit for each lipid tail with its six nearest neighbors. Ψ_6 is measured using the DPPC, DIPC, and Chol tails. P_2 is measured using the vector from the GL1 (GL2) to C4A (C4B) beads and the normal vector of this plane of best fit for each lipid. We evaluated the sizes of domains of DPPC and Chol lipid tails by both the number of intra- (n) and inter-leaflet (m) lipid tails in domains.

4.3 Results and Discussion

4.3.1 Spatial and structural equilibration

The impact of Chol concentration on the structure and dynamics associated with liquid phase behavior in lipid bilayers was investigated using a CG ternary lipid mixture observed to achieve macroscopic phase separation in molecular dynamics simulation. Simulations of DPPC, DIPC, and Chol lipids at 0, 3, 7, 13, 22, 30, 42, 53, and 61 mol% Chol, maintaining DPPC and DIPC at equimolar ratios, were performed. Three 11 μs replicate trajectories of each system were sampled representing a total of 3 x 9 x 11 μs = 297 μs of simulation. By evaluation of S_{mix}, Λ, P_2, and Ψ_6, we find systems reach a stable state by 3 μs. We consider $\geq$6 μs equilibrium (Figure 4·1)

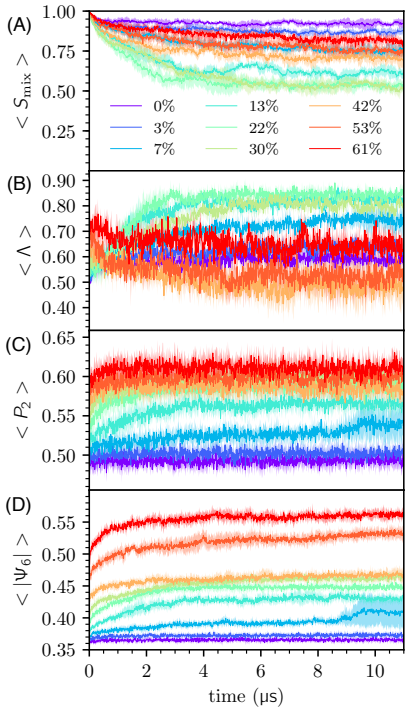

Figure 4·1: Time series averages of (A) mixing entropy, (B) inter-leaflet domain registration, (C) plane-fitted DPPC P_2 order parameter, and (D) absolute value of plane-fitted DPPC bond-orientational order parameter in nine systems of different mol% Chol.

4.3.2 Three regimes of phase behavior

We observe that the membrane becomes demixed at intermediate Chol concentrations (7-42 mol%) and that domains become registered in the phase separated state, which

has previously been confirmed experimentally.[336] Additionally, we observe the well-known phenomenon that the membrane becomes more ordered as Chol concentration increases.

Structures drawn from the end of each simulation show a general trend of increasing local curvature as the concentration of Chol increases, ranging from a flat surface (0-13 mol%), to a standing wave (13-42 mol%), to a rough surface (42-61 mol%) (see Figure 4·2). These changes in morphology appear to be directly related to the partitioning of Chol to regions of concave local curvatures.[348,355] Local Chol concentration is observed to be spatially correlated with anti-registration of lipid domains at high mol% Chol, and this is implied by the high percentage of DPPC-Chol contacts accompanying the anti-registration of lipid domains (Figure 4·3(A), 4·3(B)). the standing wave observed in our simulations spans the unit cell, which is commensurate with the size of the phase separated lipid domains. This was observed in other system sizes at 30 mol% Chol over a range of system sizes in past simulation work.[335] These phase separated domain-spanning undulations have been directly observed in experiment as well,[356] demonstrating that lipid domains each effect their own local curvature on the membrane surface.

Chol is observed to preferentially interact with DPPC. The number of DPPC-Chol and DIPC-Chol contacts, calculated based on Voronoi tessellations of head groups, demonstrate that Chol almost exclusively aggregates with DPPC up to 13 mol% Chol (Figure 4·3(A)). This colocalization of DPPC and Chol supports L_o domain formation, ensuring complete formation of L_o phase at only 13 mol% Chol, where 30% of all DPPC contacts are made with Chol.[172] Near 20, 33, and 55 mol% Chol the ratio of DPPC-Chol contacts to DIPC-Chol contacts agrees well with recent label-free Raman spectroscopy measurements of Chol partitioning in DPPC:DOPC:Chol monolayers,[2] as well as with x-ray experiments by Chen et al.[3] and Bellička et al. at 20 and 24 mol% Chol.[4] The increase of DPPC order parameters as the percentage of DPPC-Chol contacts increase from 0-50% is similar to that observed recently by Wang et al. in MARTINI (see Figure 4·2(D), 4·2(G)).[357] At Chol concentrations surpassing 50 mol% we see that DPPC-Chol contacts exceed the 66% solubility limit of Chol for a bulk membrane.[209–212]

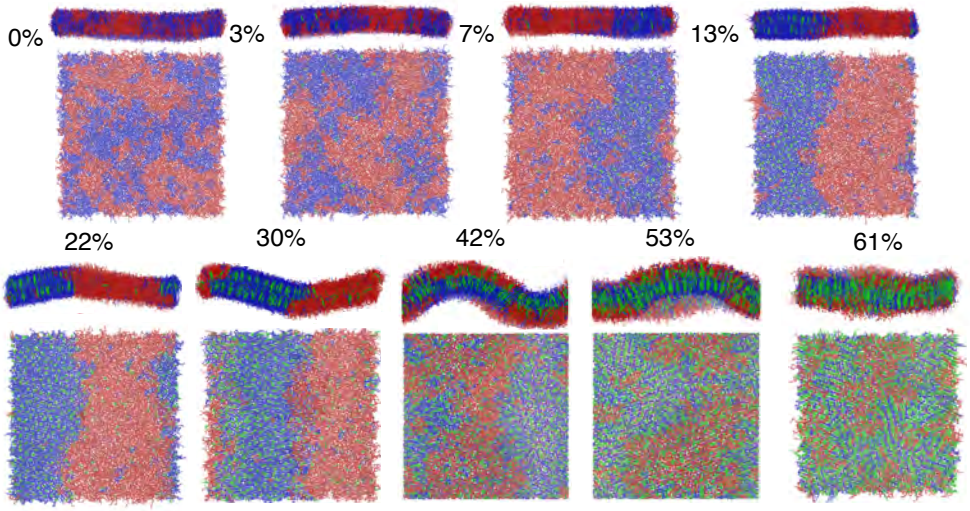

Figure 4·2: Renderings of the top and the side of the final frame of simulation for a trajectory corresponding to each system. DPPC, DIPC, and Chol are rendered blue, red, and green, respectively, using VMD 1.9.4. Bonds are drawn using cg_bonds.tcl from the MARTINI developers. The xy-plane is rotated in some frames to better view the axis of phase separation.

At these high Chol concentrations we observe the formation of anti-registered ordered domains that feature linear aggregates of DPPC and Chol (Figure 4·2). This structure features repeating face-to-back linear aggregates of Chol separated by a single layer of DPPC tails, such that each Chol forms contacts with exactly two other Chol in these domains. This structure is supported by the cholesterol "umbrella model", in which lipids associate with Chol to prevent solvation of Chol head groups by water. The particular lamellar arrangement of lipids and Chol we observe was previously predicted by umbrella model-inspired lattice simulations developed by Huang and Feigenson.[209] In their simulation model an energetic penalty to Chol-Chol contacts effectively modeled the umbrella effect, and at about 66 mol% aggregates of Chol, in which each Chol made contact with exactly two other Chol, forming a maze-like structure which minimizes the number of Chol-Chol contacts. Later, off-lattice simulations by Mouritsen and coworkers also observed these linear Chol aggregates and referred to them as "threads", the term which we adopt to describe these aggregates.[177] FRET experiments by Parker et al. found that there is a minimum in Chol-Chol contacts about 66 mol% Chol within the range of 45-70 mol%, just below concentrations that would form Chol monohydrate crystals in solution.[210] Parker et al. argued these results support the existence of these Chol threads which minimize the cluster size of Chol.

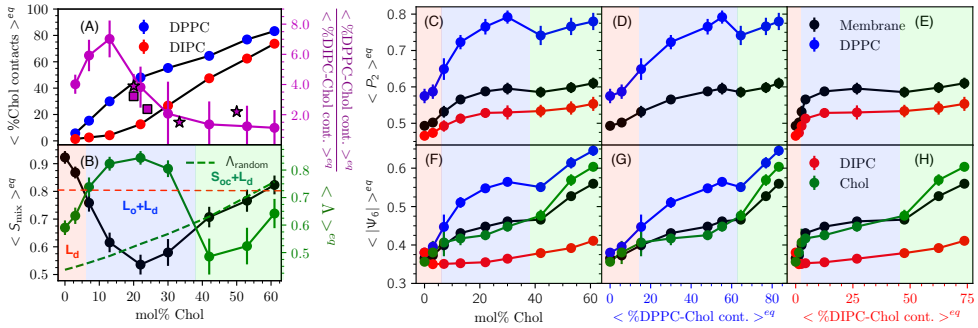

Figure 4·3: (A) Chol-lipid contacts with DPPC and DIPC as % of total lipid-lipid contacts. Stars indicate the DPPC:DOPC:Chol monolayer Raman spectra observations of Donaldson and Aguiar.[2] Squares indicate x-ray inferences by Chen et al.[3] and Bellička et al.[4] (B) Mixing entropy and inter-leaflet domain registration ratio of %Chol-DPPC to %Chol-DIPC contacts. Shading represents the regimes presenting unique phase behavior labeled I (red), II (blue), and III (green). The dashed red line is the mixing entropy at 50% domain miscibility, $S_{mix}^{50\%}$. The dashed green line is the equilibrium average domain registration determined from random permutation of chemical identities in these trajectories. Equilibrium DPPC, DIPC, and Chol order parameters as a function of (C and F) mol% Chol (D and G) %Chol-DPPC contacts and (E and H) %Chol-DIPC contacts. All contacts are between head groups.

These Chol threads are much like our observed structures above 50 mol% Chol, in which we observe $\gtrsim$66% of DPPC contacts to be with Chol (Figure 4·3(A)). We previously performed atomistic simulations to study Chol dimerization structures and found that Chol forms the face-to-back dimers (which we observe here) with high propensity, suggesting Chol threads form not only due to the umbrella effect, but also due to some preference for dimerization.[228,229] Additionally, AFM experiments in ternary mixtures of similar mol% Chol observe the persistence of nanoscopic domains of unknown phase, which may be the domains containing Chol threads we report here.[175,202,226,227]

These highly ordered domains also exhibit bond-orientational order at the domain length scale, similar to the gel phase.[313] As such, we refer this phase as a "cholesterolic gel" (S_{oc})—a lipid gel phase that includes (and is induced by) cholesterol. These observations support the existence of three regimes of phase behavior, denoted (1) regime I, miscible L_d, (2) regime II, domain registered L_d+L_o coexistence, and (3) regime III, domain anti-registered L_d+S_{oc} coexistence. The transition points between these regimes are discussed later.

4.3.3 Structure of regimes of phase behavior

At low (0-7 mol%) Chol concentration the whole membrane is in the L_d phase. This may be surprising, as our simulations are at 295 K and the T_m of pure DPPC is 314.5±1.8 K.[156] However, in the MARTINI model the T_m of DPPC has been determined to be as low as 292.4 K, as determined via the generalized Replica Exchange MD method,[349] and 296 K, as determined via conventional Replica Exchange MD.[303] Additionally, mixtures of DPPC with other lipids are known to both substantially decrease[303] and broaden the corresponding peak in the heat capacity.[217,219,220] For example, in equimolar DPPC:DOPA mixture, T_m decreases to approximately 294.45±0.2 K.[220] Because DIPC has more unsaturated bonds than DOPA, it is possible that mixtures of DPPC with DIPC would exhibit an even lower T_m than mixtures of DPPC with DOPA.

At equilibrium the P_2 and $|\Psi_6|$ order parameters increase up to a "dip" marking the apparent transition between L_o to S_{oc} phases at 42 mol% Chol, where 66% of DPPC contacts are shared with Chol (Figure 4·3(A), 4·3(C), 4·3(F)). The S_{oc} phase becomes yet more ordered with higher mol% Chol. The structure of DIPC is generally insensitive to Chol concentrations and the P_2 of DIPC increases only slightly as the L_o phase is formed by DPPC and Chol (Figure 4·3(E)).

The S_{oc} phase is structurally distinct from the L_o phase due to the unique lamellar structures formed by DPPC and Chol, manifest in the bond-orientational order of DPPC and Chol. The 3, 22, and 52 mol% Chol systems, representative of regimes I, II, and III, are distinct as characterized by the $|\Psi_6^k|$ and Ψ_6^k order parameters (Figure 4·4).

Inspection of Ψ_6^k reveals that the L_d, L_o, and S_{oc} phases are analogous to the liquid, hexatic, and solid phases of 2D systems.[260] In regime I (0-7 mol% Chol) there is no significant orientational order as measured by Ψ_6^k or $|\Psi_6^k|$ over any length scale in the system. In regime II (7-42 mol% Chol) $|\Psi_6^k|$ is ordered and correlated over the Lo domain. In regime III (42-61 mol% Chol) $|\Psi_6^k|$ is ordered and $|\Psi_6^k|$ and Ψ_6^k are correlated over the length scale of all S_{oc} domains (Figures 4·4).

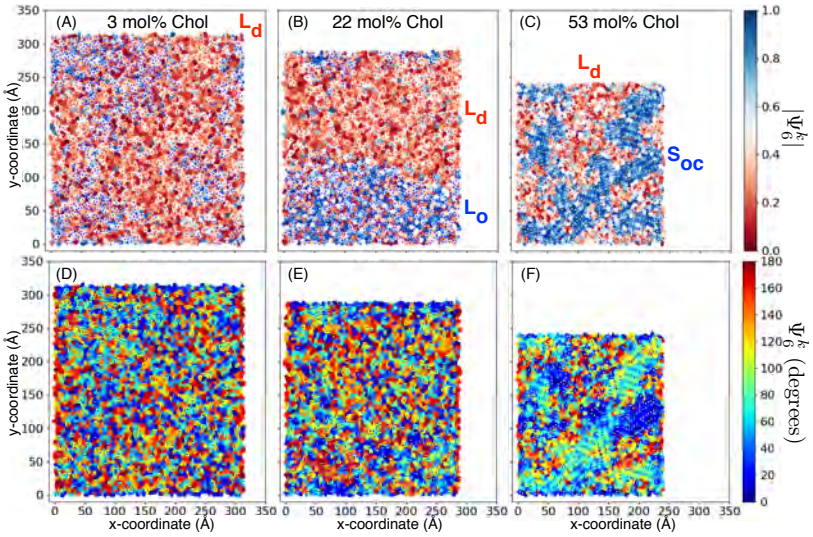

Figure 4·4: Voronoi tessellations of lipid and Chol tails in upper leaflets of simulated membranes at the last frame of each trajectory. DPPC (blue), DIPC (red), and Chol (white) dots represent tails. Voronoi cells are colored according to the absolute and untransformed value of lipid tail bond-orientational order parameters at (A and D) 3 mol% Chol, (B and E) 22 mol% Chol, and (C and F) 52 mol% Chol.

The S_{oc} phase observed in this study is similar to a gel phase. While gel phases showing "hexatic" order have recently been reported in terms of the Ψ_6 order parameters,[179,358] the S_{oc} phase is distinct due to the presence of Chol threads and the effects of Chol threads on the membrane surface that drive domain anti-registration.

Chol, DIPC, and DPPC are evidenced to strongly prefer concave, weakly prefer concave, and weakly prefer convex local curvature on the membrane surface, respectively, as determined via x-ray measurements on monolayers supported by inverted hexagonal phases.[348] Because S_{oc} domains contain Chol in higher concentration, S_{oc} domains may induce concave curvature overall. This would explain the preference of S_{oc} domains for registration with L_d domains in the opposing leaflet, which are more fluid and contain less Chol. This important difference in domain preferences for local curvature may be accounted for by the theoretical model of Schlomovitz and Schick.[340,341] However, our results demonstrate that these quantities are sensitive to the concentration of Chol in the membrane, and particularly in each domain, which has not been considered in these models.

4.3.4 Miscibility transitions between regimes of phase behavior

In undergoing the miscibility transition between these regimes of phase behavior we expect the system to present fluctuations in local lipid compositions with a disperse distribution of domain sizes. To explore the miscibility transitions, we identified transleaflet clusters of DPPC and Chol tails, defining aggregates of n intra- and m inter-leaflet tails at equilibrium (Figure 4·5). We find that the structural order of domains is insensitive to domain size, as previously identified in 30 mol% Chol.[335]

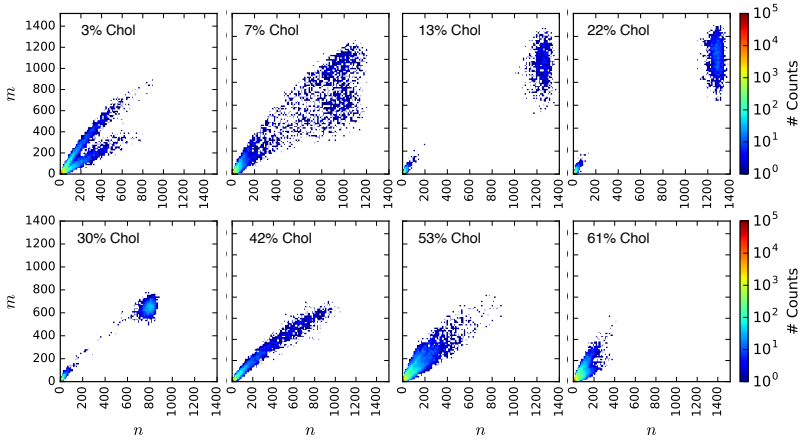

Figure 4·5: Voronoi tessellations of lipid and Chol tails in upper leaflets of simulated membranes at the last frame of each trajectory. DPPC (blue), DIPC (red), and Chol (white) dots represent tails. Voronoi cells are colored according to the absolute and untransformed value of lipid tail bond-orientational order parameters at (A and D) 3 mol% Chol, (B and E) 22 mol% Chol, and (C and F) 52 mol% Chol.

Examination of transleaflet aggregate sizes in regimes I and III show a bifurcation of slopes of $m(n) \approx 2/3$ and $m(n) \approx 1/3$ corresponding to a $\sim$2/3 domain overlap similar to Λ in Figure 4·3(B). A polydispersity in domain sizes is observed at 7 and 42 mol% Chol. The transition from regimes I to II seems to be well-described by the 50% miscibility point, as the 7 mol% Chol system S_{mix} is marginally lower than $S_{mix}^{50\%}$ (Figure 4·4(B)). Additionally, order parameters at 7 mol% Chol show larger fluctuations at equilibrium than other system compositions (Figure 4·1). The transition observed at 42 mol% Chol is apparently not well-described by $S_{mix}^{50\%}$. However, the transition of domain overlap, Λ, to below Λ_{random} indicates the onset of anti-registration at 42 mol% Chol (Figure 3(B)), and there is a clear signature of this transition in P_2 and $|\Psi_6|$(Figure 4·3(C-H)). It may be possible to identify the transition to regime III by measurement of domain overlap with a method analogous to our computation of Λ spectroscopically using leaet-selective deuteration.[346] The transition from nanoscopic

domain coexistence to macroscopic phase separation near 7 and vice-versa at 42 mol% Chol approximately fits the DPPC:DOPC:Chol phase diagrams of Veatch et al. and Davis et al., which measure these transitions to occur at approximately 10 and 45 mol% Chol,[194] and 10 and 35 mol% Chol, respectively.[205]

4.4 Conclusion

We have performed a detailed investigation of Chol concentration on phase separation in bilayers formed of ternary lipid mixtures using molecular dynamics simulation. We observed three regimes of phase behavior, denoted I) miscible L_d phase, II) macroscopically phase separated L_d+L_o coexistence featuring registered domains, and III) microscopically phase separated anti-registered domains of L_d coexistent with the newly identified liquid cholesterolic gel (S_{oc}) phase. These structures were validated by comparison with experimental determinations of Chol partitioning in lipid domains,[2–4] theoretical expectations of Chol-lipid complex structures at high mol% Chol invoking the umbrella model[209] supported by FRET experiments,[210] and the miscibility phase diagrams of DPPC:DIPC:Chol mixtures.[194,205] We demonstrate the structural difference between these three regimes via order parameters characterizing mixing, domain registration, structural order along the bilayer normal, structural order within the membrane plane, and transleaflet domain sizes. We find regimes I, II and III to manifest distinct differences in bond-orientational order. The S_{oc} phase is found to exhibit 2D bond-orientational order over the length scale of the lipid domains, characterized by face-to-back threads of Chol and DPPC.

There may be biological implications of the S_{oc} phase for determination of protein structure and function, as proteins can preferentially partition to particular lipid domains. The complex phase behavior induced by cholesterol effects the structure, function, and processing of proteins in Alzheimer's and other diseases, and will therefore continue to be relevant to our understanding of these disease mechanisms. The S_{oc} phase may need to be considered in addition to the L_d and L_o phases when considering protein structures in such disease pathways.

These collected observations substantially enhance our understanding of the role of Chol in complex phase behavior in ternary lipid mixtures and provide a framework for exploring structure and dynamics of domain formation in future computational, theoretical, and experimental investigations.

Chapter 5

Impact of Cholesterol Concentration and Lipid Phase on Structure and Fluctuation of C99

5.1 Introduction

The Sanders group has observed that cholesterol modulates chemical shifts in C99 and proposed that a specific C99-Chol complex is formed using the $G_{29}xxxG_{33}xxxG_{37}$ glycine zipper and a hydrogen bond with the ($K_{16}LVFFAED_{23}$) juxta-membrane domain.[5,98,104] Song et al. characterized the equilibrium constant of C99-Chol association, $K_d^{C99-Chol}$, in POPC:POPG lipid vesicles as 2.7 ± 0.3 mol% (-2.1 kcal/mol) via fitting changes in chemical shift as a function of protein and cholesterol concentration to a phenomenological kinetic model.[53] However, equilibrium constant is weaker than typical protein backbone-water hydrogen bonds (H-bonds).[246]

The TMD of C99 (G_{29}AIIGLMVGGVVIATVIVITLVMLKKK$_{55}$) contains several sequence motifs known to stabilize canonical "GAS_{right}" homodimers, including $G_{29}xxxG_{33}xxxG_{37}$ and $G_{38}xxxA_{42}$.[106,359,360] Sanders has proposed that the glycine zipper provides a "groove" that supports contacts between the C99 TMD and the smooth α-face of Chol.[104] All-atom MD simulations of the C99 TMD in DMPC:Chol bilayers, employing initial conditions in which the Chol α-face is in contact with the $G_{29}xxxG_{33}$ face of C99 (Figure 5·1.A-C), estimated the C99-Chol binding energy to be -2.6 ± 0.4 kcal/mol.[361] A subsequent simulation study observed the pKa of E22 and E23 of the C99 JM domain, having pKa values of 7.4 ± 0.1 and 6.5 ± 0.1, must be protonated to stabilize the JM helix and Chol interactions.[102] The JM domain helix can be destabilized when both E22 and D23 are protonated (neutralized), at pH 7. As such, the structure and function of the JM helix is different at the cytosolic pH of 7 experienced in plasma membranes and the luminal pH of 4.5 to 6.5 in endosomal membranes.[362] E22 and D23 are also sites for Familial AD (FAD) mutations, including the Dutch

(E22Q)[127] and Iowa (D23N)[131] mutants.

The potential interplay of C99 and cholesterol are often discussed in terms of a stable C99-Chol complex.[363] The concept of a bound C99-Chol complex is surprising, as there is no precedent for cholesterol binding to other single-pass transmembrane proteins. Protein-cholesterol binding interfaces have been defined for multi-pass proteins such as G-coupled protein receptors (GPCRs) and ion channels.[235,364–374] These transmembrane interfaces have often been characterized in terms of Cholesterol Recognition/interaction Amino acid Consensus (CRAC) sequences.[249,375] CRAC domain sequences are (L/V)-X_{1-5}-Y-X_{1-5}-(K/R), in which X_{1-5} are any apolar amino acid. CARC ("inverse" CRAC) domains are (K/R)-X_{1-5}-(Y/F)-X_{1-5}-(L/V).[376] Within these CRAC or CARC domains, the aromatic residues are conjectured to support Chol-protein π-stacking interactions with the Chol-α face assisted by van der Waals contacts with Leu or Val. These domains can also support H-bonding with Chol at the lipid-water interface with Arg or Lys. C99 contains one CARC sequence in the JM domain, K_{16}LVFFAEDV_{24}. Within this domain, the pH-switching residues E22 and D23 are present.

Barrett et al. studied C99 in DMPC:DHPC using ^{1}H-^{15}N NMR and observed chemical shifts that strongly ($F_{20}, E_{22}, G_{29}, I_{32}, G_{33}, V_{39}$) or moderately ($D_{23}, N_{27}, L_{34}$M VG$G_{38}$) respond to changes in Chol concentration.[5] It was suggested that these residues may constitute the binding interface (Figure 5·1.C). However, the orientation of these residues around the helical TMD shows no particular face of C99 along which Chol would interact (Figure 5·1.D). Taken together, these observations suggest that the C99-Chol complex is only moderately stable and may be less specific than previously proposed.

MD simulations have been used to explore protein-Chol binding interfaces in GPCRs employing the MARTINI lipid and protein model to explore possible protein-Chol complexes.[235,365,366,368–372] These coarse-grained simulations have led to the identification of contacts formed between multiple transmembrane helices. Putative protein-Chol binding complexes are mapped to all-atom models to elucidate their structure and specific stabilizing interactions. Given the lack of significant structural pockets, this approach cannot be used to propose binding sites for Chol to single pass transmembrane proteins such as C99. In addition, coarse-grained models lack detailed H-bonding and π-stacking interactions necessary to support stable C99-Chol complexes,[6] making them unsuitable for the exploration of Chol-protein binding.

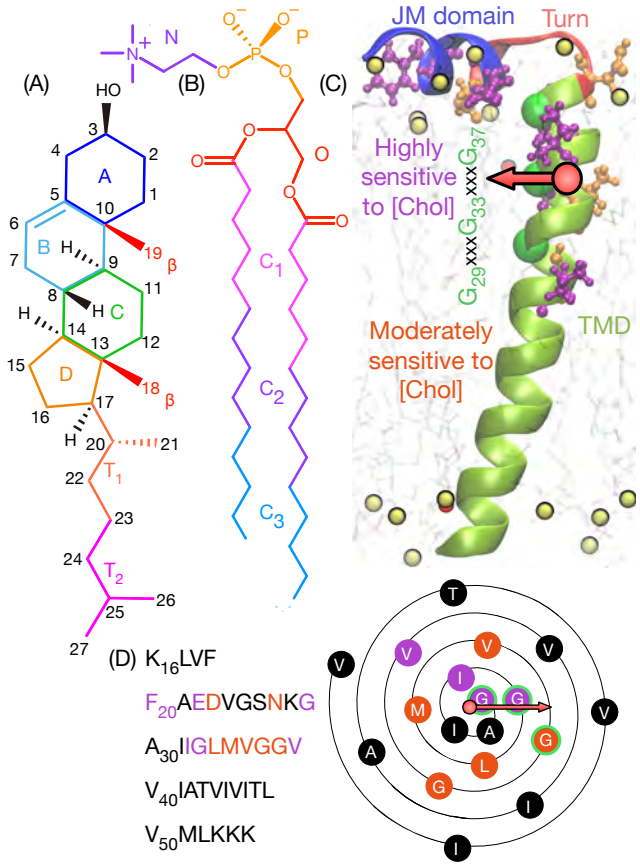

Figure 5·1: (A) Molecular structure of Chol, coloring the O, β, A-D rings, T_{1-2} groups used to average C99-Chol contacts. (B) Structure of DMPC, coloring the N, P, and C_{1-3} groups used to average C99-DMPC contacts. (C) $C99_{16-55}$ of PDB:2LOH in DMPC:Chol 8:2 membrane. JM domain, turn, and TMD labeled in blue, red, and green-yellow, respectively. Residues highly (moderately) sensitive to Chol concentration in purple (orange).[5] GxxxGxxxG motif Cα in green. DMPC (Chol) phosphorous (oxygen) in yellow (red) and lipid tails (transparent) within 10 shown for reference. $C99_{16-55}$ sequence displayed with residue coloring. (D) Wenxiang diagram of residues 29 to 46 of the transmembrane helix.

The minimal subsequence $C99_{16-55}$, (K_{16}LVFFAEDVGSNKGAIIGLMVGGVVIA TVIV- ITLVMLKKK$_{55}$), appears to be required to capture essential interactions between C99 and cholesterol. This congener contains the ubiquitous VGSN turn sequence, the central hydrophobic cluster KLVFFAED,[15,377] and the C99 TMD, including the $K_{53}K_{54}K_{55}$ lysine anchor.[67,107] For C99 in plasma membranes and micelles, experiment and simulation suggest that KLVFFAED will form a JM helix, that VGSNK forms a turn, and GAIIGLMVGGVVIATVIVITLVMLKKK forms the

α-helical C99 TMD.[5,6,67,98,104,108]

Here, we employ unbiased MD simulations, that make no prior assumption of the C99-Chol encounter complex, in order to characterize the nature of the C99-Chol interaction in DMPC bilayers containing 0, 5, 10, and 20 mol% Chol. Four forms of C99 were studied including (1) wildtype $C99_{16-55}$ neutral E22, D23 or (2) charged E22, D23, and (3) the Dutch (E22Q)[127] with mutant neutral D23 and Q23, and (4) Iowa (D23N)[131] mutant with neutral E22 and N23. We performed 70 unbiased, 1-μs all-atom simulations of $C99_{16-55}$.

Enhancements to cholesterol concentration induced the L_o phase, changing the structure of C99. We characterized the structure of C99 by TMD tilt, helical propensity, orientation of the JM domain, and height of the JM domain above the membrane surface. We also observed that the E22Q mutant, D23N mutant, and charge state of E22 and D23 in the L_o phase also change the structure of C99. C99-cholesterol residence lifetimes were found to be power-law distributed with constants k in the range of 1.21 to 1.43, suggesting heterogeneity in the stability of C99-Chol complexes. Of these, long-lived C99-Chol complexes were found to be supported by hydrogen bonds of K16 and K28 with the Chol hydroxyl group in the upper leaflet (exo-facing in plasma membrane), and K53-K55 with the Chol hydroxyl group in the lower leaflet (cyto-facing in plasma membrane). Within the upper leaflet, it was found that the conformation of the JM domain creates unique interfaces for C99-Chol complexes whose potential of mean force are within 1 kcal/mol of the $K_d^{C99-Chol}$ determined by Song et al.[53] We conclude that monomeric C99 does not bind Chol through the formation of a specific, stable heterodimer. We find that multiple, specific C99-Chol complexes can form depdendent on the conformational state of the C99 JM domain and lipid phase.

5.2 Methodology

Molecular Dynamics Simulation

The 40-residue $C99_{16-55}$ congener sequence was used to model C99. The CHARMM36 force field[273,274] was employed to describe the system, using ACE N-terminal and CT3 C-terminal capping groups. C99 was initiated from a configuration based on PDB:2LOH,[378] in which the JM domain is structured, and inserted into the membrane obtained from past simulation of wildtype C99 in DMPC:Chol 8:2 simulations.[102]

Cholesterol was laterally distributed at random in the bilayer such that there was no C99-Chol dimer in the initial state. This is different from past work exploring the C99-Chol complex, in which the initial state was a preformed C99-Chol complex at the GxxxG interface.[102,361] Lipid bilayers, each encapsulating the transmembrane domain of C99, were prepared in CHARMM using the CHARMM-GUI system building protocol.[278,379–382]

The bilayer leaflets were constructed with an asymmetric number of lipids in order to support the insertion of the JM domain in the upper leaflet of the lipid bilayer. For 0, 5, 10, and 20 mol% systems, 69, 66, 62, and 55 DMPC were used in the upper leaflet and 73, 69, 65, and 58 DMPC were used in the lower leaflet. For 5, 10, and 20 mol% systems, 3, 7, 14 Chol were used in the upper leaflet and 4, 8, and 15 Chol were used in the lower leaflet. Approximately 46 waters per lipid and 17 Na^+ and Cl^- ions (with additional counter-ions depending on the system) were used to solvate each lipid bilayer. Four different C99 proteins were simulated, including (1) at an effectively acidic pH, in which E22 and D23 were neutral (E22,D23[0]),[102] (2) at neutral pH (E22,D23[-]), as well as the (3) Dutch (E22Q[0]) and (4) Iowa (D23N[0]) FAD mutants at acidic pH. These acidic and neutral pH protonation states are representative of the endosomal and plasma membrane environments, respectively. Ten replicates of each of these proteins were prepared with unique, randomized lateral distributions of DMPC and Chol. Each system was minimized and then equilibrated using a processive release of restraints and associated increase from 1- to 2-fs integration time step as suggested by Wu et al.[381]

All molecular dynamics simulations were performed using 25 2.4 GHz Intel Xeon E5-2680v4 CPUs and a P100 GPU using GROMACS 2018.3[277] at mixed precision to achieve a 86 ns/day rate of sampling for these ∼35,900-atom simulations. The leap-frog integrator was used with a 2-fs time step in combination with hydrogen bond constraints via the SETTLE method.[383] Neighbor lists were updated every 20 steps using the buffered Verlet neighbor scheme. Short-range interactions employed a 1.2 nm distance cutoff with a force switching function applied from 1.0 to 1.2 nm for Lennard-Jones and from 0 to 1.2 nm for electrostatic interactions. Long-range interactions were handled using Particle Mesh Ewald[384] with a 0.12 nm grid spacing and 4th order grid interpolation. A Nosé-Hoover thermostat[385] with 1 thermostatting chain and a time constant of 1 ps was used to control temperature to 310 K, separating C99, the lipid bilayer, and the solvent to three separate thermostat groups. The

Parrinello-Rahman barostat[386] was used with the z-axis decoupled from the xy-plane employing a 5 ps time constant, a reference pressure of 1 bar, and a compressibility of 4.5x10^{-5} bar^{-1}. Each system was run for 1 μs of MD, summing to 70 μs of sampling. Coordinates were saved every 100 ps. All analyses employed this frame-resolution, including 100,000 frames in the analysis of each system.

Analysis Methods

Various structural order parameters providing insight into the protein conformational ensemble were employed to characterize essential changes to C99 structure in these different conditions. To describe insertion of the JM domain to (or evacuation from) the membrane surface, we evaluated the difference of the z-axial positions of K16 Cα atoms from the mean z-axial positions of the phosphorous of DMPC within the upper leaflet of each frame. The TMD tilt (polar) angle, θ, JM domain azimuthal angle in reference to the GxxxG face ($G_{29}AIIG_{33}LMVG_{37}$), ϕ. The helicity of C99 was characterized by the identification of amide hydrogen bonds (H-bonds) in the backbone.

To define the xy-plane distribution of upper-leaflet Chol or DMPC complexed with C99 relative to the GxxxG face, we rotated the coordinates of the system such that the xy-plane projection of the GxxxG face vector points along the positive x-axis, obtaining the position of solvating Chol or DMPC in these transformed x' and y' coordinates. To determine contacts between C99 and Chol or DMPC, we used a 5 distance cut-off between heavy (non-hydrogen) atoms to define whether a contact was formed. To more easily represent C99-Chol contacts, contacts of each heavy atom on Chol (of 28) with each protein residue (of 40) were averaged over geometrically-representative subunits of the Chol molecule, simplifying from 28 Chol contacts to 8. Subunits of Chol were assigned as O (O3) the oxygen head group, β (C18, C19) defining β-face methyl groups, the sterol rings A (C3, C2, C4, C1, C5, C6), B (C6, C10, C7, C9, C8), C (C9, C8, C11, C14, C12, C13), D (C14, C13, C15, C16, C17), and the upper and lower segments of the carbon tail, T_1 (C20, C21, C22, C23) and T_2 (C24, C25, C26, C27) (Figure 5·1.A). Similarly, to easily represent C99-DMPC contacts, the 46 heavy atoms of DMPC are averaged over the geometrically-representative subunits of DMPC, simplified from 46 to 5 contacts. Subunits of DMPC were assigned as N (C13, C14, C15, N, C12, C11), P (O12, O13, O14, P, O11, C1), C1 (C22, C23, C24, C25, C26, C32, C33, C34, C35, C36), C2 (C27, C28, C29,

C210, C37, C38, C39, C310), and C3 (C211, C212, C213, C214, C311, C312, C313, C314) (Figure 5·1.B).

We tracked the "residence time" over which each Chol or DMPC remained in contact with C99. A 25-ns cutoff in residence time was used to distinguish complexed and transient Chol or DMPC upon inspection of residence time probability distributions. The number of Chol or DMPC simultaneously solvating C99 was determined by counting the number of intersecting residence times between solvating Chol or DMPC (with residence times >25-ns) per frame in each simulation. This was done by first determining the number of n-mers of the highest order, progressively evaluating lower order n-mers down to a dimer, and removing frames found to intersect with other frames when determining the number of each n-mer present in the trajectory. This ensured that a given frame of a solvating Chol or DMPC could not be counted as part of both a higher- and lower-order n-mer. This analysis was performed in the upper and lower leaflets to quantify the number of simultaneously populated solvation sites of the C99 congener.

The angular distribution of the Chol mass density around the GxxxG face supported the definition of five unique C99-Chol interfaces in the upper leaflet (see Results). We determined the relative population and C99-Chol contacts for these five interfaces, defined based on the angular position around the GxxxG face vector. The interfaces labeled from 1 to 5 were assigned for Chol centers of mass at positions between 290-45°, 45-115°, 115-190°, 190-220°, and 220-290° relative to the GxxxG face vector. The relative orientation of these interfaces corresponds to the relative positioning of residues that exhibited strong or moderate changes in chemical shift as measured in past NMR studies of C99 (Figure 5·1.C) in DHPC:DMPC:Chol bicelles.[5]

We measured the hydrogen bonds formed for solvating C99 or DMPC involving Lys 16, 28, 53, 54, and 55. From Lys, the amide nitrogen, N, amido nitrogen, NZ, and, for Lys 55, the capping nitrogen, NT, serve as donors and the carbonyl O3 serves as an acceptor. From Chol, the hydroxyl group, H3 and O3, serves as donor and acceptor. From DMPC there are three groups of acceptors. From the phosphate there are O11, O12, O13, and O14. From the ester groups on the lipid tails there are O21 and O22, and O31 and O32. A hydrogen bond was defined if the H-O distance is under 2.5 Å and if the N-H-O angle is larger than 150°. The Lys-phosphate hydrogen bonds measured here are more appropriately described as a salt bridge due to its ionic character, and we refer to it as such in what follows.

5.3 Results and Discussion

All-atom MD simulations of $C99_{16-55}$ employing neutral, protonated E22 and D23 corresponding to pH $\leq$ 6.5[102] were performed at 0, 5, 10, and 20 mol% cholesterol (Chol) in DMPC lipid bilayers mimicking experiments of Song et al.[53] At 20 mol% Chol, simulations of $C99_{16-55}$ at acidic pH (C99[E22,D23[0]]) and neutral pH (C99[E22,D23[-]]) were performed, along with simulations of the Dutch (C99[E22Q[0]]) and Iowa (C99[D23N[0]]) FAD mutants at acidic pH. These acidic and neutral protonation states mimic the endosomal and plasma membrane environments in which C99 is processed by γ-secretase to form amyloid beta (Aβ).[80,362,387,388] Analysis of 10 1-μs replicates of each system was used to characterize the conformational ensembles of C99 and interfaces of long-lived C99-Chol complexes.

5.3.1 C99 conformational ensemble

Orientation of C99 domains depends on cholesterol concentration

At 0, 5, 10 and 20 mol% Chol, the bilayer is characterized as a miscible mixture of DMPC and Chol. In order to characterize the effect of varying Chol concentration and lipid ordering, we computed the C99 tilt angle (θ) distribution, relative orientation of the JM domain to the GxxxG face in the xy-plane (ϕ), the insertion depth of the JM domains to the membrane surface, and the helicity of C99 residues.

When the concentration of Chol is increased in saturated lipid bilayers the L_o phase formed.[389] This manifests a commonly observed z-axial thickening and xy-plane condensation and ordering of lipids in the lipid bilayer that is expected to cause the C99 tilt angle (θ) to decrease. The C-H NMR order parameter was used to report on the enhancement in lipid tail ordering characteristic of the L_o phase, which we observe to be substantially enhanced by addition of Chol. What was not anticipated, was the change in the xy-plane orientation of the JM domain relative to the GxxxG face in response to this ordering of the bilayer (ϕ). Analysis of the E22,D23[0] systems at 0, 5, and 10 mol% Chol exhibit θ distributions centered near 45° which shift to 25 ° in 20 mol% Chol, indicating a major change in TMD conformation in the L_o phase.

In ϕ, multiple states which do not interconvert are observed. Typically, the JM domain was positioned at ϕ=60° or 340° counterclockwise from the GxxxG face are observed from the N-terminus, the latter becoming more populated at 20 mol% Chol (Figure 5·2.A-D). However, the conformational distribution at 20 mol% Chol was

found to be sensitive to both charge state and sequence of residues 22 and 23 (Figure 5·2.D-G). For E22,D23[-], θ fluctuates about 20° and ϕ is random. E22Q[0] exhibits three clear states in ϕ, with the JM domain sitting at about ϕ=60° and occasionally at ϕ=280°, and fluctuates about θ=35°. D23N exhibits slightly different behavior, as the JM domain populates three states characterized by (θ,ϕ)=(40,20°), (25,60°), and (25,140°). These observed differences in JM domain orientation (ϕ) and TMD tilt angles (θ) appear to be signatures of where and how Chol interacts with C99. The observation that the conformational ensembles of the JM domain and TMD tilt depend sensitively on the chemical state suggest that these changes in charge state and sequence could impact C99 homodimerization and C99-γ-secretase binding.

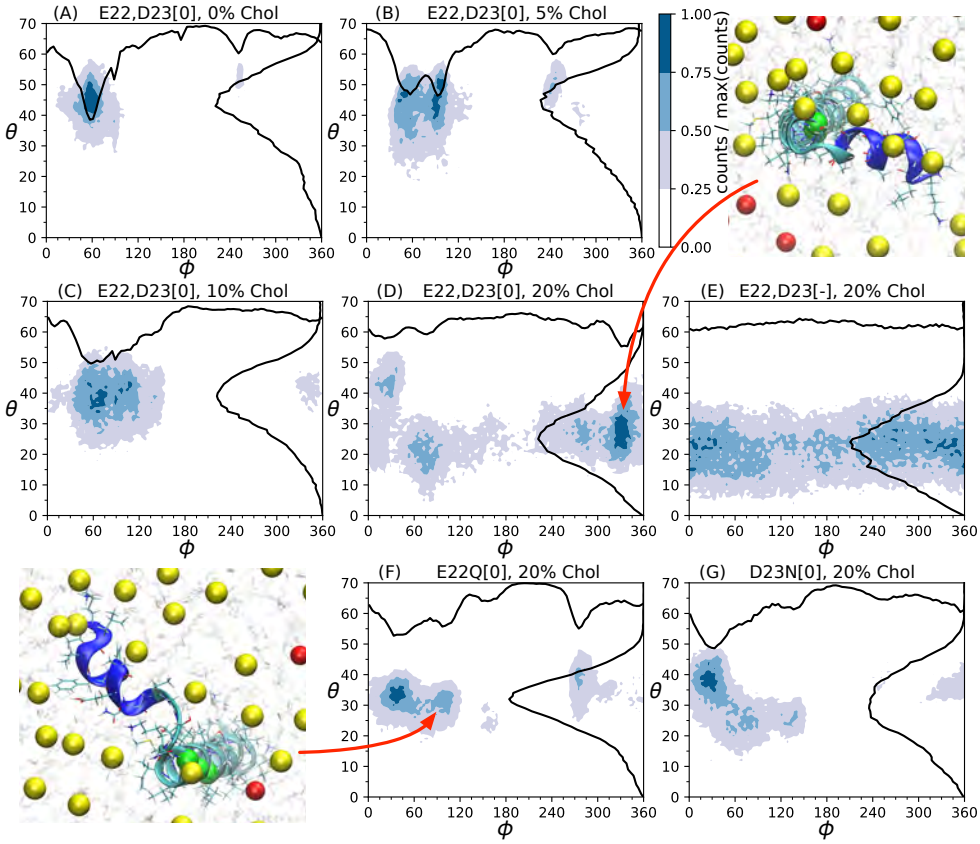

Figure 5·2: Scaled observations of C99 E22,D23N[0] TMD tilt angle (θ) and orientation of JM domain relative xy-plane orientation to the GxxxG face (ϕ) at (A) 0, (B) 5, (C), 10, and (D) 20 mol% Chol. (E) E22,D23N[-], (F) E22Q[0], and (G) D23N[0] distributions at 20 mol% Chol. Visualizations of the phosphorous and oxygen of DMPC and Chol (yellow and red) and C99 from above the xy-plane, coloring $G_{29,33,37}$ green and the JM domain blue.

Insertion of the JM domain depends on sequence and charge state

The insertion depth of K16 serves as a measure of JM domain orientation relative to the bilayer surface. For C99 E22,D23[0] we observe that insertion of the JM domain increases with increasing mol% Chol (Figure 5·3.A). For E22,D23[-] the JM domain is observed to rarely insert in the membrane surface (Figure 5·3.B). It has been observed that insertion of the JM domain is necessary to complete the putative Chol binding site described by Sanders and coworkers, which involves hydrogen bonding of the JM domain to Chol O3.[102] In the FAD mutants, E22Q and D23N, insertion of the JM domain is observed to be enhanced. Notably, the JM domain of the E22Q[0] mutant is observed to be consistently inserted throughout the simulations.

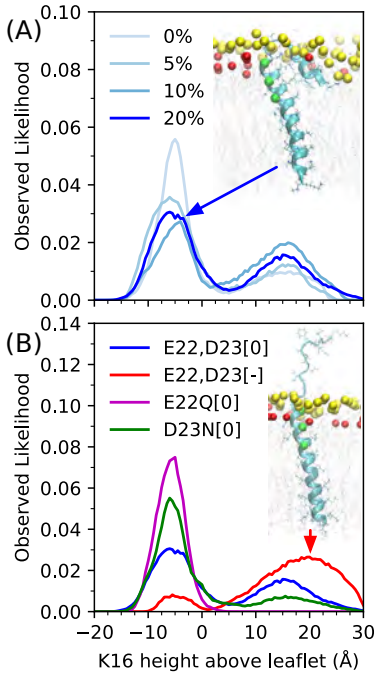

Figure 5·3: Probability densities of K16 height above mean DMPC phosphorous positions used to define the bilayer-solvent interface in upper leaflet (A) for E22,D23N[0] at varying mol% Chol and (B) at 20 mol% Chol. Insets depict phosphorous and oxygen of DMPC and Chol (yellow and red) and color $G_{29,33,37}$ green.

JM domain structure depends on pH

The presence of Chol in the membrane appears to shorten the α-helix of the C99 TMD of E22,D23[0] as the tilt angle of the TMD decreases (Figure 5·4.A). The mea-

sured distribution is consistent with that observed for the full C99 sequence.[67] For E22Q[0] and D23N[0] we see similar helical propensities at 20 mol% Chol. However, in E22,D23[-] the JM domain is observed to be unstructured (Figure 5·4.B). As observed previously, the charge state of E22 and D23 at neutral pH destabilizes the JM domain, leading to extension of the unstructured JM domain into solvent. This pH switch[102] supports a mechanism of pH-dependent insertion and evacuation of the JM domain in wildtype C99. However, this facility seems lost in the E22Q (Dutch) and D23N (Iowa) FAD mutants.

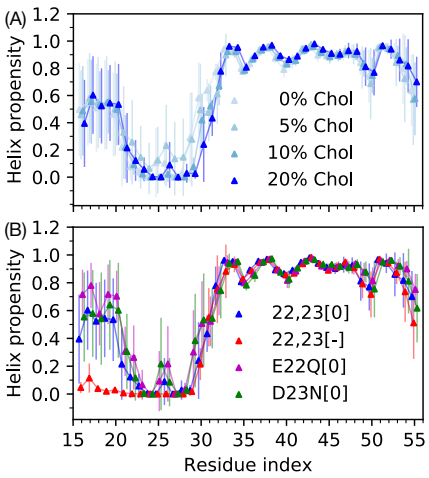

Figure 5·4: α-helix propensity defined by likelihood of any backbone H-bond between each ith and i$\pm$3, i$\pm$4, or i$\pm$5 residues at (A) for E22,D23N[0] and (B) at 20 mol% Chol averaged over replicate trajectories with corresponding standard deviations.

5.3.2 C99 Solvation by Cholesterol and DMPC

Residence times suggest C99 solvation, but not binding

The conjecture that cholesterol modulates the amyloid pathway by forming stable and specific complexes with C99 suggest that we should observe a relatively long-lived C99-cholesterol complex.[104] Within an ensemble of C99-Chol interactions, it should be possible to distinguish "bound" Chol from "unbound" Chol, the latter only forming transient contacts with lifetimes similar to those of other C99-lipid interactions, and that persist for lifetimes in excess of other Chol-lipid interactions (roughly $\sim$0.35 ns on average.)[228] To do this we observed the residence time for each observed C99-Chol

and C99-DMPC contact pair, tracked for each 100-ps time frame, to identify any Chol or DMPC initially in contact with C99 that maintained any contact with C99. This analysis was performed for all C99-Chol and C99-DMPC contact pairs observed in each system. It was found that the average C99-Chol and C99-DMPC lifetime is approximately 1-ns, longer than that of lipid-lipid interactions. The log-log likelihood distributions of C99-Chol and C99-DMPC residence are well described by a power law (Figure 5·5 and S2). We find that the power law exponents, k, are similar for Chol and DMPC, and are between 1.25 to 1.43. This suggests that the C99-Chol interaction observed in simulation and experiment is heterogeneous without a characteristic time or energy scale for binding. For this reason, we refer to Chol and DMPC that persist in contact with C99 for over 25-ns as solvating as opposed to bound.

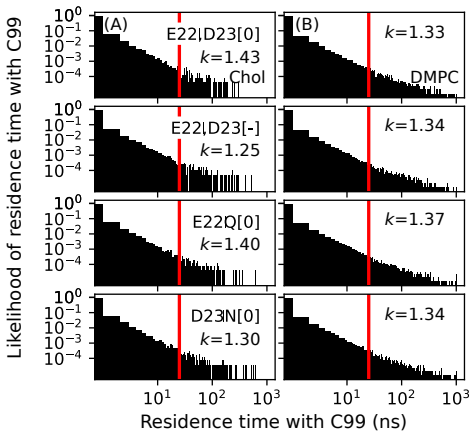

Figure 5·5: C99-Chol dimer residence times observed for all C99-Chol contact pairs at 20 mol% Chol. Red line indicates the 25-ns cutoff used to distinguish transient and complexed C99-Chol pairs. Inset notes power law exponents for C99-Chol residence times.

C99-cholesterol aggregate likelihood distributions

Our results suggest Chol does not form stable and specific bound complexes with C99. To explore the nature of longer-lived associations having residence times >25-ns we address the following questions. How many Chol can concurrently solvate C99? Do C99-Chol complexes in one leaflet impact formation of C99-Chol complexes in the opposite leaflet?

At 20 mol% we observe that Chol in the upper leaflet dimerizes with C99 between 20

to 40% of the time. Higher order aggregates form with varying probability depending on the state of residues 22 and 23 (Figure 5·6.A). In C99 D23N[0], the C99-Chol dimer is as likely as Chol-free C99. In addition, the rare tetramer forms, suggesting that the conformational ensemble of the JM domain in D23N provides more unique and stable interfaces on C99 for solvation by Chol. In the lower leaflet, we see that E22,D23[0], E22,D23[-], and E22Q[0] exhibit similar C99-Chol aggregate likelihoods (Figure 5·6.B). Here, too, D23N[0] exhibits enhanced C99-Chol aggregate likelihoods and sizes. By examining the solvating Chol oligomer distribution without discrimination between the upper and lower leaflet, compared with the joint probability distribution implied if distributions of the upper and lower leaflet are uncorrelated, we find that the oligomer distributions in the upper and lower leaflets are uncorrelated (Figure 5·6.C). These observations imply that C99-Chol complexes are dependent on the conformational ensemble of C99, which is affected by the state of residues 22 and 23 and the formation of the L_o phase at sufficient concentration of Chol.

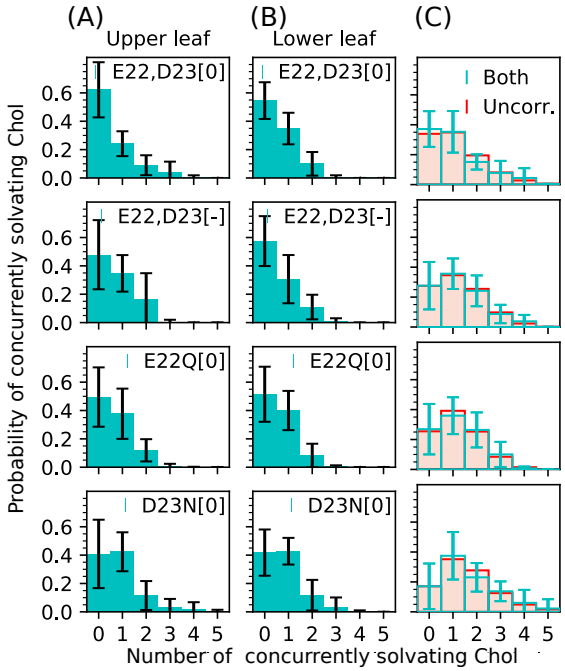

Figure 5·6: Observed probability densities of bound C99-Chol complexes for C99 at 20 mol% Chol in the (A) upper, (B) lower, and (C) both leaflets (cyan) and expectation for both leaflets assuming upper and lower leaflet distributions are uncorrelated (red). Averages and standard deviations are computed over 10 replicate trajectories.

Cholesterol distribution about C99 TMD assumes multiple complex interfaces

As the JM domain assumes various orientations relative to the GxxxG face dependent on the charge state or sequence of C99 (see Figure 5·2), the solvation interfaces of C99-Chol in the upper leaflet are expected to display varying likelihoods and solvation motifs.

In the $C99_{16-55}$ congener, which lacks the C-terminal JM helix, the lower leaflet has no JM domain to obstruct Chol interactions with C99.[67] We characterized the xy-plane mass density of upper leaflet Chol about the C99 TMD with the director oriented outward from the GxxxG face (see Figure 5·7). This GxxxG face has previously been hypothesized to serve as a specific Chol binding site and serves as a primary binding interface for the C99 homodimer. The GxxxG face was defined in terms of a vector in the xy-plane fit through the center of geometry of $IIG_{33}LM$ and the Cα of G33. We aligned the GxxxG face vector along the positive x-axis (now described using transformed coordinates x' and y') and identified five unique faces of C99 that support C99-Chol solvation for varying chemical states of E22 and D23 at 20 mol% Chol (Figure 5·7). These five interfaces (labeled from 1 to 5) correspond to polar angles 290-45°, 45-115°, 115-190°, 190-220°, and 220-290°, respectively, relative to the GxxxG face vector (0°). The potential of mean force (PMF) of the masses of solvating Chol at these interfaces is between 2.5 and 3 kcal/mol, within 1 kcal/mol of of the $K_d^{C99-Chol}$ determined by Song et al.,[53] suggesting that these solvating Chol are a reasonable representation of the bound cholesterol proposed by Sanders and coworkers.

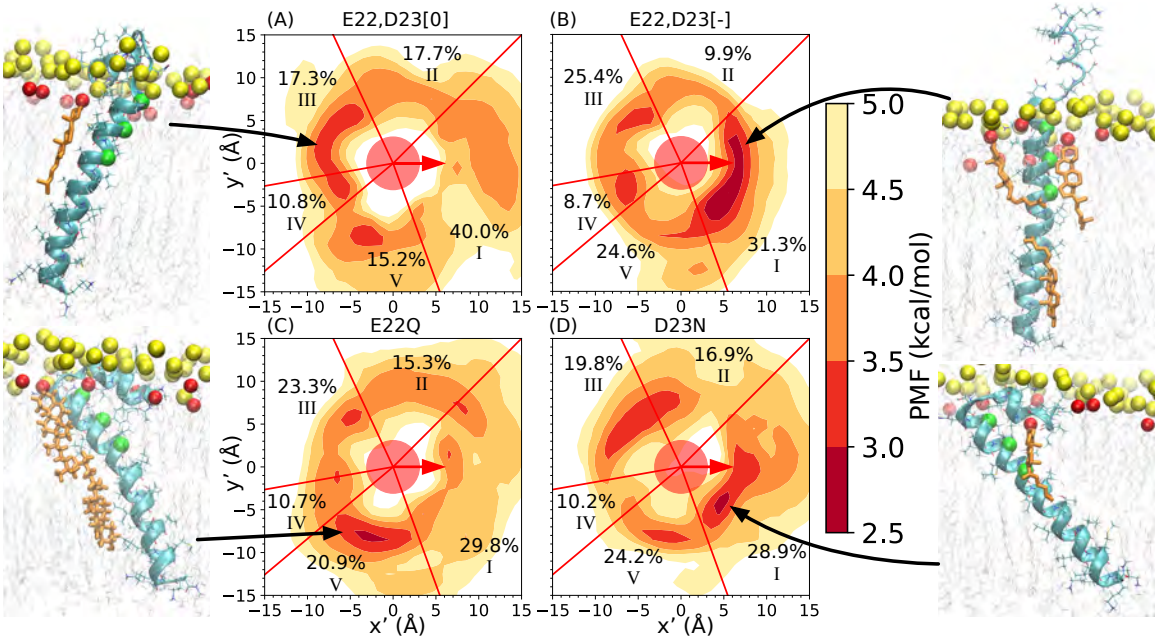

Figure 5·7: Potential of mean force ($-k_{\mathrm{B}}T \ln p(\mathrm{x}', \mathrm{y}')$) about the GxxxG director vector (red) of the C99 TMD (circle). Five angular bins defining interfaces for upper leaflet TMD-Chol solvation demarcated by red lines. Insets display relative population of Chol at each of the five interfaces. Visualizations of C99-Chol complexes demonstrate representative configurations, depicting Chol (orange), $G_{29,33,37}$ (green), and DMPC and Chol phosphorous (yellow) and oxygen (red).

C99-Chol complex motifs depend on juxtamembrane charge state and sequence

C99-Chol contacts formed in the upper leaflet of each solvation interface around the GxxxG face were measured using a 5 heavy atom distance contact criterion. Groups of averaged heavy atom contact pairs on Chol were used to define sites of interaction with C99 from the oxygen head (O), β-face (β), sterol rings A-D (A, B, C, D), and carbon tail segments ($\mathrm{T}_1, \mathrm{T}_2$) (see Chapter 5 Methods). C99-Chol contact maps were computed to define predominant C99-Chol contacts at contact interfaces stabilizied for various chemical states of C99 at 20 mol% Chol.

At interface 1 (Figure 5·8), which includes the GxxxG face, E22,D23[0], E22Q[0], and D23N[0] exhibit rare contacts to the C99 TMD and prominently feature H-bonds of Chol oxygen with K16 (occasionally with K28). These contacts were observed when the JM domain was positioned over the GxxxG face. While the population of interface

1 is higher than all other binding interfaces (Figure 5·7), C99-Chol complexes were not observed to be stabilized by contacts with the GxxxG face in conjunction with the JM domain as originally hypothesized by Beel et al.[104] The GxxxG face only supports C99-Chol complexation when the JM domain is extended into solvent, as observed for E22,D23[-]. The complex is primarily stabilized by H-bonds of K28 with Chol O3 and π-stacking with ring B. Similarly, at other solvation interfaces where H-bonding with K28 to Chol O3 was observed, C99-Chol contacts were formed most prominently with the α-face of Chol with support from π-stacking with ring B, and less frequently with the β-face, with Chol tail groups T_1 and T_2 contacting G38 and I41 (or G37 and V40) and A42 and I45 (or I41 and V44), respectively. C99 E22Q[0] and D23N[0] generally exhibit fewer contacts between the C99 TMD and sterol and tail groups of Chol.

At interface 2 (Figure 5·8), C99-Chol contacts were predominantly stabilized by hydrogen bonds with K16 in C99 E22,D23[0] and N27 and K28 in E22,D23[-] and E22Q[0]. D23N exhibits variable H-bonding of Chol with the JM domain in addition to N27 and K28. At interface 3, K28 H-bonding supports all observed C99-Chol contacts. In C99 E22,D23[-] and D23N[0], these contacts were also supported by K16 H-bonding. At interface 4, C99 E22,D23[0] exhibited prominent β-face binding chiefly stabilized via interaction of T_1 with G38, as well as I41 and T_2 with A42 and V45. C99 E22,D23[-] displayed solvation by the Chol α-face stabilized by various H-bonds with residues 27-30 and π-stacking with ring B. C99 E22Q[0] was observed to form occasional H-bonds solely with K28, while E22,D23[-], E22Q[0], and D23N[0] occasionally engaged in π-stacking with ring B. At interface 5, non-specific H-bonds formed were to the JM domain and turn region in E22,D23[0], accompanied by contacts of Chol tail groups with residues 40, 41, 44, and 45. E22,D23[-] and D22Q[0] both presented qualitatively similar contacts to those observed at interface 4. D23N[0] displayed prominent α- and β-face solvation stabilized by H-bonding with residues 26-30, most often with K28. For C99 E22,D23[-], H-bonding of the JM domain with Chol O3 occured in the rare instances where the unstructured JM domain was inserted in the membrane, as it was observed at interface 1.

Considering C99-Chol interaction in the lower leaflet, absent a reentrant JM helix (including the C-helix[67]), Chol freely contacts residues at the C-terminal end of the TMD. We observed no specific interfaces for C99-Chol association along the C-terminal TMD of C99. Within the lower leaflet, E22,D23[0], E22,D23[-], and E22Q[0]

were all observed to support C99-Chol association via H-bonding of Chol O3 to the lysine anchor $K_{53}K_{54}K_{55}$ and contact between the Chol β- and α-faces (via ring A) along the C-terminal end of the TMD (Figure S4). The end of the Chol tail (T_1, T_2) also forms many contacts with the TMD. D23N[0] Chol complexation in particular was found to be stabilized by interaction of L34 with T_2, facilitated by the enhanced tilt angle of the TMD (see Figure 5·2).

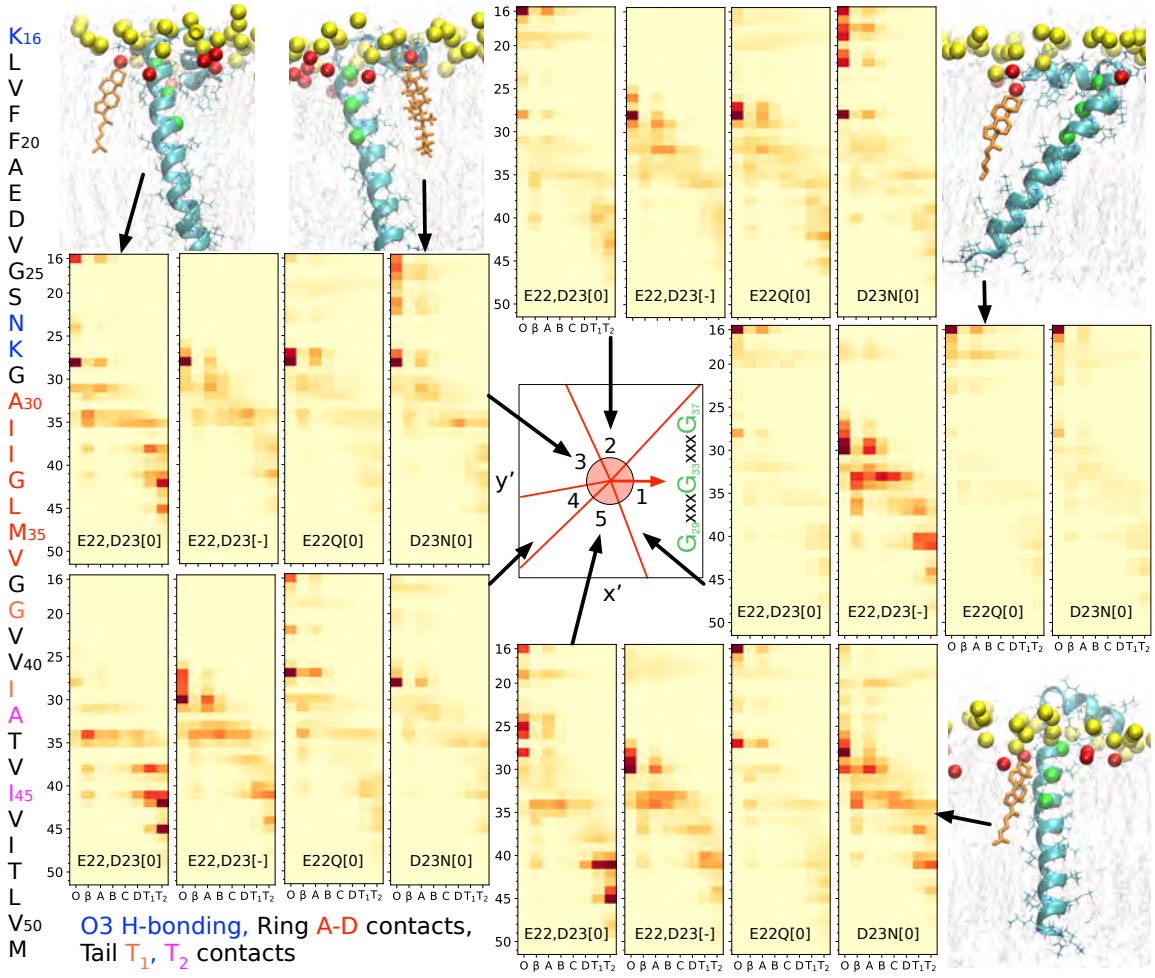

Figure 5·8: >25-ns C99-Chol contact maps at 20 mol% for five upper leaflet C99-Chol solvation interfaces and four forms of C99. Populations are depicted in transformed xy-positions about the GxxxG face director vector (red arrow). Sampled contact likelihoods colored by relative position on a linear scale. Visualizations of representative C99-Chol complexes depicting Chol (orange), $G_{29,33,37}$ (green), and DMPC and Chol phosphorous (yellow) and oxygen (red).

C99-DMPC complex solvates C99 without specificity and outcompetes Lys-Cholesterol Hydrogen Bonding

Given the pattern of C99-Chol solvation interfaces in the upper leaflet, it is reasonable to ask if solvating DMPC is characterized by a spatially complementary mass distribution about the C99 TMD. In fact, we find that C99-DMPC mass densities about the GxxxG face show virtually no preference of DMPC for any face of the C99 TMD (Figure 5·9). This further supports the conjecture that, though cholesterol does not bind C99, it does show spatially anisotropic solvation of C99 (Figure 5·7) in contrast to lipids such as DMPC.

Analysis of C99-DMPC contact maps for dimer associations having >25-ns residence times reveal that, much like Chol, DMPC prominently interacts with the JM domain and the N-loop in addition to the TMD and the Lys anchor. However, interaction with Lys does not appear to be very important for stabilizing C99-DMPC complexes. This lack of specific interaction with Lys, that is responsible for dependence of Chol position on the orientation of the JM domain and N-loop, results in DMPC solvating the C99 TMD without orientational specificity.

We evaluate the average number of monopartite hydrogen bonds and salt bridges formed in each trajectory between one C99 and one Chol or DMPC averaged over the number of replicate trajectories (Table 5.1). The DMPC PC and ester groups each have 4 oxygens which form 44 potential monopartite hydrogen bonds or salt bridges with the 5 Lys of C99. The Chol hydroxyl group can form 17 monopartite hydrogen bonds with the Lys of C99.We observe that the Lys-PC salt bridge substantially outcompetes hydrogen bonding groups, forming 6.7 times more often than the ester group, and 53 times more often than the Chol hydroxyl group. This comparison does not account for the ratio of DMPC/Chol in these systems or the total number of potential monopartite hydrogen bonds available to the PC and ester groups compared to the hydroxyl group. Reweighting the average number of Chol hydrogen bonds observed based on the DMPC/Chol (5/1 at 20 mol%) and the ratio of PC/hydroxyl (or ester/hydroxyl) potential hydrogen bonds and salt bridges (44/17), we find that the PC group is 4 times more likely to form a salt bridge with Lys than form a hydrogen bond with the Chol hydroxyl. However, we do find that the Chol hydroxyl is 1.7 times more likely to hydrogen bond with Lys than the DMPC ester if reweighted in this way. Perhaps it is this slightly higher affinity for the Chol hydroxyl group to Lys over the ester group that manifests anisotropy in the Chol distribution around

Table 5.1: Average and standard deviation in number of hydrogen bonds of Lys to DMPC PC, DMPC Ester, or Chol O3. Extra weight on Lys-Chol hydrogen bonds corresponds to the DMPC/Chol ratio (5, 10, 20 for 20, 10, 5 mol% Chol) and the 44/17 PC/Chol and Ester/Chol ratio of potential monopartite hydrogen bonds (44 for DMPC PC and Ester groups). Statistics over all systems at 20 mol% Chol displayed with the cumulative standard deviation. For 5, 10, and 20 mol% Chol, α = 20x44/17, 10x44/17, and 5x44/17.

C99	<PC>	<Ester>	<O3>	<O3>α
E22,D23[0]	4.3 ± 0.6	0.6 ± 0.1	0.08 ± 0.05	0.99 ± 0.05
E22,D23[-]	3.8 ± 0.4	0.5 ± 0.1	0.06 ± 0.02	0.78 ± 0.2
E22Q[0]	4.8 ± 0.3	0.8 ± 0.2	0.07 ± 0.05	0.95 ± 0.05
D23N[0]	4.1 ± 0.5	0.6 ± 0.2	0.12 ± 0.05	1.51 ± 0.05
Overall	4.25 ± 0.93	0.63 ± 0.32	0.08 ± 0.09	1.06 ± 0.22

E22,D23[0]	<PC>	<Ester>	<O3>	<O3>α
0% Chol	4.1 ± 0.6	0.7 ± 0.1	-	-
5% Chol	3.9 ± 0.5	0.6 ± 0.1	0.02 ± 0.04	0.96 ± 0.04
10% Chol	4.1 ± 0.5	0.6 ± 0.2	0.03 ± 0.03	0.86 ± 0.03

the TMD.

Recently, it was demonstrated that the phosphate-Lys interaction is 0.7 kcal/mol more stable than expected in the CHARMM36 force field. It was suggested that the discrepancy could be corrected by increasing the minimum in the Lennard-Jones potential by 0.08 Å.[390] We did not employ this correction. However, it should be expected that interactions with PC and the hydrogen bonding groups of sphingolipids and gangliosides that are found in lipid rafts, where C99 is evidenced to be processed, would outcompete Chol hydroxyl-Lys interactions. Within plasma membranes, where C99 is thought to play an important role in cholesterol homeostasis, the exo-facing leaflet generally has twice the saturated/unsaturated lipid ratio of the cyto-facing leaflet,[391] making it more likely that the N-terminus of C99, which forms specific but weak complexes with Chol, will be found in lipid raft domains. Therefore, interactions that might contribute to stabilization of a specific, bound C99-Chol dimer are surpassed by interactions between other lipids in the membrane. Nevertheless, cholesterol is expected to interact with C99 in plasma membranes and affect its conformational ensemble.

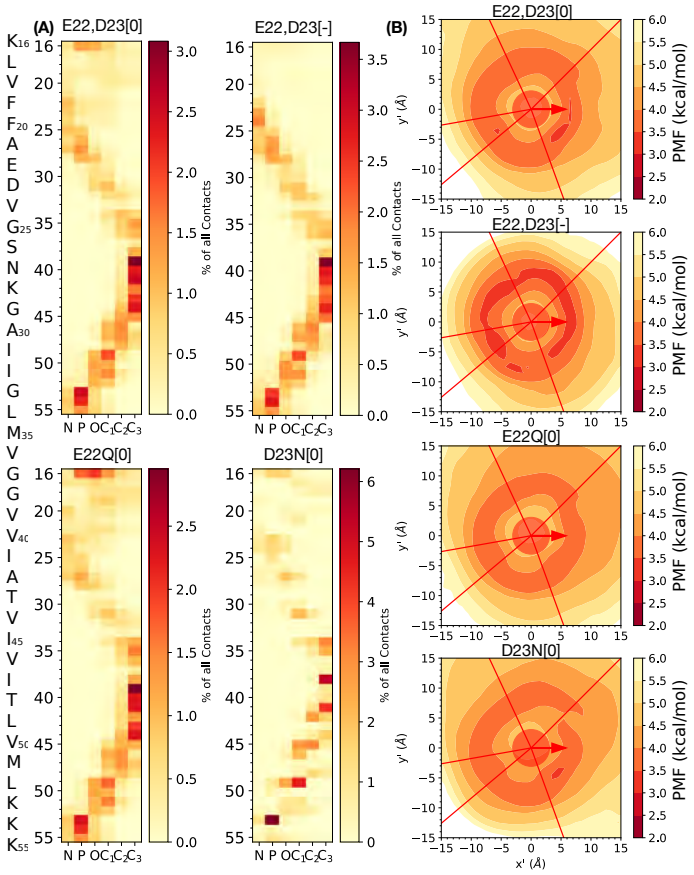

Figure 5·9: (A) >25-ns C99-DMPC contact maps at 20 mol% Chol of both the upper and lower leaflet. (B) Potential of mean force ($-k_{\mathrm{B}}T \ln p(\mathrm{x}', \mathrm{y}')$) of solvating DMPC about the GxxxG director vector (red) of the C99 TMD (circle) and red lines demarcating each of five C99-Chol interfaces.

5.4 Conclusions

Elucidation of the structure, stability, and possible function of C99-cholesterol complexation has received considerable attention since the initial report of specific binding of cholesterol to C99.[98,104] Functional roles proposed for specific binding of cholesterol to C99 have included cholesterol sensing, competition with C99 homodimerization, and C99 partitioning to $\mathrm{L_o}$ "raft" domains containing γ-secretase involved in cleavage of C99 and Aβ biogenesis. Nevertheless, clear characterization of the structure of the C99-Chol complex has proved elusive. To address this fundamental question, we have employed unbiased, rigorously sampled atomistic molecular dynamics simulations to

characterize the nature of C99-cholesterol interaction.

MD simulations of the wildtype sequence of the $C99_{16-55}$ congener protein were performed in DMPC lipid bilayers at 0, 5, 10, and 20 mol% concentrations mimicking prior experimental studies of C99 in bicelles.[5] Formation of the L_o phase was observed at 20 mol% cholesterol, leading to an increase in tilt angle of C99 and impacting the depth of insertion of the JM domain and its orientation relative to the TMD. These changes may be indirectly responsible for changes in chemical shift initially attributed to the binding of cholesterol to C99[5] used to indirectly determine the equilibrium constant of C99-cholesterol dissociation.[53] Indeed, it was found that the C99 heterodimer lifetimes with cholesterol and DMPC manifest as similar power law distributions, displaying no clear signature of a bound C99-cholesterol heterodimer with a characteristic time scale and binding free energy.

For the purpose of investigating how complexed cholesterol might yet affect C99 structure, we investigated cholesterol and DMPC with C99 heterodimer lifetimes exceeding 25-ns as representative of long-lived complexes. We characterized the structure of C99 and C99-cholesterol interactions for C99 charged states representative of endosomal membranes at pH $\leq$ 6.5 (E22,D23[0]) and plasma membranes at neutral pH (E22,D23[-]), as well as the Dutch (E22Q[0]) and Iowa (D23N[0]) FAD mutants at pH $\leq$ 6.5. At 20 mol% cholesterol we found the C99 E22,D23[-] JM domain α-helix to be unstructured and extended into aqueous solvent. In contrast, in E22,D23[0], E22Q[0], and D23N[0] the JM domain features a structured α-helix. Of these, E22,D23[0] and D23N[0] were able to "switch" between a membrane-inserted and membrane-evacuated structure, while E22Q[0] was found to be exclusively inserted into the lipid bilayer.

The wildtype sequence of C99 was observed to support many different orientations of the JM domain relative to the GxxxG face, supporting multiple interfaces for solvation by cholesterol. E22Q[0] and D23N[0] do not exhibit pH switching behavior, instead consistently presenting a stable JM domain α-helix and a restricted set of conformational states. In the upper leaflet, five interfaces defined by orientation of Chol density relative to the GxxxG face were found to describe conformations of the C99 TMD solvated by cholesterol, having free energies derived from potential of mean force calculations within 1 kcal/mol of the experimentally-derived dissociation constant.[53] Most complexes were stabilized by H-bonding of the cholesterol hydroxyl group to K16 and K28 and π-stacking interaction of the second cholesterol ring with the C99 TMD. Within the lower leaflet, complexes were characterized by H-bonding

of cholesterol to the lysine anchor $K_{53}K_{54}K_{55}$, non-specific contacts along the α- and β-face of cholesterol, and interaction of the cholesterol tail with the center of the C99 TMD.

Curiously, it was found that C99-DMPC complexes did not exhibit the specificity for interfaces on the C99 TMD as observed for cholesterol. We attribute this to the lack of necessity for specific interactions with Lys to stabilize the complex as is observed with C99-Chol. Additionally, it was found that DMPC outcompetes cholesterol for hydrogen bonding with Lys, even when weighted for the total number of monopartite hydrogen bonds and salt bridges that may be formed and the DMPC/cholesterol ratio. This further supports the notion that cholesterol does not bind to C99, as the necessary hydrogen bonds are quickly replaced by competition with strongly interacting groups from other lipids.

Using unbiased MD simulations of C99 in DMPC-cholesterol lipid bilayers, we have provided insight into the atomic-level details of C99-cholesterol interactions. Our work suggests that there is no specific C99-cholesterol dimerization interface as initially hypothesized by Beel et al.,[98] and that the C99-Chol dissociation constant determined by Song et al.[53] is consistent with short-lived but specific C99-cholesterol complexes observed in our simulations. Recently proposed[363] roles for C99 regulation of cholesterol homeostasis and Aβ production suggest a role for both lipid raft domains and the pH cellular compartments. The multiple weak cholesterol solvation interfaces with C99 that we describe in this work provide insight into C99-Chol interactions that may play a key role in those environments.

Chapter 6

Structure of Full-Length C99 and Implications for Role of Extra-Membrane Domains in Function and Oligomerization

6.1 Introduction

Currently, the experimental knowledge of extra-membrane residues of C99 is limited to backbone chemical shifts and NOEs measured in LMPG micelles, EPR signals measured in POPC:POPG membranes, and hydrophobic and hydrophilic NMR probe signals in membrane-mimicking detergent bicelles, for which the structural ensembles of residues 6, 12-16, 53-56, 62, 73-76, 80, 81, and 88 are unresolved or too uncertain.[5,6,98] A prodigious body of work characterizing structure of Aβ fragments has been performed and generally suggests that residues 21-28 of Aβ act as a seed for oligomerization and fibril formation. It has been conjectured that this region contains key residues characterizing the aggregation-prone N^* state of Aβ and Aβ fragments.[15,392] Support for this conjecture has been provided by NMR and computational studies of Aβ_{40} and Aβ_{42} structural ensembles.[393] Additionally, the JM domain (K_{16}LVFFAED$_{23}$) and C-loop (residues 53–90) domains show chemical shifts consistent with random coil, implying that they are unstructured on average. However, these domains may exhibit heterogeneity of metastable structural states as has been observed in many intrinsically disordered proteins. A detailed account of C99 structure, domains, and notable mutations and post-translational modifications is provided in Chapter 1.

To address some of the outstanding questions related to the structure of C99 and its interaction with the membrane, we performed simulations of monomeric wildtype C99 in model membranes, using a computational approach that proved to be remarkably useful in elucidating structures of the TMD.[107,114,394] We employed replica-exchange molecular dynamics (REMD)[288] to sample hundreds of nanoseconds of C99 dynamics

at physiological temperatures in 30, 35, and 40 Å-thick membranes modeled using the GBSW implicit solvation method.[272]

In thin membranes, we observed extracellular domain states to be correlated with the TMD state. The mean and variance of the TMD (θ) and GG hinge (κ) angles were observed to increase with thinning of the membrane. The C- and N-terminal secondary and tertiary structures of C99 were heterogeneous with discrete metastable states, which we found to become increasingly correlated as the membrane thickens. These ensembles were directly compared and contrasted with the results of prior solution NMR and EPR studies.[5,6] C99 ensembles were found to exhibit newly-observed metastable α-helical and β-strand structures in C- and N-termini, which are correlated with the state of the TMD in thinner membranes. β-strand structures observed in some N-terminal residues are suggestive of templates that may seed amyloid oligomerization on the membrane surface. α-helical domains in the N-terminus are observed and found to be suggestive of nicastrin association sites. α-helical domains observed in previously uncharacterized phosphorylatable sites T58, S59, and Y86, suggest that these domains may be involved in interactions that enhance phosphorylation processes. Overall, our work provides insights into the structure of extra-membrane residues of C99, and lays the foundation for further investigations probing the role of C99 structure in facilitating interaction with other molecules in membrane.

6.2 Methodology

6.2.1 Initial Structure Preparation

We constructed an initial structure of the full-length C99 sequence using current literature data. Residues 23-55 were modelled using a "Gly-in" structure of one C99 sampled by Dominguez et al.[114] Onto this fragment, residues 1-22 and 56-99 were built using dihedral angles predicted via the TALOS+,[395] using the Cα, Cβ, C, N, and H chemical shifts reported for C99 in LMPG micelles.[98] To remove clashes and effectively move the C-helix close to the membrane surface, the ψ angle of H14, located in the disordered loop of the N-teminus, was adjusted to 180° and the ϕ angle of Q82 was adjusted to 180°. The rotomeric states of residues 1-22 and 56-99 were assigned using the Shapovalov and Dunbrack rotamer library.[396] Protonation states were assigned using the AddH program in UCSF Chimera,[397] assigning negative GLU and ASP, positive LYS and ARG, neutral CYS and TYR, and setting HIS to the

HSD CHARMM histidine type. The center of the membrane was initially set at the z-coordinate of the Cα of G38.

6.2.2 Molecular Dynamics Simulation

All simulations were performed with CHARMM version c41 [278] using the CHARMM36 force field,[398] likely to be the most accurate force field for simulation of Aβ.[399] The GBSW implicit membrane solvent model was used,[272] employing a 0.004 kcal mol^{-1} Å^{-2} surface tension, 5 Å smoothing length from the membrane core-surface boundary, and 0.6 Å smoothing length at the water-membrane surface boundary, using 24 radial and 38 angular integration points to 20 Å. No cutoffs were used for nonbonded interactions. After C99 was inserted in 30, 35, and 40 Å-thick implicit membranes the potential energy was minimized using the steepest descent algorithm until apparent convergence, and simulated for 130, 160, and 460 ns, respectively, using REMD [288] via the REPDSTR utility in CHARMM. We used 16 replicas in REMD simulations, employing exponentially-spaced temperatures from 310 to 500 K and attempting to exchange temperature conditions every 1 ps, manifesting an overall exchange success rate of 17.7 ± 3.7%. Langevin dynamics was employed using a 2 fs time step with a leap frog integrator, a 5 ps^{-1} friction constant, and constrained hydrogen bonds via the SHAKE algorithm. Atomic coordinates were written every 10 ps and all analyses employed coordinate data at this resolution.

6.2.3 Clustering Methods

SHIFTX2 was used to compute the full set of chemical shifts of C99 in each frame for thermodynamic conditions of 7.4 pH and 310 K temperature.[400] All analyses considered structures sampled at equilibrium (past 30 ns) in the 310 K ensemble from REMD. To assign conformational states of extra-membrane domains of C99, a relatively low-dimensional space that enables precise clustering was constructed. Secondary structure assignments were made using the STRIDE implementation in VMD.

To cluster C99 structures four Principal Component Analysis (PCA) eigenspaces were constructed, using Cα positions and the sine and cosine transformations of dihedral angles (dPCA [401]) of N-terminal residues 1-29 and C-terminal residues 52-99, using data from the equilibrium ensemble in 30, 35, and 40 Å membranes. The first 3 prin-

cipal components of simulation data in each of these four eigenspaces were considered relevant, with each conformation of C99 described by a 12-dimensional space capturing the secondary and tertiary structure of the N- and C-terminus. Conformations at each membrane thickness were assigned to states by clustering in this 12-dimensional space using a Gaussian Mixture Model (GMM). The GMM of simulations at each membrane thickness was constructed using k-means clustering to parameterize initial clustering and weights of each data point in each cluster, then refined using 100 iterations of the GMM Expectation-Maximization algorithm.[402] We aimed to construct GMMs that would provide a precise clustering of the most significant conformational states while separating rarely sampled states to small clusters.

To measure the correlation between the N- and C-terminal domains of C99, we cluster the N- an C-terminus separately using the same input data used for the combined clusters of N- and C-terminal domains, constructing N- and C-terminal domain 16-cluster GMMs in 30, 35, and 40 Å membranes. We measure the normalized mutual information

$$\frac{\sum_C^M \sum_N^M p(N,C) \log \frac{p(N,C)}{p(N)p(C)}}{\sqrt{(\sum_N^M p(N) \log p(N))(\sum_C^M p(C) \log p(C))}} \tag{6.1}$$

where M is the number of clusters, $p(N)$ is the likelihood of the N^{th} N-terminus cluster, $p(C)$ is the likelihood of the C^{th} C-terminus cluster, and $p(N,C)$ is the joint probability of the N^{th} and C^{th} cluster. The mutual information ranges from 0 to 1, 1 representing maximum correlation between the N- and C-terminus state changes.

6.3 Results and Discussion

6.3.1 Convergence of Ensemble to Equilibrium and Experiment

Full-length C99 was simulated using REMD in GBSW implicit membranes, a successful approach for enhanced sampling of membrane protein structure.[403] Membranes of 30, 35, and 40 Å thicknesses, corresponding to lipids of 12-, 14-, and 16-carbon sn-1 lipid tails, such as di-12:0 PC (DLPC), di-14:0 PC (DMPC), and 16:0-18:1 PC (POPC), respectively, were used to study the effect of membrane structure on the conformational ensemble of C99.[404] The initial structure of C99, constructed from a combination of past simulations and chemical shift-based dihedral assignments, grad-

ually evolved in REMD simulations to interact with the membrane surface. The radius of gyration (R_g) rapidly converged to the ensemble average in 35 and 40 Å membranes, but appeared to require 20 ns to converge in 30 Å membranes due to relatively slow re-arrangements in secondary structure near the membrane surface (Figure 6·1A). We considered the equilibrium ensemble to have been reached by 30 ns in all REMD simulations, and only consider data at equilibrium for characterization of C99 structure.

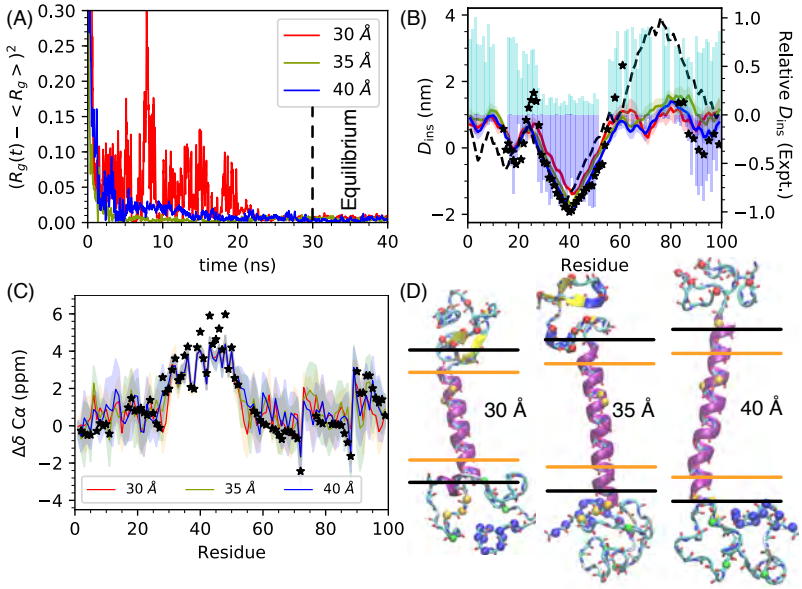

Figure 6·1: (A) Squared difference of R_g from ensemble average over time. The vertical dashed line at 30 ns demarcates the time beyond which the ensembles are considered to be at equilibrium. (B) Equilibrium average and standard deviation of insertion depth of residue Cα in the membrane, D_{ins}. Stars indicate scaled relative depths of residue insertion to the membrane inferred from EPR probe signals in POPG:POPC membranes, dashed line represents insertion depths of the initial C99 structure in a 35 Å membrane.[5] Scaled NMR signals from lipophilic (blue) and hydrophilic (cyan) probes in POPC-DHPC bicelles shown in bars.[6] (C) Equilibrium average and standard deviation of Cα chemical shifts predicted using SHIFTX2. Stars indicate the Cα chemical shifts measured in LMPG micelles. (D) Structures of C99 at 30 ns in 30, 35, and 40 Å membranes. Cα within the atomistic structure are labeled as N-terminal familial AD mutation (red), residues 28, 37, 38, 53, 54, and 55 (orange), phosphorylatable residues Cα (green), and C-helix (blue).

The ensemble average of Cα residue depths of insertion (D_{ins}) in the membrane were well-captured by simulation, comparing well with NMR signals from hydrophobic and hydrophilic probes in POPC-DHPC bicelles and correlating with past EPR measurements in POPG:POPC membranes (40 Å-thick membranes) by Pearson's r of 0.888, 0.861, and 0.894 for 30, 35, and 40 Å membranes, respectively (Figure 6·1B). This is substantially better than the initial structure of C99 prepared for these simulations, which has a Pearson's r correlation with EPR insertion depths of 0.717, deviating most in the C-terminus. This marginally higher insertion depth correlation observed in 40 Å membrane may be attributed to the insertion of the C-helix in the membrane surface. The C-helix was observed to rest on the membrane surface in much of the 40 Å ensemble in contrast with the 30 and 35 Å ensembles that predominantly show residues around T90 to rest on the membrane surface. The higher correlation of C99 residue insertion in 40 Å implicit membranes is taken to be indicative of behavior in POPC membrane, which has been measured to be approximately 40 Å thick in combined analysis of small-angle neutron and x-ray scattering data.[404] The significant deviations in insertion depth at I60 seem to suggest that these implicit membrane simulations can not capture structural features of C99 unique to POPC:POPG membranes, as POPG lipids carry a net negative charge and these implicit membrane simulations attempt to model zwitterionic lipids.

Cα chemical shifts predicted using the SHIFTX2 algorithm, which provides the best correlations of predicted chemical shifts to experiment of current chemical shift prediction methods, show substantial correlation with those measured in LMPG micelles (r correlation coefficients of 0.882, 0.908, and 0.903 for 30, 35, and 40 Å membranes) (Figure 6·1C). However, overall the 40 Å membrane simulations showed higher correlation with all backbone chemical shifts (Table 6.1.[98] Deviations from the LMPG experimental chemical shifts suggest that C99 is slightly too helical in residues 55-70. Furthermore, the degree of lower correlation observed of 30 Å membranes stems from lower propensity for helical structure in residues 90-99. The secondary structure propensities of each residue in conformational states of the extra-membrane region are discussed in further detail below.

Table 6.1: Pearson's r correlations of C99 ensemble averaged chemical shifts with LMPG micelle backbone chemical shifts. Highest correlation of each backbone chemical shift is displayed in bold.

	r(Cα)	r(Cβ)	r(C)	r(N)	r(H)
30 Å	0.882	0.607	0.739	0.484	0.159
35 Å	**0.908**	0.632	0.766	0.560	**0.3646**
40 Å	0.903	**0.793**	**0.787**	**0.570**	0.327

6.3.2 TMD tilt and kink angles

The hinge located at $G_{37}G_{38}$ has been conjectured to modify the interaction of C99 with γ-secretase in a way that impacts C99 processing.[108] As the membrane thickness increases the production of Aβ has been reported to increase overall, but the ratio of Aβ_{42}/Aβ_{40} decreases.[110,111] This suggests that C99 structures in thick membranes are preferable for appropriate interactions of C99 with γ-secretase. The stability of the TMD helix at the GG hinge has been observed to be weaker than the rest of the TMD via H-D exchange experiments.[108,109]

In past simulation studies the GG hinge flexibility did not appear to be sensitive to membrane thickness.[114] However, the simulations presented here include the full C99 sequence, which seems to be important for sampling certain TMD structures. Here, we define the TMD tilt angle (θ) as the angle between the vector of best fit through residue 30-52 Cα positions and the z-axis. The GG hinge angle (κ) is the angle between the vectors of best fit through Cα positions of residues 30-37 and of residues 38-52. In 40 Å membranes there is a single macrostate of TMD structure with average and standard deviation in TMD angles ($< \theta >$) of 7.5° ± 3.9° and GG hinge angles ($< \kappa >$) of 9.3° ± 4.9°. In 35 Å membranes these angles increase to $< \theta > =$ 11.1° ± 5.6° and $< \kappa > =$ 9.9° ± 5.1°. In 30 Å membranes three structural macrostates of the TMD manifest, composing 29.8% (TM1), 66.2% (TM2), and 4.0% (TM3) of the ensemble. Extra-membrane clusters 4, 5, 7, and 8 comprise TM1, featuring $< \theta >$ of 9.1° ± 3.6° and $< \kappa >$ of 16.6° ± 7.0°. Clusters 1, 2, 3, 6, 9, 12 ,13, 14, 15, and 16 comprise TM2, which exhibits $< \theta >$ of 24.3° ± 4.0° and $< \kappa >$ of 14.5° ± 7.0°. Cluster 10 comprises TM3, characterized by $< \theta >$ of 9.3° ± 4.3° and $< \kappa >$ of 46.9° ± 4.8°. The extreme kink in TM3 is an artifact, resulting from unraveling of TMD residues 31-33 to form a β-strand with residues 20-22. We also analyzed the PMF along θ in the 30 Å membrane discarding the TM3 state, finding the energy barrier between TM1 and TM2 to appear at $\theta = 16°$ with approximately 3 kcal/mol, while

the basin of TM1 appears at $\theta = 8°$ with approximately 2.3 kcal/mol and the basin of TM2 appears at $\theta = 25°$ with approximately 1.8 kcal/mol.

These observations suggest that the mean and variance of TMD and GG hinge angles generally increase as a result of membrane thinning. The increase is accompanied by considerable heterogeneity in the C99 structures. In future experiments, these results might be experimentally verified using aligned lipid bilayers with solid-state NMR, RDC solution NMR, or TROSY NMR in bicelles.

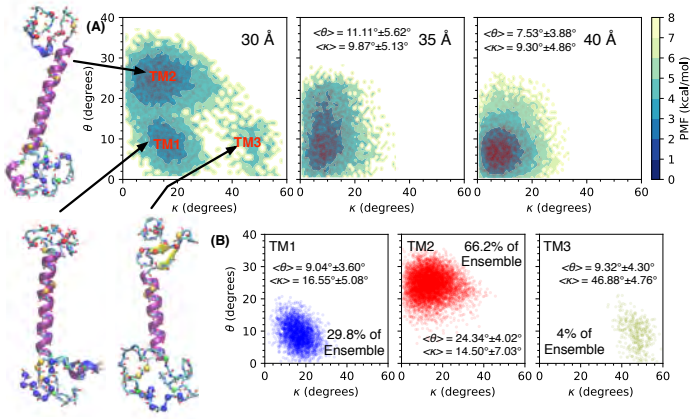

Figure 6·2: TMD (θ) and GG kink (κ) angles of C99 (A) PMF ($-k_BT\ln(p(\theta,\phi))$) at equilibrium in 30, 35, and 40 Å membranes, showing 4,000 randomly selected data points in red and (B) 30 Å membrane for TMD macrostates TM1 (blue), TM2 (red), and TM3 (gold), which compose 66.2, 29.8, and 4% of the equilibrium ensemble, respectively. Insets show mean and standard deviation of angles in the displayed macrostate. Representative C99 conformation secondary structure drawn with STRIDE and Cα colored as defined in Figure 6·1.

6.3.3 Secondary Structure, Membrane Insertion, and Implications of C99 States

The secondary and tertiary structures of extra-membrane residues are heterogeneous. Using projection of simulation data onto a 12-dimensional space the describing relevant PCA eigenvectors of secondary and tertiary structures of N- and C-terminal extra-membrane residues, conformational clusters were assigned and refined using k-means and a Gaussian Mixture Model to find the 16 conformational states defined in 30, 35, and 40 Å membranes. These clusters were inspected by embedding the 12-dimensional space to a 2-dimensional space by metric multidimensional scaling and viewing all assigned atomistic structures. The correlation in changes to the conforma-

tion state of the N- and C-terminal domains was evaluated by constructing 16-cluster GMMs of these domains independently using the same structural information and calculating the normalized mutual information of N- and C-terminal domain cluster assignments (Eq 6.1). We found the correlation between domains to be 0.596, 0.634, and 0.854 in 30, 35, and 40 Å membranes, increasing with membrane thickness. Considering the 8 most populated clusters of each membrane, which account for 75.4, 75.4, and 73.0% of 30, 35, and 40 Å membrane ensembles, we identify the most prominent C99 states. Secondary structure assignment via STRIDE allows for the general classification of structure. We consider the secondary structure propensity by taking the difference between the observed α-helix likelihood (p_α) and the observed β-strand likelihood (p_β) ($p_s = p_\alpha - p_\beta$) for each cluster, such that when $p_s = +1$ the residue has complete α-helical propensity and when p_s = -1 the residue has complete β-strand propensity (Figure 6·3). In each membrane condition, we observe unique secondary structures including or proximal to sites of non-TMD familial AD mutations, phosphorylatable sites, and the metal binding sites. To consider tertiary structure we measured the insertion depth of Cα to the membrane surface (D_{ins}).

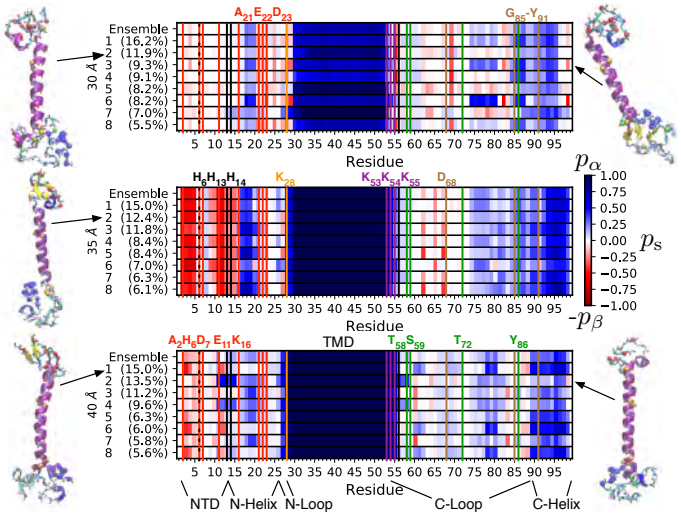

Figure 6·3: Difference of α and β propensity at each C99 residue in the ensemble (see scale for secondary structure propensity on the right) and in the 8 most populous clusters in 30, 35, and 40 Å membranes (percentages correspond to population of the ensemble). Lines and text indicate residue indices of interest: AD-associated mutations (red), phosphorylation sites (green), lysine anchor (purple), metal binding sites (black), Aβ_{33}-producing mutation (orange), and C31 cleavage and cytotoxic function sites (brown). Last frame of visualized C99 clusters with secondary structure drawn with STRIDE and Cα shown as in Figure 6·1.

The TMD is observed to lengthen on both the C- and N-terminal ends with increasing membrane thickness. The TMD was extended by two residues at the N-terminus and one residue at the C-terminus every 5 Å increase in membrane thickness, growing from residues 30-53 in 30 Å membranes to residues 26-55 in 40 Å membranes. This observation is in contrast to the usual assumption[120] that the lysine anchor does not change its registration with the membrane surface, and that only the N-terminal end of the TMD changes registration with the membrane surface as membrane thickness changes. This had previously been unconfirmed, as past experiments on full-length C99 could not resolve structure or membrane insertion of the lysine anchor in a variety of environments.[6] Residue K28, found to change production of Aβ_{40} to Aβ_{33} when mutated to Ala,[120] is incorporated in the TMD helix, undergoing a transition from β to α structure as membrane thickness increases.

In all membrane conditions residues 16-20 have propensity to form helix and be inserted to the membrane (Figure 6·4), in agreement with prior EPR and NMR experiments, as well as the helix previously observed from residues 13-23 in past solution-phase Aβ NMR experiments.[405] The full C-helix, identified as being inserted in membrane in past experiments, is found to be helical in all conditions other than 30 Å, for which residues 96-99 are unstructured and unassociated with the membrane surface. The C-helix is observed to be helical even when unassociated with the membrane surface, a condition observed in some clusters in all membrane conditions. This finding provides a structural basis for the conjecture that the C-helix is available for binding with cytoplasmic proteins in any membrane condition. Residues 73-76, for which membrane insertion and chemical shifts had been previously unresolved in NMR experiments with micelles and bicelles, as well as in EPR experiments with membranes, appear to be unstructured in all membranes and broadly distributed relative to the membrane surface. Residues 74 to 80 are found to be slightly less helical and more bound to the membrane surface in 30 Å membranes, suggesting that thinner membranes may make C99 less available for binding to the G0 protein, which binds residues 61-80.[145] Residue D68, the cleavage site for cytotoxic C31 peptide formation, gains more β-propensity as membrane thins. The cytotoxic functional domain G85-Y91 becomes more α-helical in response to membrane thinning, though the insertion depth does not follow a trend, being membrane-associated in 30 and 40 Å, and membrane-disassociated in 35 Å membranes. It may be possible that C99 in thinner membranes is more amenable to cleavage of D68 to form C31.

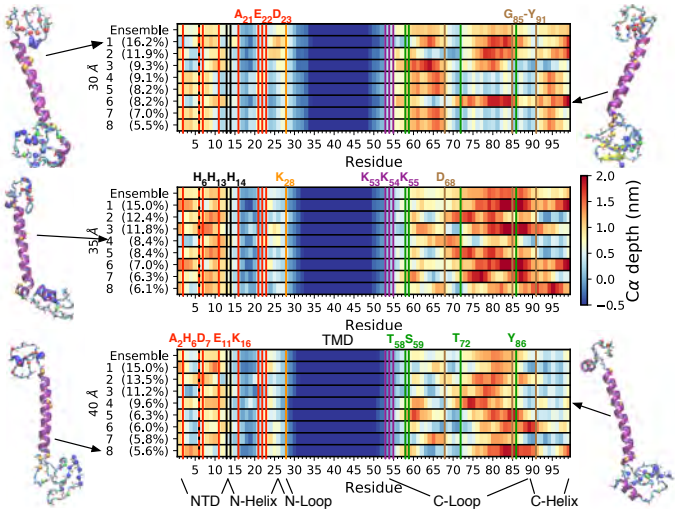

Figure 6·4: Average membrane insertion of each C99 residue Cα (see scale for depth of insertion on the right) in the ensemble and in the 8 most populous clusters in 30, 35, and 40 Å membranes (percentages correspond to population of the ensemble). Lines and text indicate residue indices of interest: AD-associated mutations (red), phosphorylation sites (green), lysine anchor (purple), metal binding sites (black), Aβ_{33}-producing mutation (orange), and C31 cleavage and cytotoxic function sites (brown). Last frame of indicated C99 clusters with secondary structure drawn with STRIDE and Cα shown as in Figure 6·1.

In 30 Å membranes, residues 21-23, 25-27, and 28-30 occasionally interact to form β-strands, suggestive of the aggregation-prone N^* structural motif observed in Aβ fragments.[15,392] This structure is not present in 35 and 40 Å membranes, in which residues 28-30 join the TMD helix. Mutants of residues 21-23 are featured in cases of familial AD and thin membranes are known to cause an increase in the ratio of Aβ_{42}/Aβ_{40} produced. It is possible that mutations in residues 21-23 stabilize this β-strand, altering the TMD ensemble to resemble the structure observed in 30 Å membranes. Additionally, in some clusters, residue K55 forms H-bonds consistent with β-strand structures involving A69, occasionally including Q82 and Q83 as well. In 35 Å membranes, a prominent β-hairpin is formed with residues 2-5 and 11-15, in which residue N27 sometimes participates via H-bonding. This hairpin is positioned away from the membrane surface. This structure does not appear in membrane-bound Aβ_{1-42} in similar implicit membrane simulations,[394] and seems to be unique to 35 Å-thick membranes. It is possible that this β-hairpin structure acts as a seed for Aβ oligomerization. C99-seeded Aβ association to the membrane may be much more favorable than pure Aβ mixtures considered in the past,[22] as Aβ is at sub-

stantially higher concentration outside the cells than in the membrane. Mutation of residues 2, 11, and 16, found in familial AD, may change the propensity for this β-hairpin to form. Additionally, H6, H13, and H14, residues known to bind metal ions found at high concentration in amyloid plaques,[136] are proximate to the observed β-hairpin. The structure of His-ion complexes found in computational investigations of Aβ_{1-16} resembles this hairpin structure.[406,407] As such it may be possible that 35 Å membranes are ideal for stabilizing C99 structures that bind metal ions.

In 40 Å membranes there is weaker propensity for β-hairpin formation observed in 35 Å membranes. A strand with residues 2-5 and 11-13 in some clusters, such as 1, 6, and 8, is observed. In clusters 2 and 4, residues 11-15 form an α-helix that is unassociated with the membrane. Along with residues 16-20, this helix may serve as an interaction site with the nicastrin domain of γ-secretase. The formation of these α-helices may serve to enhance the recognition of C99 by γ-secretase as one possible mechanism explaining the observed increase in Aβ processing observed in thicker membranes.

The secondary structure propensities and insertion depth of non-TMD residues 1-28 and 52-99 for the whole ensemble and for each cluster reveal that the helicity of extra-membrane residues is not correlated with membrane insertion depth. This observation is contrary to typical expectation that the more hydrophobic membrane environment increases the propensity for helical structure. This is quantified by Pearson's r correlation of non-TMD residue secondary structure propensity to membrane insertion of Cα, $r(p_s, D_{ins})$, in the ensemble and in clusters (Figure 6·5). It is indeed possible that this could be a consequence of the simulation model used, and further investigation using explicit solvent simulations with consideration of the disordered protein structure should be pursued.

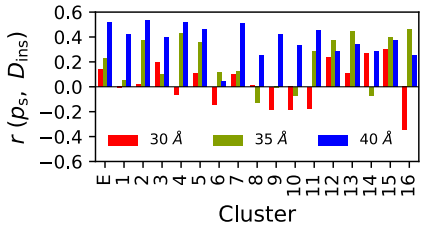

Figure 6·5: Pearson's r correlation of average Cα depth of insertion in membrane (D_{ins}) and difference in observed α and β structure propensity (p_s) in C99 residues 1-28 and 53-99 in the equilibrium ensemble (E) and in each cluster.

6.4 Conclusions

We performed REMD simulations of full-length C99 in model membranes of 30, 35, and 40 Å thicknesses. Heterogeneous but discrete structural states observed in the C99 C- and N-terminal extra-membrane regions of C99 are found to be unique to the specific membrane condition. This observation supports past work on C99 congeners in lipid bilayers[112–114] in which the specific lipid composition, membrane thickness, and membrane curvature were observed to impact C99 monomer and dimer structure. We observe the TMD and $G_{37}G_{38}$ hinge angle means and variances to increase as the membrane thins. Multiple TMD states were found to manifested in thin membranes which were found to be directly correlated with the conformational state of extra-membrane domains. Generally, an increase in α and β secondary structure is observed as membrane thickness increases, accompanied by an increasing correlation of changes in N- and C-terminal domain conformational states. The TMD helix expands on the N- and C-terminal ends as membrane thickness increases. Residues 21-23, 25-27, and 28-30 form β-strands similar to the aggregation-prone N^* motif previously observed in Aβ fragments in 30 Å membranes. In addition, residues 2-5 and 11-15 form a β-hairpin in 35 Å membranes. It is conjectured that these β-strand motifs may serve as seeds for Aβ aggregation on the membrane surface. Residues 11-15 adopt α-helical structures in 40 Å membranes that may promote binding of C99 with the nicastrin domain of γ-secretase to promote non-amyloidogenic processing of C99. α-helical structures are generally stabilized in the C-terminus as membrane thickness increases, and do not require association with the membrane surface. This observation suggests that these domains are readily available to interact with proteins in the cytoplasm. Conversely, residues 85-91, known to be essential to cytotoxic function, become α-helical as the membrane thins. These observations drawn from our simulation study are summarized in Figure 6·6.

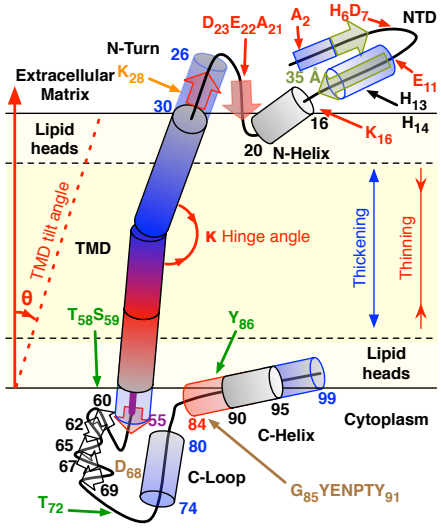

Figure 6·6: Yellow shading represents the hydrophobic environment of the membrane. Secondary structures resulting from membrane thinning (red), membrane thickening (blue), and unique to 35 Å membranes (gold) are transparent. Residue indices are provided to identify regions in which secondary structure is observed. Red residues are found mutated in familial AD, black residues are important for metal binding, green residues are phosphorylatable, orange K28 Ala mutation changes Aβ produced, and brown residues are critical for C31 formation and cytotoxicity. TMD and GG hinge angle means and variance increase with thinning membrane. Black-outlined C-loop β-strands are transient in many membrane conditions.

The insights provided by this study enhance our current understanding of the structural ensemble of full-length C99 in membrane and the potential role played by C99 structure in recognition and processing by γ-secretase. Taken together, these results open the path to investigations of the role of C99 structure in interactions with γ-secretase and Aβ, which may lead to new perspectives on the genesis of amyloid in AD.

Chapter 7

All-atom Ensemble of Full-length APP-C99 Monomer and Homodimer Structures

7.1 Introduction

Congeners of APP-C99 of residues 16-55 in length ($C99_{16-55}$) or shorter are known to form a homodimer primarily defined via the transmembrane domain (TMD) glycine zipper motif $G_{29}xxxG_{33}xxxG_{37}$. This sequence motif is known to play a role in stabilizing homodimers of transmembrane helices, observed most famously in Glycophorin A.[359] The propensity for different dimer motifs, "Gly-in", "Gly-side", and "Gly-out", defined by the Crick angle between C99 homodimers along both Gly33 Cα, have been shown to be dependent on whether lipids are organized into micelles or bilayers, and are dependent on lipid composition.[107,113,114,394] The juxta-membrane (JM) domain, $K_{16}LVFFAED_{23}$, has been demonstrated to form an α-helix (the "N-helix") both in Familial Alzheimer's Disease mutants and in lower pH environments characteristic of endosomes.[102,123]

Solution phase NMR experiments have been used to characterize the structure of full-length C99 in a variety of experimental conditions by the Sanders group using DHPC detergent bicelles.[5,6,98] These experiments, performed at 318.15 K, pH 4.5-6.5, and q (lipid/detergent) ratios of 0.33 or 0.50, have characterized the C99 extra-membrane domains primarily by the assignment of backbone chemical shifts. Using these chemical shift assignments, the accessibility to the lipid bilayer or aqueous solution have been assessed by observing the broadening of peak intensities in the presence of the lipid-like hydrophobic environment probe 16-DOXYL-stearic acid (16-DSA) and the hydrophilic probe, gadopentetic acid (Gd-DTPA). Generally, the observed extra-membrane domain chemical shifts suggest random coil structure and are exposed to solution, and the JM domain and C-terminal domain $Y_{91}KFFEQMQN_{99}$ have been observed to be helical (the "C-helix") and to interact with the lipid bilayer. However,

there is precedent to expect that these extra-membrane domains can express complex ensembles of α-helix and β-strand secondary structure.

C99 N-terminal extra-membrane residues contain part of the Aβ sequence, which participates in stabilizing amyloid oligomer and fibril structures via unique β-strand motifs.[408] The C-terminal extra-membrane residues contain domains used for specific interaction with signaling proteins in the cytosol, in APP, C99, and the γ-cleavage product C31.[409] The observation of chemical shifts suggestive of random coil structure may indeed come from the relatively rapid interconversion of metastable conformational states of these intrinsically disordered residues. Our past simulations of the full-length C99 monomer with the GBSW implicit solvent bilayer model[272] using the CHARMM36 force field[273,274] observed ensembles of metastable states characterized by unique α-helical and β-strand structures dependent on membrane thickness.[67] β-strands observed in the extra-membrane domains were particularly interesting, as these suggested that the C99 N-terminus might be available as a seed for Aβ aggregation on the membrane surface, or that the C99 N-terminus and C-terminus might serve as interfaces for stabilizing the C99 homodimer and other protein-protein interactions.

Recently, Caldwell et al. characterized DHPC bicelles with $q < 1.0$ using small-angle X-ray and neutron scattering, fluorescence anisotropy, and MD simulation, finding $q \leq 0.5$ bicelles to be spheroidal (micellear) in shape, due to mixing of DHPC with other lipids.[410] Additionally, Piai et al. demonstrated that reducing q below 0.7 manifests substantial changes to NMR spectra as q decreases.[411] Indeed, NMR spectra of C99 in DHPC bicelles and LMPG micelles are nearly indistinguishable.[5,6,98] It may be the case that past NMR characterizations of full-length C99 in DHPC bicelles are not wholly representative of C99 structure in lipid bilayers. To address this, recent solution phase bicelle experiments have been performed using n-dodecyl-β-melibioside (DDMB) detergent to successfully solubilize C99 in a variety of lipid compositions including both DMPC:egg sphingomyelin (eSM):Chol (4:2:1) and POPC bicelles[7] at q ratios from 0.33 to 1.0, allowing for characterization of C99 in liquid ordered L_o and liquid disordered L_d environments. These DDMB bicelles were characterized by small-angle X-ray and neutron scattering and cryogenic electron microscopy to be sufficiently oblate, to hold C99 in the disk region, and for the DDMB head groups to be closely packed together, thus forming a stable disk environment excluding DDMB suitable for service as a model lipid bilayer environment. The surfactant mixing issue

observed for DHPC seems to be ameliorated for DDMB due to strong interactions between the DDMB Melibiose (D-galactose-$\alpha(1\rightarrow6)$-D-glucose) head groups which cause DDMB to cluster together at the bicelle annulus.

DDMB bicelles were confirmed to solubilize a distribution primarily composed of C99 monomers, a significant population of C99 homodimers, and rarely-observed C99 homotrimers via Förster resonance energy transfer, electron paramagnetic resonance, double electron electron resonance spectroscopy, chemical linking/sodium dodecyl sulface polycrylamide gel electrophoresis, and native native ion mobility-mass spectrometry. These experiments identified that 16-DSA and Gd-DTPA probes *both* broaden peaks of many extra- and intra-membrane residues along the C99 sequence, suggesting that the C99 monomer and homodimer express a complex distribution of conformational states that make residues of C99 accessible to these hydrophilic and hydrophobic probes. A particularly notable result at high 16-DSA and Gd-DTPA probe concentration, residues 3, 4, and 64-74 were shown to still be inaccessible to these probes. Additionally, both ^{15}N T1/T2 relaxation time ratios and ^{1}H-^{15}N nuclear Overhauser effect T1/T2 ratios showed residues 3, 4, and 64-74 to be mobile. Moreover, the flanking residues 6-8, 61-63, and 77-79 were all found to rapidly exchange amide hydrogens with water in CLEANEX-PM NMR experiments.[412,413] These curious results were suggestive of a C99 homodimer primarily stabilized by a complex ensemble of homodimeric C99 conformations predominantly defined by the C99 C-loop (residues 53-90) and secondarily by the N-terminal extra-membrane domains.

Here, we report generalized Replica Exchange with Solute Tempering (gREST) molecular dynamics (MD) simulations[292] of the C99 monomer and homodimer performed using the CHARMM36m[275] force field to most-accurately model the intrinsically disordered domains evidenced to stabilize the C99 homodimer. We simulate C99 in POPC single-component lipid bilayers, serving as a simple model of a L_d phase bilayer, to which wildtype C99 is evidenced to partition in plasma membranes.[414] We find the C99 monomer to best reproduce the hydrophobic and hydrophilic probe experiments, expressing the re-insertion of the JM domain and a membrane-bond C-helix both not observed in the C99 homodimer. The C99 monomer expressed a truly intrinsically disordered conformational ensemble, for which the optimal number of clusters is on the order of thousands of states. We found the C99 homodimer to exhibit 15 unique conformational states defined by β-strands in extra-membrane domains. These conformations in the homodimer extra-membrane domains are found to

control specific glycine zipper dimer motifs in the TMD. Gly-in conformations were observed when the C99 N-terminus, including the JM domain, formed β-strands. The Gly-out conformation was found to form only when the JM domain formed a helix, which was accompanied by an abolition of β-strand conformation in the N-terminus. The Gly-side conformation was, curiously, observed only when the C-helix forms.
C99 monomer and homodimer C-loops formed β-strands and reside in a globular state, resting away from the lipid bilayer such that they would not interact with 16-DSA, and potentially cause the rejection of hydrophilic Gd-DTPA probe from residues 64-74 observed by Hutchison et al.[7] Overall, these simulations provide new evidence for the role of the C99 extra-membrane domains in stabilizing the C99 homodimer, the nature of the C99 monomer conformational ensemble, and generally demonstrate the importance of modeling intrinsically disordered domains in simulation studies.

7.2 Methodology

7.2.1 Initial Structure Preparation

Residues E22 and D23 were deprotonated as if in a plasma membrane environment at pH 7.4.[102,123] HIS was set to the HSD CHARMM histidine type. The C99 monomer initial structures were prepared from 16 conformational clusters we previously observed in 40 Å-thick implicit GBSW lipid bilayers,[67] embedded into symmetric POPC lipid bilayers of 240 POPC lipids using the CHARMM-GUI membrane builder.[278,380,381] These systems were solvated with 120 water/lipid and 150 nM NaCl (57 Na^+, and 54 Cl^-), containing a total of 120,232 atoms.
The C99 dimer initial structures were prepared by assigning secondary structure of most extra-membrane domain residues (residues 1-22 and 56-99) with random coil dihedral angles built onto transmembrane domain residues (23-55) with coordinates taken from Gly-in and Gly-side conformations previously observed by Dominguez et al.[114] The two initial Gly-in and Gly-side conformations of C99 homodimer were embedded into 602-POPC lipid bilayers with 200 water/lipid and 150 nM NaCl. These initial configurations were equilibrated in conventional MD simulation with the same simulation parameters as later described for 100-200 ns until the random coil structures collapsed into a globular conformation, stable for an additional 100 ns of simulation. These collapsed conformations were used to build a substantially smaller system of 400-POPC lipid bilayers, 170 water/lipid, and 150 nM NaCl (173

Na^+, and 167 Cl^-), containing a total of 260,160 atoms used for generalized Replica Exchange with Solute Tempering (gREST) simulations.[292] Both C99 monomer and C99 homodimer simulations were minimized with steepest descent to convergence, then annealed for 1 ns from 10 to 310 K prior to gREST simulation.

7.2.2 Molecular Dynamics Simulation

Both the RIKEN K-Computer and the Institute of Molecular Science Molecular Simulation computers were used to simulate the C99 monomer and dimer with conventional MD and gREST. All simulations were performed using the GENESIS 1 SPDYN molecular dynamics engine.[279,280] gREST simulations were used to equilibrate and simulate the C99 monomer and dimer using an effective temperature scheme employing 16 replicas at linearly-spaced temperatures from 310 to 340 K. Simulations of the monomer C99 defined the solute to include Lennard-Jones, dihedral, and CMAP terms of residues 1-28 and 53-99 of C99 and all head group and ester atoms of POPC. Simulations of homodimeric C99 defined the solute to include Lennard-Jones, dihedral, and CMAP of all atoms of C99 and POPC. Replica exchanges were attempted every 10 ps and system coordinates were saved at the same frequency. A time step of 2.5 fs was used for the integration with the Velocity Verlet algorithm and long-range electrostatic interactions were computed every two steps via the RESPA multiple time-step integration.[415,416]

The CHARMM36m force field was used for both C99 monomer and homodimeric systems[273–275] and the CHARMM TIP3P water model was used for water.[417] Simulations of the C99 homodimer employed a reduction to all protein-lipid Lennard-Jones interactions by a factor of 0.9 to stabilize the homodimer, the scaling factor developed by Domański et al. to capture the proper free energy of dimerization in the Glyocophorin A homodimer, which also features a glycine zipper motif.[418] A similar gREST scheme and protein-lipid scaling factor to those used in this study were found to be effective for capturing the conformational ensemble of the FGFR3 homodimer validated on solid-state NMR experiments.[293]

Because the C99 monomer and dimer feature intrinsically disordered domains, it is possible that rare, fully-extended conformations are possible in the C99 monomer and dimer. To avoid interactions of the C99 N- and C-termini across the PBC along the z-axis or N-terminus-to-N-terminus or C-terminus-to-C-terminus interaction across the PBC along the xy-plane, we applied 10 kJ mol^{-1} $Å^{-1}$ flat-bottom harmonic restraints

to the N- and C-termini to maintain the termini in non-fully-extended conformational ensembles. For the C99 monomer, 6.5 nm flat-bottom pair restraints were applied to Cα of residues 1, 11, 89, and 99 to Cα of residue 41. For the C99 homodimer, 8.0 nm flat-bottom pair restraints were applied to Cα of residues 1, 87, and 99 to residue 41. Lennard-Jones interactions were smoothed to zero by 12 Å with force switching beginning at 10 Å. Atom pair lists were defined with a 13.5 Å distance. Long-range electrostatic interactions were calculated with smooth Particle Mesh Ewald sums.[419] The bonds including hydrogen atoms were constrained using RATTLE[420] or SHAKE,[421] and water was treated as a rigid body using SETTLE.[383] The Bussi rescaling thermostat[353] and barostat[422] were applied, with temperature set to 310 K with $\gamma_t = 1$ and pressure set to 1 atm with $\gamma_p = 0.5$. Monomeric and homodimeric C99 gREST simulations ran for 500 and 550 ns, respectively.

7.2.3 Hierarchical Clustering and Scoring

In contrast to our past simulations of the C99 monomer,[67] a combination of Cα position and dihedral PCAs of the N- and C-terminal extra-membrane residues was not effective in discriminating distinct conformational states of the C99 dimer. Rather than the previous 12-dimensional space constructed from PCAs to measure distance between conformation, we employed a simple measure of distance based on the root-mean-square deviation (RMSD) of a set of Cα pair distances between two different conformations. The most effective selection was to consider all pair distances between Cα of residues 1-28 (378 distances) and of residues 53-99 (1035 distances), for a total of $N_{pairs} = 1413$ pair distances. The RMSD of these distances (dRMSD) between all pairs of conformations (all simulation frames after equilibration) is used as the distance metric for conformational clustering, expressed as

$$\mathrm{dRMSD}(i,j) = \sqrt{\frac{1}{N_{pairs}} \sum_{k}^{N_{pairs}} \left(d_i(k) - d_j(k)\right)^2}, \tag{7.1}$$

where $d_i(k)$ and $d_j(k)$ are the k^{th} interatomic distance of the the i^{th} and j^{th} conformation (frame). With dRMSD serving as a measure of distance between all conformations, we employed Ward's minimum variance hierarchical clustering[423] to cluster conformations of the C99 monomer and dimer. To determine the best number of clusters, we employed the Silhouette scoring metric.[424] The measure of how well each

conformation, i, is clustered in a partitioning into k number of clusters is measured as

$$a(i) = \frac{1}{N_{C_i} - 1} \sum_{j \in C_i, i \neq j} \text{dRMSD(i, j)}, \tag{7.2}$$

$$b(i) = \min_{i \notin C_l} \frac{1}{N_{C_l}} \sum_{j \in C_l} \text{dRMSD(i, j)}, \tag{7.3}$$

$$s(i) = \frac{b(i) - a(i)}{\max\{a(i), b(i)\}}, \tag{7.4}$$

$$\tag{7.5}$$

where $a(i)$ defines the mean dRMSD of conformation i to the $N_{C_i} - 1$ other conformations assigned to the same cluster as i, $b(i)$ defines the minimum mean dRMSD of conformation i to N_{C_l} conformations indexed by j in each of k clusters indexed by l, and $s(i)$ defines the silhouette value of conformation i. The silhouette score, S is simply the average of all s given the number of clusters, k,

$$S(k) = \frac{1}{N_{conf}} \sum_{i}^{N_{conf}} s_k(i). \tag{7.6}$$

Silhouette scores were calculated for 2 to 30,000 clusters for the C99 monomer and dimer, and clustered conformations for k clusters at and around peaks in $S(k)$ were visually inspected prior to concluding that maxima in $S(k)$ provided the best clusterings of each system.

7.2.4 Equilibration

gREST simulations from the initial structures were likely not part of the equilibrium conformational ensemble. Because these proteins are intrinsically disordered and also begin from a globular initial conformation, we had no order parameter available to confirm convergence of these gREST simulations to equilibrium. Instead, we evaluate the convergence of the observed likelihood of visits to each effective temperature by each replicate trajectory over the course of the simulation to the observed likelihood of visits to each temperature for the full gREST simulation. This measure reaches convergence by definition and provides a rationale for determining which timescale in

the simulation to analyze as part of the equilibrium ensemble. $\Omega(t)$ is defined as

$$\Omega(t) = \frac{1}{N_{\text{rep}}} \sum_{i}^{N_{\text{rep}}} \sum_{j}^{N_{\text{rep}}} \left(p(T_j, t)_i - p(T_j)_i\right)^2 \tag{7.7}$$

where N_{rep} is the number of replica trajectories and temperatures, $p(T_j)_i$ is observed likelihood of visits the i^{th} trajectory to the j^{th} effective temperature, T_j, for the full gREST simulation, and $p(T_j, t)_i$ is the observed likelihood of visits to the i^{th} trajectory to the j^{th} temperature for the gREST simulation up to time t.

7.3 Results

7.3.1 Convergence of Ensembles to Equilibrium

Following recent NMR experiments characterizing an ensemble of C99 monomers and homodimers in bicelles with well-structured disks capable of solubilizing C99, we have performed large-scale gREST[292] simulations using the CHARMM36m[275] force field to interrogate the conformational ensemble of full-length C99 in explicit solvent all-atom MD simulations. The C99 monomer and homodimer were simulated for 450 and 500 ns, respectively. The initial state of the C99 monomer was proposed using 16 conformational states determined in our previous replica exchange molecular dynamics (REMD)[288] simulations of the full-length C99 monomer in 40 Å-thick (30 Å hydrophobic thickness) implicit solvent bilayers,[67] of similar thickness to POPC bilayers.[404] The initial state of the C99 homodimer was constructed from Gly-in and Gly-side conformations of the C99 homodimer TMD[114] with random coil structures of the N- and C-terminal extramembrane domains, which were simulated in conventional MD up until 100 ns after collapse of the N- and C-terminal extramembrane domains to a globular state. The convergence of gREST simulations to equilibrium was evaluated using an ergodic measure-like[425–427] metric based on the observed likelihoods of visits of each trajectory to each effective temperature, T, condition, $\Omega(t)$ (Eq. 7.7). By this criteria, we observe that the C99 monomer and dimer simulations quickly converge to near the overall observed distribution of visits to each T by ∼175 ns in the monomer and ∼125 ns in the homodimer, followed by a slower convergence to the final probability distribution (Figure 7·1A,B). We chose to consider the final 300 ns of simulation data at an effective temperature of 310 K in both the monomer

and homodimer for analysis as the equilibrium ensemble. The probability distribution of trajectory visits to each T show that the C99 monomer gREST simulation performed a good random walk in T space (Figure 7·1C). The C99 homodimer mostly did as well, with the exception of the 14^{th} trajectory, which was significantly more trapped on the low-temperature end of T space compared to other trajectories.

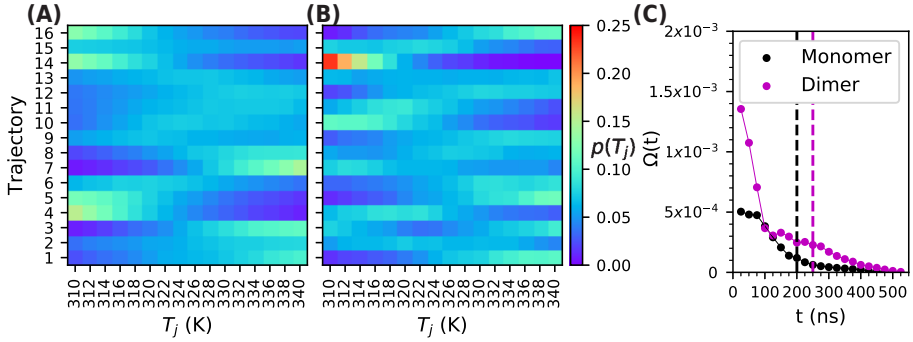

Figure 7·1: Observed likelihoods of visitation to each j^{th} effective temperature for each i^{th} trajectory, $p(T_j)$ for gREST simulations of the (A) C99 monomer and (B) C99 dimer. (C) Convergence of mean differences from $p(T_j)$ for observed likelihoods measured up to time t, $p(T_j, t)$.

7.3.2 Accessibility of C99 to hydrophobic and hydrophilic environments in MD and NMR

Some equilibrium ensemble characterizations of the C99 monomer and homodimer simulated in gREST, and of the distribution of C99 monomer and dimers in NMR experiments, can be indirectly compared. The accessibility of C99 to hydrophilic probe Gd-DTPA and hydrophobic probe 16-DSA, measured as $1 - I/I_0$, the ratio of NMR peak intensities from probe solutions divided by the intensities observed in probe-free solutions, is often analogous to the height (or depth) of residues above (below) the lipid bilayer surface, which may be defined as the average z-axial position of the POPC phosphorous atom in each lipid leaflet. This is because 16-DSA contains a stearic acid lipid tail which inserts to the lipid bilayer, and Gd-DTPA is a 545.56 g mol^{-1} complex with 5 carboxylate groups, making it both bulky and hydrophilic. Measurements of $1 - I/I_0$ for both 16-DSA and Gd-DTPA in both POPC (L_d) and DMPC:eSM:Chol 4:2:1 (L_o) DDMB bicelles match reasonably well with the height of C99 monomer Cα carbons above the lipid bilayer surface (Figure 7·2). C99 homodimer does not capture any signature of a re-insertion of the JM domain to the

membrane, which is observed in the NMR probe experiments, nor does the C99 homodimer exhibit much variation in the location of the C-terminus, both on and away from the membrane surface, as observed for the C99 monomer and in the 16-DSA and Gd-DTPA NMR experiments.

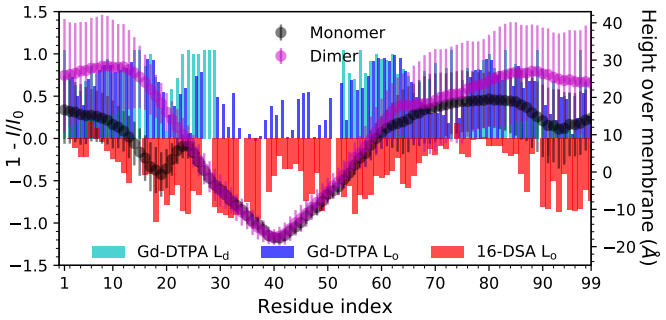

Figure 7·2: I/I_0 is the ratio of C99 NMR signals in presence of hydrophilic (Gd-DTPA) and hydrophobic (16-DSA) probes over intensities observed in NMR peak assignments, and average height of C99 monomer and homodimer residues above phosphorous in lipid leaflets observed in gREST simulations at effective temperature $T = 310$ K at equilibrium. L_d phase Gd-DTPA experiment performed with 350 μM C99 in 5 wt % in solution $q = 0.33$ POPC bicelle with 1.5 mM Gd-DTPA. L_o phase Gd-DTPA and 16-DSA experiments performed with 300 μM C99 in 7 wt% in solution $q = 0.33$ DMPC:eSM:Chol 4:2:1 bicelles and 16 mol% 16-DSA in lipid mixture or 3 mM Gd-DTPA in solution.[7]

Gd-DTPA experiment results in both L_d and L_o phase lipid bilayers are nearly indistinguishable, with the exception of more accessibility to water in residues 20-29, implying that these residues are more deeply inserted in the bilayer and that the JM domain is more α-helical in L_o phase bilayers. This behavior has been observed previously in simulations employing the $C99_{16-55}$ congener when L_o phase was introduced as a function of Chol in DMPC bilayers.[123]

7.3.3 C99 monomer is intrinsically disordered, manifests the C-helix, and features significant β-strand propensity in the C-loop

Using the RMSD of pair distances of N- and C-termini Cα as a criterion of distance between conformations of C99, we clustered the C99 monomer and homodimer using Ward's minimum variance hierarchical clustering[423] and computed silhouette scores, S, for k number of clusters to determine the most appropriate number of clusters

and cluster assignments to describe C99 conformations. Silhouette scores for the C99 monomer plateau on the order of thousands of states, and decrease linearly to zero on the order of tens of thousands of states (Figure 7·3A). As such, monomeric C99 is similar to monomeric Aβ in that the protein conformational ensemble has an enormous number of metastable states.[428] For the sake of partitioning the ensemble into some non-ideal partitioning of C99 monomer conformational states, we chose to make a clustering of 350 states, which is an apparent elbow in $S(k)$. With this clustering, we find the population of C99 monomer conformational states to be a mix of exponential and linear decay as a function of cluster size (Figure 7·3B).

A minority of these conformational states express α-helices in the C-terminus and JM domain. This suggests the presence of the C-helix and N-helix-like domains for which there were strong signatures observed in LMPG and DHPC $q = 0.33$ and 0.5 systems at pH 4.5-6.5[5,6,98] and for which there are weaker signatures observed in the recent more bilayer-like DDMB bicelle experiments.[7] We identify this subset of conformations as conformational clusters that express a propensity for residues 22 or 23, or residues 94 or 95, to accept or donate a backbone hydrogen bond with residues $i \pm (3, 4, 5)$. Of these 350 clusters, we find 53 clusters to express the C-helix at over 40% propensity, and observed C-helix in 15.31% of the conformational ensemble (Figure 7·3C). Only 3 clusters expressing the N-helix at over 40% propensity were observed, and the N-helix comprised just 4.92% of the conformational ensemble. The lack of N-helix is not a surprising result at pH 7.4, however, as we have previously demonstrated.[102,123]

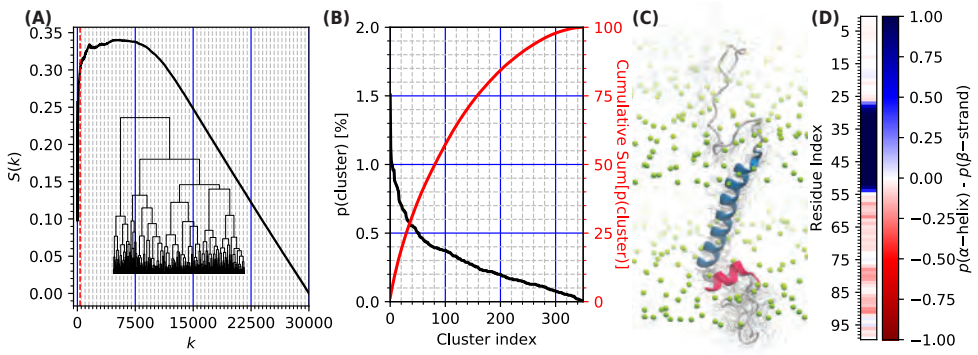

Figure 7·3: Analysis of C99 monomer. (A) Silhouette scores for Ward's minimum variance hierarchical clustering (inset dendrogram) for partitionings of k number of clusters. Dashed red line is at $k = 350$. (B) Percent of conformational ensemble for each cluster, p(cluster) (black), ranked in order from largest to smallest, and the cumulative sum of p(cluster) (red). (C) 7^{th} largest cluster of a the 350-cluster partitioning, TMD in blue, C-helix in red, and POPC phosphorous in green. (D) Ensemble-averaged secondary structure of monomer ensemble assigned using STRIDE.

The C99 monomer expresses significant but widely varying β-strand character throughout the extra-membrane domains (Figure 7·3D). The β-strand propensity observed throughout the C99 monomer C-loop and globular conformation may protect residues 64-74 such that bulky Gd-DTPA solvation might be impeded, as observed in DDMB bicelle NMR experiments.[7]

7.3.4 C99 homodimer consists of metastable states defined by N- and C-terminal β-strands

Silhouette scores of C99 homodimer clustering show that 15 clusters is the optimal number of clusters to represent the conformational ensemble (Figure 7·4A). The secondary structure of these clusters are characterized by unique β-strands formed between N- and C-terminal extra-membrane domains (Figure 7·4B). The N-helix only partially manifests in the 2^{nd} largest cluster, as it is present in only 3.85% of the ensemble. The C-helix manifests in the 9^{th}, 10^{th}, 12^{th}, and 13^{th} largest clusters, and is present in 28.90% of the ensemble. However, both the C- and N-helix conformations observed in the homodimer do not associate with the membrane surface, as they do in the monomer (Figure 7·2).

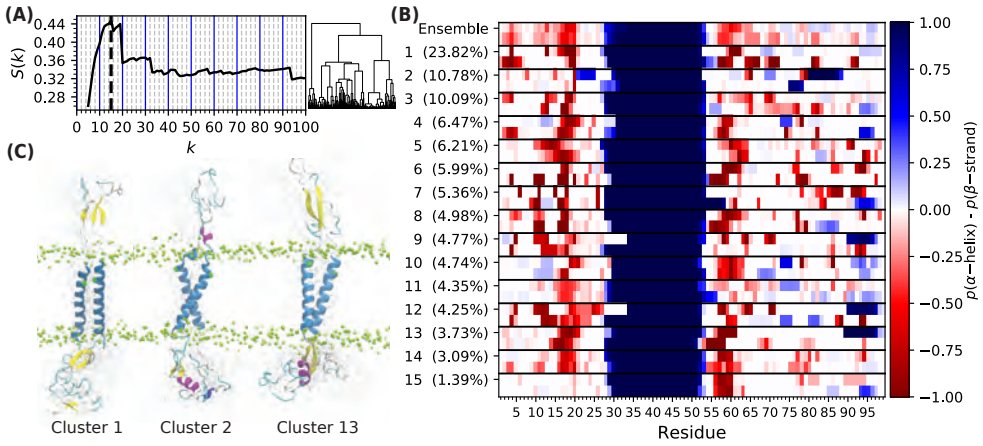

Figure 7·4: Analysis of C99 homodimer. (A) Silhouette scores for Ward's minimum variance hierarchical clustering (inset dendrogram) for partitionings of k number of clusters. Dashed black line is at $k = 15$. (B) Ensemble average and population-ranked cluster secondary structures assigned using STRIDE. (C) Representative conformations of 1$^{\text{st}}$, 2$^{\text{nd}}$, and 13$^{\text{th}}$ largest clusters. TMD in blue, C-helix in red, POPC phosphorous and Gly33 Cα in green.

7.3.5 C99 glycine zipper homodimerization depends on extra-membrane domain state

As can be seen in Figure 7·4C, the conformation of extra-membrane domains can determine the structure of the C99 homodimer in the TMD. We evaluate the xy-plane Crick angles ($\Psi^{\text{G33}}_{\text{Crick}}$), defined by the vector of Gly33 Cα oriented away from center of the helix, and the dihedral formed by vectors of Gly29-Gly37 Cα of one C99 to Gly37-Gly37 Cα of both proteins to Gly37-Gly29 Cα of the opposing protein, $\phi_{\text{Gly29Gly37}}$. Gly-in, Gly-side, and Gly-out conformations are well-partitioned by conformational clusters (Figure 7·5A). Gly-out was formed only by the 2$^{\text{nd}}$ largest cluster. Gly-side was formed only by the 12$^{\text{th}}$ and 13$^{\text{th}}$ largest clusters. The remainder of clusters formed Gly-in homodimers.

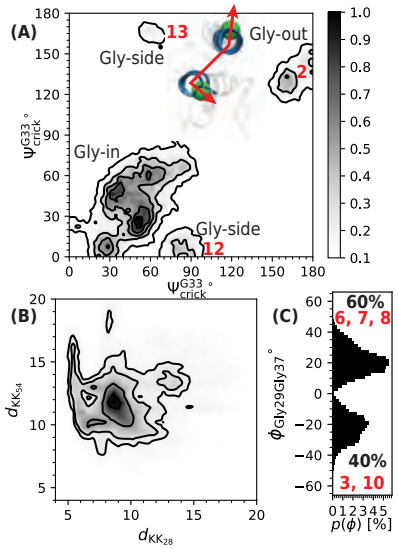

Figure 7·5: Observed likelihood distributions in C99 homodimer of (A) Crick angles.12$^{\text{th}}$ and 13$^{\text{th}}$ largest clusters are Gly-side (inset). 2$^{\text{nd}}$ largest cluster is Gly-out. (B) Distances between Cα of K28-K28 and K54-K54. (C) dihedral of Gly29-Gly37-Gly37-Gly29 Cα. 6, 7, and 8$^{\text{th}}$ largest clusters are exclusive to left-handed coils (overall 60% of coils) and 3$^{\text{rd}}$ and 10$^{\text{th}}$ largest clusters are exclusive to right-handed coils (overall 40% of coils).

Unlike Crick angles, the distances between K28 and K54 (Figure 7·5B), previously used as a metric to assign describe unique conformations of the homodimer sensitive to membrane curvature and composition,[113] are not well-partitioned by these same clusters. The handedness of the homodimer coil, however, is partitioned by some clusters. The 6, 7, and 8$^{\text{th}}$ largest clusters exclusively formed left-handed ($\phi > 0°$) coils (overall 60% of coils) and the 3$^{\text{rd}}$ and 8$^{\text{th}}$ largest clusters exclusively formed right-handed ($\phi < 0°$) coils (overall 40% of coils) (Figure 7·5). As such, we can see that the extra-membrane domains control the relative rotation of the C99 TMDs, but do not necessarily control features of the homodimer coil, such as the inter-helix distances and supercoil handedness.

7.4 Conclusions

We performed large-scale all-atom explicit solvent gREST MD simulations of full-length C99 monomer and homodimer at neutral pH in POPC bilayers. The C99 monomer was found to best-reproduce improved NMR measurements of C99 chemical

shifts and measures of accessibility to hydrophobic and hydrophilic probes in DDMB bicelles. The C99 monomer was found to be intrinsically disordered, described by thousands of metastable states. C99 monomer was found to express a majority population of β-strands in the C-loop and a minority population of C-helix. The C99 homodimer was found to express 15 metastable conformational states stabilized by β-strands in the N- and C-terminal extra-membrane domains. Extra-membrane domain secondary structures were found to directly control the Crick angles (relative rotation) of TMD helices, and to effect, but not directly control, the conformation of the homodimer supercoil. These results provide a rich picture of the C99 monomer and homodimer conformational ensemble and generally provide a detailed case study demonstrating the importance of membrane protein intrinsically disordered domains in determining the conformation of transmembrane protein domains.

Chapter 8

Conclusions and Future Perspectives

8.1 General Conclusions

Though there is a large body of work studying proteins in the amyloid cascade, there are many open fundamental questions regarding the role of lipid bilayers and membrane proteins in the Amyloid Cascade Hypothesis of Alzheimer's Disease. This is primarily due to the difficulty in experimentally characterizing (1) protein structure in lipid bilayers, (2) the local lipid environment of proteins in real and model lipid bilayers, and (3) lipid and cholesterol both in the vicinity of, and interacting with, membrane proteins. State of the art hardware, molecular dynamics (MD) simulation software, and MD force fields made it possible to study complex lipid and protein systems in the past decade. We have completed various studies of C99, the single-pass transmembrane protein precursor to amyloid β, simulations of lipid phase separations, and the effect of cholesterol on C99 and lipid phase separations.

In the preceding chapters we have described work examining the effect of finite size on the lipid miscibility transition and, using the results from that work, studied the role of cholesterol in inducing complex phases in equimolar mixtures of saturated and unsaturated lipid. We studied the effect of cholesterol on the structure of $C99_{16-55}$ congener, finding cholesterol to change the conformational ensemble of C99 not through specific interactions as previously thought, but via non-specific interaction and induction of the L_o phase. We performed the first simulations of full-length C99 monomer, first via implicit solvent lipid bilayer simulations and later in explicit solvent models, finding β-strand conformations in extra-membrane domains suggestive of interaction interfaces with other proteins. In addition, we found the C99 monomer to be characterized by an intrinsically disordered ensemble, not dissimilar from Aβ monomer. We also simulated the full-length C99 homodimer, finding C99 extra-membrane domains to stabilize metastable conformational states via β-strands in the homodimer. Conformational states of the homodimer were found to control the relative rotation

of TMD helices, but without direct control over the structure of the superhelix coil. These exploratory investigations have provided molecular details of the structure of lipid bilayers and C99 protein relevant to a better understanding of the Amyloid Cascade Hypothesis and to membrane biophysics in general. A perspective for future work building on these investigations is provided below.

8.2 Future Perspectives

8.2.1 Effect of Aspect Ratio on Miscibility Transition Critical Size and Line Tension

Our work on the effect of finite size on the miscibility transition of ternary lipid mixtures was performed in x:y 1:1 aspect ratio bilayers. Within the context of our Flory-Huggins model, if we were to change the aspect ratio of the lipid bilayer, the phase separation interface would form along the shortest of the two axes (of length L_s) in the xy-plane because this minimizes the line tension, $\frac{2L}{d}\chi$. Therefore, increasing the aspect ratio of a two-dimensional system should decrease the critical size, N_c, required to stabilize phase separation. Of course, this would lead to the conclusion that a very large aspect ratio, say one where $L_\mathrm{s} = d$, the lattice spacing, would minimize N_c. This certainly is true in a lattice model, but is unreasonable for a quasi-two-dimensional system such as a lipid bilayer, for which physical properties depend on mechanical properties of the lipid layer. Moreover, the line tension of a phase separation is defined mechanically by the interfacial wave between lipid domains, which is limited in period by the length of L_s.[429]

Manipulation of the aspect ratio to stabilize phase separations has been a common practice for the simulation of three-dimensional phase separations, such as the water-vapor interface[430] and protein phase separation.[431] However, there have not been investigations to our knowledge of how much aspect ratios in such systems can reasonably be manipulated without significantly affecting the surface tension and other physical properties.

How do we choose an N and x:y ratio that substantially reduces N_c without manifesting unrealistic behavior? Are there some generalizable observations in terms of N, χ, and x:y ratio that can be found? Is there a simple rule of thumb we can find for using manipulated aspect ratios for simulations of phase separation? Addressing these questions may be helpful for modeling phase separated lipid bilayers by substantially

reducing the number of atoms in the system.

8.2.2 Lipid Domain Partitioning of C99

Recently, we observed that MARTINI simulations of proteins in phase separating lipid mixtures will partition to the interface between L_o and L_d domains.[429] We expanded upon our Flory-Huggins model of phase separation to include a protein at the domain interface to understand how protein preference for L_o or L_d domains and χ determine how a protein will partition in a phase separated system. We found that, generally, proteins with weak preferences for either domain will partition to the domain interface. It has been reported that C99 partitions to L_d domains in the plasma membrane to interact with ADAM10. However, C99 must also interact with BACE1 and γ-secretase, which are evidenced to partition to L_o domains. The recent fluorescence spectroscopy experiments by Capone et al. determined fluorescence-labeled C99 to have a partitioning of $p_{L_o} = 0.13 \pm 0.09$ in giant plasma membrane vesicles, strongly preferring the L_d phase.[414]

It is important to note that fluorescence spectroscopy methods for determining the partitioning coefficient of proteins between L_o and L_d domains are unable to determine if proteins are at the domain interface. C99 might also localize to the interface between domains, particularly at very low C99 concentrations, as assumed in our Flory-Huggins model.

We have performed *de novo* simulations of two $C99_{16-55}$ in the phase separating mixture DPPC:DUPC:Chol 36.7:36.7:26.6 at 295 K in the CHARMM36 force field using the Anton 2 ASIC computer at the Pittsburgh Supercomputing Center (Figure 8·1A). A key result from this simulation is that the C99 TMD generally has 20% nearest neighbor contacts with DPPC lipids, sitting on the L_d side of the L_o-L_d domain interface after the L_o phase is formed by 2 μs, while occasionally migrating to the L_d bulk (Figure 8·1B). It was observed that the all-atom time scale of lipid phase separation is 40 times slower than in coarse-grained simulations employing MARTINI 2. In addition, the all-atom simulations required time steps of 2.4 fs in contrast to the 20-40 fs time steps used in the MARTNI model. Moreover, all-atom models contain approximately 10 times more atoms than MARTINI models. Therefore, all-atom MD simulations of phase separation are approximately 5000 times slower than MARTINI 2 simulations of the same number of molecules (Figure 8·1C).

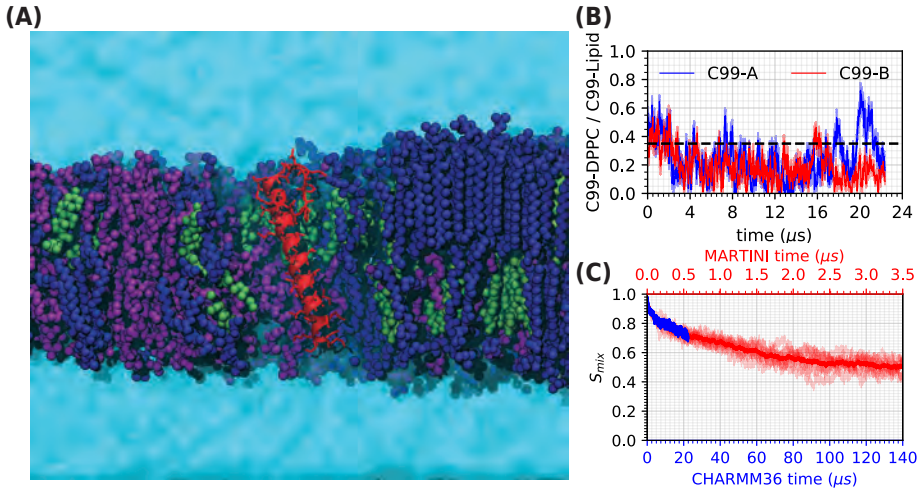

Figure 8·1: (A) $C99_{16-55}$ (red) at L_o-L_d domain interface in DPPC:DUPC:Chol 36.7:36.7:26.6 (blue, purple, green) bilayer, 496,452 atoms. (B) Ratio of C99-DPPC and C99-DPPC + C99-DUPC contacts. For two C99, A and B. Dashed black line at 0.35 represents approximate limit of L_o-L_d interface environment. (C) Mixing entropies of phase separation in CHARMM36 (blue) and in equivalent MARTINI 2 system (red).

We conclude that all-atom simulation on even the most powerful MD ASIC with publically available allocations challenged to model *de novo* lipid phase separation. Rather than take a direct simulation approach, free energy methods like umbrella sampling are likely necessary for determining the partitioning of proteins to lipid domains.[432] It may be that not only C99 partitions to L_o-L_d domain interfaces, but that BACE1 does so as well, despite the apparent affinity of BACE1 for L_o domains. Processing of APP by BACE1, or C99 by γ-secretase, at such domain interfaces would be a remarkable result. These observations suggest a potential explanation for the mysteries of APP-BACE1 and C99-γ-secretase association. Umbrella sampling simulations can be performed using massively parallel calculations on GPUs up to the microsecond time scale, which may be sufficient for sampling the free energy of these proteins across a phase separated lipid domain boundary.

There are other questions that can be explored with free energy simulations beyond protein partitioning. The polarity of protein TMDs for L_o or L_d faces at the domain interface can be explored by sampling the free energy along an axis of rotation about the z-axis. Likewise, the free energies profiles of C99-ADAM10 and C99-BACE1 TMD associations might be evaluated to determine if the TMDs participate in complexes

with C99 in addition to the extra-membrane active sites. The increasing availability of new and powerful GPUs may usher in a wide variety of such new free energy calculations on membrane proteins.

8.2.3 Bilayer simulations with user-specified initial positions

Currently used software for building lipid bilayer systems create random mixtures of lipids and potentially other molecules onto lattices.[306,381,433] There are currently no tools for directly controlling the spatial distribution and precise locations of lipids, proteins, or any other molecules in a lipid bilayer.

It is relatively easy to visualize and treat systems composed of layers of individual molecules (such as lipid bilayers) as a square or hexagonal lattice. We did this when developing Flory-Huggins models to model finite size effects in phase separation[335] and the partitioning of proteins to lipid domains.[429] Generalizing this perspective, we can consider the two-dimensional lattice to be a kind of digital canvas, within which each pixel can be defined not only by a color, but by other data, such as the topology and coordinates of a molecule.

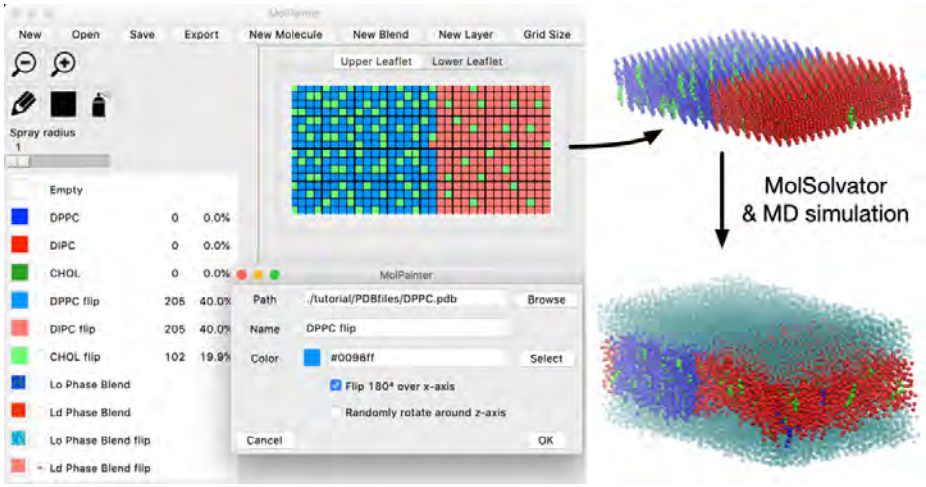

Figure 8·2: MolPainter Graphical User Interface example constructing a phase separated lipid bilayer.

I have recently developed a tool, MolPainter, for "painting" molecules onto "canvases" representing lattices each defined at different z-axial positions. The lattice sites each have an area per site, similar to an area per lipid. MolPainter enables the rapid construction of very complex layered molecular systems composed of any molecules,

though with obvious applications for modeling complex lipid membranes.

In MolPainter, the user creates a "palette" of molecules, each associated with a color and optional operations to be performed on their initial coordinates, specified in the PDB file the user provides to describe each molecule. Users select molecules to paint lattices on each canvas, assigning the molecule to each lattice site. Multiple molecules can also be "blended" together with a certain probability distribution, for example, a "L_o" phase blend of 1:2 DPPC:Chol, can be painted onto the canvas and be used to quickly paint L_o domains. When MolPainter exports a painting, the coordinates of the molecules are copied, if specified, rotated, and then translated to each lattice site either using an atom selection specified in the PDB or the center of geometry of the molecule.

MolPainter makes tasks like constructing a lipid phase separation as the initial condition for a molecular simulation very straightforward (Figure 8·2). MolPainter also has a supplemental tool, MolSolvator, which can rapidly build a box of any solvent around layered systems built in MolPainter. Both MolPainter and MolSolvator use PDB files for easy input/output of molecules and systems. MolPainter also has its own python dictionary-based files for saving and loading paintings. Examples of unique applications using MolPainter to build symmetric or asymmetric lipid bilayer phase separations, S_{oc} phases, and placement of cholesterol or lipids into the bilayer mid-plane. It is my hope that more creative, hypothesis-driven initial conditions for complex molecular systems will become commonplace in the near future through the development and use of software similar to MolPainter.

References

[1] P. F. F. Almeida. Thermodynamics of lipid interactions in complex bilayers. *Biochimica et Biophysica Acta - Biomembranes*, 1788:72–85, 2009.

[2] S. H. Donaldson and H. B. de Aguiar. Molecular Imaging of Cholesterol and Lipid Distributions in Model Membranes. *The Journal of Physical Chemistry Letters*, 9:1528–1533, 2018.

[3] L. Chen, Z. Yu, and P. J. Quinn. The partition of cholesterol between ordered and fluid bilayers of phosphatidylcholine: A synchrotron X-ray diffraction study. *Biochimica et Biophysica Acta - Biomembranes*, 1768:2873–2881, 2007.

[4] M. Belička, A. Weitzer, and G. Pabst. High-resolution structure of coexisting nanoscopic and microscopic lipid domains. *Soft Matter*, 13:1823–1833, 2017.

[5] P. J. Barrett, Y. Song, W. D. Van Horn, E. J. Hustedt, J. M. Schafer, A. Hadziselimovic, A. J. Beel, and C. R. Sanders. The Amyloid Precursor Protein Has a Flexible Transmembrane Domain and Binds Cholesterol. *Science*, 336: 1168–1171, 2012.

[6] Y. Song, K. F. Mittendorf, Z. Lu, and C. R. Sanders. Impact of Bilayer Lipid Composition on the Structure and Topology of the Transmembrane Amyloid Precursor C99 Protein. *Journal of the American Chemical Society*, 136: 4093–4096, 2014.

[7] J. M. Hutchison, K. C. Shih, H. A. Scheidt, S. M. Fantin, K. F. Parson, G. A. Pantelopulos, H. R. Harrington, K. F. Mittendorf, S. Qian, R. A. Stein, S. E. Collier, M. G. Chambers, J. Katsaras, M. W. Voehler, B. T. Ruotolo, D. Huster, R. L. McFeeters, J. E. Straub, M. P. Nieh, and C. R. Sanders. Bicelles Rich in both Sphingolipids and Cholesterol and Their Use in Studies of Membrane Proteins. *Journal of the American Chemical Society*, 142: 12715–12729, 2020.

[8] H. Hippius and G. Neundörfer. The discovery of Alzheimer's disease. *Dialogues in Clinical Neuroscience*, 5:101–108, 2003.

[9] D. J. Selkoe. In the beginning ... *Nature*, 354:432–433, 1991.

[10] J. Hardy and G. Higgins. Alzheimer's disease: the amyloid cascade hypothesis. *Science*, 256:184–185, 1992.

[11] J. Hardy. The amyloid hypothesis for Alzheimer's disease: A critical reappraisal. *Journal of Neurochemistry*, 110:1129–1134, 2009.

[12] A. E. Roher, T. A. Kokjohn, S. G. Clarke, M. R. Sierks, C. L. Maarouf, G. E. Serrano, M. S. Sabbagh, and T. G. Beach. APP/Aβ structural diversity and Alzheimer's disease pathogenesis. *Neurochemistry International*, 110:1–13, 2017.

[13] R. Gallardo, N. A. Ranson, and S. E. Radford. Amyloid structures: much more than just a cross-β fold. *Current Opinion in Structural Biology*, 60: 7–16, 2020.

[14] G. P. Morris, I. A. Clark, and B. Vissel. Inconsistencies and Controversies Surrounding the Amyloid Hypothesis of Alzheimer's Disease. *Acta Neuropathologica Communications*, 2:135, 2014.

[15] J. E. Straub and D. Thirumalai. Toward a molecular theory of early and late events in monomer to amyloid fibril formation. *Annual Review of Physical Chemistry*, 62:437–463, 2011.

[16] E. N. Cline, M. A. Bicca, K. L. Viola, and W. L. Klein. The Amyloid-β Oligomer Hypothesis: Beginning of the Third Decade. *Journal of Alzheimer's Disease*, 64:S567–S610, 2018.

[17] M. P. Lambert, A. K. Barlow, B. A. Chromy, C. Edwards, R. Freed, M. Liosatos, T. E. Morgan, I. Rozovsky, B. Trommer, K. L. Viola, P. Wals, C. Zhang, C. E. Finch, G. A. Krafft, and W. L. Klein. Diffusible, nonfibrillar ligands derived from Aβ1-42 are potent central nervous system neurotoxins. *Proceedings of the National Academy of Sciences of the United States of America*, 95: 6448–6453, 1998.

[18] S. Mandrekar-Colucci and G. E. Landreth. Microglia and Inflammation in Alzheimers Disease. *CNS & Neurological Disorders - Drug Targets*, 9:156–167, 2012.

[19] A. ElAli and S. Rivest. Microglia in Alzheimer's disease: A multifaceted relationship. *Brain, Behavior, and Immunity*, 55:138–150, 2016.

[20] C. Cheignon, M. Tomas, D. Bonnefont-Rousselot, P. Faller, C. Hureau, and F. Collin. Oxidative stress and the amyloid beta peptide in Alzheimer's disease. *Redox Biology*, 14:450–464, 2018.

[21] J. J. Kremer and R. M. Murphy. Kinetics of adsorption of β-amyloid peptide Aβ(1-40) to lipid bilayers. *Journal of Biochemical and Biophysical Methods*, 57:159–169, 2003.

[22] D. J. Lindberg, E. Wesén, J. Björkeroth, S. Rocha, and E. K. Esbjörner. Lipid membranes catalyse the fibril formation of the amyloid-β (1–42) peptide through lipid-fibril interactions that reinforce secondary pathways. *Biochimica et Biophysica Acta - Biomembranes*, 1859:1921–1929, 2017.

[23] P. Flagmeier, S. De, T. C. Michaels, X. Yang, A. J. Dear, C. Emanuelsson, M. Vendruscolo, S. Linse, D. Klenerman, T. P. Knowles, and C. M. Dobson. Direct measurement of lipid membrane disruption connects kinetics and toxicity of Aβ42 aggregation. *Nature Structural and Molecular Biology*, 27: 886–891, 2020.

[24] M. F. Sciacca, C. Tempra, F. Scollo, D. Milardi, and C. La Rosa. Amyloid growth and membrane damage: Current themes and emerging perspectives from theory and experiments on Aβ and hIAPP. *Biochimica et Biophysica Acta - Biomembranes*, 1860:1625–1638, 2018.

[25] J. Lee, Y. H. Kim, F. Arce, A. L. Gillman, H. Jang, B. L. Kagan, R. Nussinov, J. Yang, and R. Lal. Amyloid β Ion Channels in a Membrane Comprising Brain Total Lipid Extracts. *ACS Chemical Neuroscience*, 8:1348–1357, 2017.

[26] D. C. Bode, M. D. Baker, and J. H. Viles. Ion channel formation by amyloid-β42 oligomers but not amyloid-β40 in cellular membranes. *Journal of Biological Chemistry*, 292:144–1413, 2017.

[27] F. Tofoleanu and N. V. Buchete. Alzheimer Aβ peptide interactions with lipid membranes: Fibrils, oligomers and polymorphic amyloid channels. *Prion*, 6: 339–345, 2012.

[28] L. Martin, X. Latypova, C. M. Wilson, A. Magnaudeix, M. L. Perrin, C. Yardin, and F. Terro. Tau protein kinases: Involvement in Alzheimer's disease. *Ageing Research Reviews*, 12:289–309, 2013.

[29] G. S. Bloom. Amyloid-β and tau: The trigger and bullet in Alzheimer disease pathogenesis. *JAMA Neurology*, 71:505–508, 2014.

[30] M. Jin, N. Shepardson, T. Yang, G. Chen, D. Walsh, and D. J. Selkoe. Soluble amyloid β-protein dimers isolated from Alzheimer cortex directly induce Tau hyperphosphorylation and neuritic degeneration. *Proceedings of the National Academy of Sciences of the United States of America*, 108:5819–5824, 2011.

[31] K. Plaschke, J. Kopitz, M. Siegelin, R. Schliebs, M. Salkovic-Petrisic, P. Riederer, and S. Hoyer. Insulin-resistant brain state after intracerebroventricular streptozotocin injection exacerbates Alzheimer-like changes in Tg2576 AβPP-overexpressing mice. *Journal of Alzheimer's Disease*, 19:691–704, 2010.

[32] J. K. Morris and J. M. Burns. Insulin: An Emerging Treatment for Alzheimer's Disease Dementia? *Current Neurology and Neuroscience Reports*, 12:520–527, 2012.

[33] D. Kellar and S. Craft. Brain insulin resistance in Alzheimer's disease and related disorders: mechanisms and therapeutic approaches. *The Lancet Neurology*, 19:758–766, 2020.

[34] S. Kumar-Singh, J. Theuns, B. Van Broeck, D. Pirici, K. Vennekens, E. Corsmit, M. Cruts, B. Dermaut, R. Wang, and C. Van Broeckhoven. Mean age-of-onset of familial Alzheimer disease caused by presenilin mutations correlates with both increased Aβ42 and decreased Aβ40. *Human Mutation*, 27:686–695, 2006.

[35] N. Tang and K. P. Kepp. Aβ42/Aβ40 Ratios of Presenilin 1 Mutations Correlate with Clinical Onset of Alzheimer's Disease. *Journal of Alzheimer's Disease*, 66:939–945, 2018.

[36] T.-H. Xu, Y. Yan, Y. Kang, Y. Jiang, K. Melcher, and H. E. Xu. Alzheimer's disease-associated mutations increase amyloid precursor protein resistance to γ-secretase cleavage and the Aβ42/Aβ40 ratio. *Cell Discovery*, 2:16026, 2016.

[37] R. Riek and D. S. Eisenberg. The activities of amyloids from a structural perspective. *Nature*, 539:227–235, 2016.

[38] X. Yang, G. Meisl, B. Frohm, E. Thulin, T. P. Knowles, and S. Linse. On the role of sidechain size and charge in the aggregation of Aβ42 with familial mutations. *Proceedings of the National Academy of Sciences of the United States of America*, 115:E5849–E5858, 2018.

[39] U. C. Müller, T. Deller, and M. Korte. Not just amyloid: Physiological functions of the amyloid precursor protein family. *Nature Reviews Neuroscience*, 18:281–298, 2017.

[40] S. O. Dahms, S. Hoefgen, D. Roeser, B. Schlott, K.-H. Guhrs, and M. E. Than. Structure and biochemical analysis of the heparin-induced E1 dimer of the amyloid precursor protein. *Proceedings of the National Academy of Sciences*, 107:5381–5386, 2010.

[41] S. Hoefgen, S. O. Dahms, K. Oertwig, and M. E. Than. The amyloid precursor protein shows a pH-dependent conformational switch in its E1 domain. *Journal of Molecular Biology*, 427:433–442, 2014.

[42] S. O. Dahms, M. C. Mayer, D. Roeser, G. Multhaup, and M. E. Than. Interaction of the amyloid precursor protein-like protein 1 (APLP1) E2 domain with heparan sulfate involves two distinct binding modes. *Acta Crystallographica Section D: Biological Crystallography*, 71:494–504, 2015.

[43] L. C. Roisman, S. Han, M. J. Chuei, A. R. Connor, and R. Cappai. The crystal structure of amyloid precursor-like protein 2 E2 domain completes the amyloid precursor protein family. *The FASEB Journal*, 33:5076–5081, 2019.

[44] I. Coburger, S. O. Dahms, D. Roeser, K. H. Gührs, P. Hortschansky, and M. E. Than. Analysis of the overall structure of the multi-domain amyloid precursor protein (APP). *PLoS ONE*, 8:1–12, 2013.

[45] P.-H. Kuhn, H. Wang, B. Dislich, A. Colombo, U. Zeitschel, J. W. Ellwart, E. Kremmer, S. Roßner, and S. F. Lichtenthaler. ADAM10 is the physiologically relevant, constitutive α-secretase of the amyloid precursor protein in primary neurons. *The EMBO Journal*, 29:3020–3032, 2010.

[46] J. Prox, C. Bernreuther, H. Altmeppen, J. Grende, M. Glatze, R. D'Hooge, S. Stroobants, T. Ahmed, D. Balschun, M. Willem, S. Lammich, D. Isbrandt, M. Schweizer, K. Horré, B. De Strooper, and P. Saftig. Postnatal disruption of the disintegrin/metalloproteinase ADAM10 in brain causes epileptic seizures, learning deficits, altered spine morphology, and defective synaptic functions. *Journal of Neuroscience*, 33:12915–12928, 2013.

[47] H. Cai, Y. Wang, D. McCarthy, H. Wen, D. R. Borchelt, D. L. Price, and P. C. Wong. BACE1 is the major β-secretase for generation of Aβ peptides by neurons. *Nature Neuroscience*, 4:233–234, 2001.

[48] X. Zhang and W. Song. The role of APP and BACE1 trafficking in APP processing and amyloid-β generation. *Alzheimer's Research and Therapy*, 5: 1, 2013.

[49] R. J. Andrew, K. A. Kellett, G. Thinakaran, and N. M. Hooper. A Greek tragedy: The growing complexity of Alzheimer amyloid precursor protein proteolysis. *Journal of Biological Chemistry*, 291:19235–19244, 2016.

[50] H. S. Nhan, K. Chiang, and E. H. Koo. The multifaceted nature of amyloid precursor protein and its proteolytic fragments: friends and foes. *Acta Neuropathologica*, 129:1–19, 2015.

[51] A. Kimura, S. Hata, and T. Suzuki. Alternative Selection of β-Site APP-Cleaving Enzyme 1 (BACE1) Cleavage Sites in Amyloid β-Protein Precursor (APP) Harboring Protective and Pathogenic Mutations within the Aβ Sequence. *Journal of Biological Chemistry*, 291:24041–24053, 2016.

[52] M. Kolev, M. Ruseva, C. Harris, B. Morgan, and R. Donev. Implication of Complement System and its Regulators in Alzheimers Disease. *Current Neuropharmacology*, 7:1–8, 2009.

[53] Y. Song, E. J. Hustedt, S. Brandon, and C. R. Sanders. Competition Between Homodimerization and Cholesterol Binding to the C99 Domain of the Amyloid Precursor Protein. *Biochemistry*, 52:5051–5064, 2013.

[54] R. Aguayo-Ortiz, C. Chávez-García, J. E. Straub, and L. Dominguez. Characterizing the structural ensemble of γ-secretase using a multiscale molecular dynamics approach. *Chem. Sci.*, 8:5576–5584, 2017.

[55] M. Okochi, S. Tagami, K. Yanagida, M. Takami, T. S. Kodama, K. Mori, T. Nakayama, Y. Ihara, and M. Takeda. γ-Secretase Modulators and Presenilin 1 Mutants Act Differently on Presenilin/γ-Secretase Function to Cleave Aβ42 and Aβ43. *Cell Reports*, 3:42–51, 2013.

[56] P.-H. Kuhn, A. V. Colombo, B. Schusser, D. Dreymueller, S. Wetzel, U. Schepers, J. Herber, A. Ludwig, E. Kremmer, D. Montag, U. Müller, M. Schweizer, P. Saftig, S. Bräse, and S. F. Lichtenthaler. Systematic substrate identification indicates a central role for the metalloprotease ADAM10 in axon targeting and synapse function. *eLife*, 5:1–29, 2016.

[57] E. Jorissen, J. Prox, C. Bernreuther, S. Weber, R. Schwanbeck, L. Serneels, A. Snellinx, K. Craessaerts, A. Thathiah, I. Tesseur, U. Bartsch, G. Weskamp, C. P. Blobel, M. Glatzel, B. De Strooper, and P. Saftig. The disintegrin/metalloproteinase ADAM10 is essential for the establishment of the brain cortex. *Journal of Neuroscience*, 30:4833–4844, 2010.

[58] R. A. Kovall, B. Gebelein, D. Sprinzak, and R. Kopan. The Canonical Notch Signaling Pathway: Structural and Biochemical Insights into Shape, Sugar, and Force. *Developmental Cell*, 41:228–241, 2017.

[59] H. Treiber, N. Hagemeyer, H. Ehrenreich, and M. Simons. BACE1 in central nervous system myelination revisited. *Molecular Psychiatry*, 17:237–239, 2012.

[60] Y. Luo, B. Bolon, M. A. Damore, D. Fitzpatrick, H. Liu, J. Zhang, Q. Yan, R. Vassar, and M. Citron. BACE1 (β-secretase) knockout mice do not acquire compensatory gene expression changes or develop neural lesions over time. *Neurobiology of Disease*, 14:81–88, 2003.

[61] M. S. Wolfe. Structure and Function of the γ-Secretase Complex. *Biochemistry*, 58:2953–2966, 2019.

[62] J. Shen, R. T. Bronson, D. F. Chen, W. Xia, D. J. Selkoe, and S. Tonegawa. Skeletal and CNS Defects in Presenilin-1-Deficient Mice. *Cell*, 89:629–639, 1997.

[63] F. Panza, M. Lozupone, G. Logroscino, and B. P. Imbimbo. A critical appraisal of amyloid-β-targeting therapies for Alzheimer disease. *Nature Reviews Neurology*, 15:73–88, 2019.

[64] L. M. Bekris, C.-E. Yu, T. D. Bird, and D. W. Tsuang. Review Article: Genetics of Alzheimer Disease. *Journal of Geriatric Psychiatry and Neurology*, 23:213–227, 2010.

[65] R. Vassar. ADAM10 Prodomain Mutations Cause Late-Onset Alzheimer's Disease: Not Just the Latest FAD. *Neuron*, 80:250–253, 2013.

[66] S. Todd, A. J. McKnight, W. W. Liu, R. Carson, S. Heggarty, B. McGuinness, G. B. Irvine, D. Craig, A. P. Passmore, and J. A. Johnston. BACE1 polymorphisms do not influence platelet membrane β-secretase activity or genetic susceptibility for alzheimer's disease in the northern irish population. *NeuroMolecular Medicine*, 10:368–376, 2008.

[67] G. A. Pantelopulos, J. E. Straub, D. Thirumalai, and Y. Sugita. Structure of APP-C99 1–99 and implications for role of extra-membrane domains in function and oligomerization. *Biochimica et Biophysica Acta (BBA) - Biomembranes*, 1860:1698–1708, 2018.

[68] C. Bi, S. Bi, and B. Li. Processing of mutant β-amyloid precursor protein and the clinicopathological features of familial alzheimer's disease. *Aging and Disease*, 10:383–403, 2019.

[69] A. Rostagno, J. L. Holton, T. Lashley, T. Revesz, and J. Ghiso. Cerebral amyloidosis: Amyloid subunits, mutants and phenotypes. *Cellular and Molecular Life Sciences*, 67:581–600, 2010.

[70] N. M. Li, K. F. Liu, Y. J. Qiu, H. H. Zhang, H. Nakanishi, and H. Qing. Mutations of beta-amyloid precursor protein alter the consequence of Alzheimer's disease pathogenesis. *Neural Regeneration Research*, 14:658–665, 2019.

[71] A. Capell, H. Steiner, M. Willem, H. Kaiser, C. Meyer, J. Walter, S. Lammich, G. Multhaup, and C. Haass. Maturation and pro-peptide cleavage of β-secretase. *Journal of Biological Chemistry*, 275:30849–30854, 2000.

[72] E. Marcello, C. Saraceno, S. Musardo, H. Vara, A. G. de la Fuente, S. Pelucchi, D. Di Marino, B. Borroni, A. Tramontano, I. Pérez-Otaño, A. Padovani, M. Giustetto, F. Gardoni, and M. Di Luca. Endocytosis of synaptic ADAM10

in neuronal plasticity and Alzheimer's disease. *Journal of Clinical Investigation*, 123:2523–2538, 2013.

[73] J. H. Chyung, D. M. Raper, and D. J. Selkoe. γ-Secretase Exists on the Plasma Membrane As an Intact Complex That Accepts Substrates and Effects Intramembrane Cleavage. *Journal of Biological Chemistry*, 280:4383–4392, 2005.

[74] S. Parvathy, I. Hussain, E. H. Karran, A. J. Turner, and N. M. Hooper. Cleavage of Alzheimer's amyloid precursor protein by α-secretase occurs at the surface of neuronal cells. *Biochemistry*, 38:9728–9734, 1999.

[75] C. Venugopal, C. Demos, K. Jagannatha Rao, M. Pappolla, and K. Sambamurti. Beta-Secretase: Structure, Function, and Evolution. *CNS & Neurological Disorders - Drug Targets*, 7:278–294, 2008.

[76] E. H. Koo, S. L. Squazzo, D. J. Selkoe, and C. H. L. B. I. I. I. T. A. P. P. Koo4. Trafficking of cell-surface amyloid β-protein precursor. *Journal of Cell Science*, 109:991–998, 1996.

[77] R. G. Perez, S. Soriano, J. D. Hayes, B. Ostaszewski, W. Xia, D. J. Selkoe, X. Chen, G. B. Stokin, and E. H. Koo. Mutagenesis identifies new signals for β-amyloid precursor protein endocytosis, turnover, and the generation of secreted fragments, including Aβ42. *Journal of Biological Chemistry*, 274: 18851–18856, 1999.

[78] J. T. Huse, D. S. Pijak, G. J. Leslie, V. M. Lee, and R. W. Doms. Maturation and endosomal targeting of β-site amyloid precursor protein-cleaving enzyme. The Alzheimer's disease β-secretase. *Journal of Biological Chemistry*, 275: 33729–33737, 2000.

[79] L. Pastorino, A. F. Ikin, A. C. Nairn, A. Pursnani, and J. D. Buxbaum. The carboxyl-terminus of BACE contains a sorting signal that regulates BACE trafficking but not the formation of total Aβ. *Molecular and Cellular Neuroscience*, 19:175–185, 2002.

[80] E. H. Koo and S. L. Squazzo. Evidence that production and release of amyloid β-protein involves the endocytic pathway. *Journal of Biological Chemistry*, 269:17386–17389, 1994.

[81] A. Lai, S. S. Sisodia, and I. S. Trowbridge. Characterization of Sorting Signals in the β-Amyloid Precursor Protein Cytoplasmic Domain. *Journal of Biological Chemistry*, 270:3565–3573, 1995.

[82] C. Haass, E. H. Koo, A. Mellon, A. Y. Hung, and D. J. Selkoe. Targeting of cell-surface β-amyloid precursor protein to lysosomes: Alternative processing into amyloid-bearing fragments. *Nature*, 357:500–503, 1992.

[83] T. Yamazaki, E. H. Koo, and D. J. Selkoe. Trafficking of cell-surface amyloid β-protein precursor: II. Endocytosis, recycling, and lysosomal targeting detected by immunolocalization. *Journal of Cell Science*, 109:999–1008, 1996.

[84] C. Nordstedt, G. L. Caporaso, J. Thyberg, S. E. Gandy, and P. Greengard. Identification of the Alzheimer β/A4 amyloid precursor protein in clathrin-coated vesicles purified from PC12 cells. *Journal of Biological Chemistry*, 268:608–612, 1993.

[85] R. Vassar, B. D. Bennett, S. Babu-Khan, S. Kahn, E. A. Mendiaz, P. Denis, D. B. Teplow, S. Ross, P. Amarante, R. Loeloff, Y. Luo, S. Fisher, J. Fuller, S. Edenson, J. Lile, M. A. Jarosinski, A. L. Biere, E. Curran, T. Burgess, J. C. Louis, F. Collins, J. Treanor, G. Rogers, and M. Citron. β-Secretase cleavage of Alzheimer's amyloid precursor protein by the transmembrane aspartic protease BACE. *Science*, 286:735–741, 1999.

[86] X. Meckler and F. Checler. Presenilin 1 and presenilin 2 target γ-secretase complexes to distinct cellular compartments. *Journal of Biological Chemistry*, 291:12821–12837, 2016.

[87] P. Paroutis, N. Touret, and S. Grinstein. The pH of the secretory pathway: Measurement, determinants, and regulation. *Physiology*, 19:207–215, 2004.

[88] Y. B. Hu, E. B. Dammer, R. J. Ren, and G. Wang. The endosomal-lysosomal system: From acidification and cargo sorting to neurodegeneration. *Translational Neurodegeneration*, 4:1–10, 2015.

[89] H. Shimizu, A. Tosaki, K. Kaneko, T. Hisano, T. Sakurai, and N. Nukina. Crystal Structure of an Active Form of BACE1, an Enzyme Responsible for Amyloid β Protein Production. *Molecular and Cellular Biology*, 28:3663–3671, 2008.

[90] F. Grüninger-Leitch, D. Schlatter, E. Küng, P. Nelböck, and H. Döbeli. Substrate and inhibitor profile of BACE (β-secretase) and comparison with other mammalian aspartic proteases. *Journal of Biological Chemistry*, 277:4687–4693, 2002.

[91] V. Y. Hook, T. Toneff, W. Aaron, S. Yasothornsrikul, R. Bundey, and T. Reisine. β-amyloid peptide in regulated secretory vesicles of chromaffin cells: Evidence for multiple cysteine proteolytic activities in distinct pathways for β-secretase activity in chromaffin vesicles. *Journal of Neurochemistry*, 81: 237–256, 2002.

[92] C. McLendon, T. Xin, C. Ziani-Cherif, M. P. Murphy, K. A. Findlay, P. A. Lewis, I. Pinnix, K. Sambamurti, R. Wang, A. Fauq, and T. E. Golde. Cell-free assays for γ-secretase activity. *The FASEB Journal*, 14:2383–2386, 2000.

[93] K. Ohta, A. Mizuno, S. Li, M. Itoh, M. Ueda, E. Ohta, Y. Hida, M. xing Wang, M. Furoi, Y. Tsuzuki, M. Sobajima, Y. Bohmoto, T. Fukushima, M. Kobori, T. Inuzuka, and T. Nakagawa. Endoplasmic reticulum stress enhances γ-secretase activity. *Biochemical and Biophysical Research Communications*, 416:362–366, 2011.

[94] B. Zhu, L. L. Jiang, T. Huang, Y. Zhao, T. Liu, Y. Zhong, X. Li, A. Campos, K. Pomeroy, E. Masliah, D. Zhang, and H. Xu. ER-associated degradation regulates Alzheimer's amyloid pathology and memory function by modulating γ-secretase activity. *Nature Communications*, 8:1–14, 2017.

[95] L. Zheng, A. Cedazo-Minguez, M. Hallbeck, F. Jerhammar, J. Marcusson, and A. Terman. Intracellular distribution of amyloid beta peptide and its relationship to the lysosomal system. *Translational Neurodegeneration*, 1:1–7, 2012.

[96] Y. Matsunaga, N. Saito, A. Fujii, J. Yokotani, T. Takakura, T. Nishimura, H. Esaki, and T. Yamada. A pH-dependent conformational transition of Aβ peptide and physicochemical properties of the conformers in the glial cell. *Biochemical Journal*, 361:547–556, 2002.

[97] J. Khandogin and C. L. Brooks. Linking folding with aggregation in Alzheimer's β-amyloid peptides. *Proceedings of the National Academy of Sciences of the United States of America*, 104:16880–16885, 2007.

[98] A. J. Beel, C. K. Mobley, H. J. Kim, F. Tian, A. Hadziselimovic, B. Jap, J. H. Prestegard, and C. R. Sanders. Structural Studies of the Transmembrane C-Terminal Domain of the Amyloid Precursor Protein (APP): Does APP Function as a Cholesterol Sensor? *Biochemistry*, 47:9428–9446, 2008.

[99] T. Tomita and T. Iwatsubo. Structural biology of presenilins and signal peptide peptidases. *Journal of Biological Chemistry*, 288:14673–14680, 2013.

[100] M. M. Javadpour, M. Eilers, M. Groesbeek, and S. O. Smith. Helix packing in polytopic membrane proteins: Role of glycine in transmembrane helix association. *Biophysical Journal*, 77:1609–1618, 1999.

[101] S. Kim, T.-J. Jeon, A. Oberai, D. Yang, J. J. Schmidt, and J. U. Bowie. Transmembrane glycine zippers: Physiological and pathological roles in membrane proteins. *Proceedings of the National Academy of Sciences*, 102:14278–14283, 2005.

[102] A. Panahi, A. Bandara, G. A. Pantelopulos, L. Dominguez, and J. E. Straub. Specific Binding of Cholesterol to C99 Domain of Amyloid Precursor Protein Depends Critically on Charge State of Protein. *Journal of Physical Chemistry Letters*, 7:3535–3541, 2016.

[103] N. Pierrot, D. Tyteca, L. D'auria, I. Dewachter, P. Gailly, A. Hendrickx, B. Tasiaux, L. E. Haylani, N. Muls, F. N'Kuli, A. Laquerrière, J. B. Demoulin, D. Campion, J. P. Brion, P. J. Courtoy, P. Kienlen-Campard, and J. N. Octave. Amyloid precursor protein controls cholesterol turnover needed for neuronal activity. *EMBO Molecular Medicine*, 5:608–625, 2013.

[104] A. J. Beel, M. Sakakura, P. J. Barrett, and C. R. Sanders. Direct binding of cholesterol to the amyloid precursor protein: An important interaction in lipid-Alzheimer's disease relationships? *Biochimica et Biophysica Acta - Molecular and Cell Biology of Lipids*, 1801:975–982, 2010.

[105] C.-D. Li, Q. Xu, R.-X. Gu, J. Qu, and D.-Q. Wei. The dynamic binding of cholesterol to the multiple sites of C99: as revealed by coarse-grained and all-atom simulations. *Phys. Chem. Chem. Phys.*, 19:3845–3856, 2017.

[106] S. M. Anderson, B. K. Mueller, E. J. Lange, and A. Senes. Combination of Cα–H Hydrogen Bonds and van der Waals Packing Modulates the Stability of GxxxG-Mediated Dimers in Membranes. *Journal of the American Chemical Society*, 139:15774–15783, 2017.

[107] N. Miyashita, J. E. Straub, D. Thirumalai, and Y. Sugita. Transmembrane structures of amyloid precursor protein dimer predicted by replica-exchange molecular dynamics simulations. *Journal of the American Chemical Society*, 131:3438–3439, 2009.

[108] O. Pester, P. J. Barrett, D. Hornburg, P. Hornburg, R. Pröbstle, S. Widmaier, C. Kutzner, M. Dürrbaum, A. Kapurniotu, C. R. Sanders, C. Scharnagl, and D. Langosch. The backbone dynamics of the amyloid precursor protein transmembrane helix provides a rationale for the sequential cleavage mechanism of gamma-secretase. *Journal of the American Chemical Society*, 135: 1317–1329, 2013.

[109] Z. Cao, J. M. Hutchison, C. R. Sanders, and J. U. Bowie. Backbone Hydrogen Bond Strengths Can Vary Widely in Transmembrane Helices. *Journal of the American Chemical Society*, 139:10742–10749, 2017.

[110] O. Holmes, S. Paturi, W. Ye, M. S. Wolfe, and D. J. Selkoe. Effects of Membrane Lipids on the Activity and Processivity of Purified γ-Secretase. *Biochemistry*, 51:3565–3575, 2012.

[111] E. Winkler, F. Kamp, J. Scheuring, A. Ebke, A. Fukumori, and H. Steiner. Generation of Alzheimer disease-associated amyloid beta 42/43 peptide by gamma-secretase can be inhibited directly by modulation of membrane thickness. *Journal of Biological Chemistry*, 287:21326–21334, 2012.

[112] L. Dominguez, S. C. Meredith, J. E. Straub, and D. Thirumalai. Transmembrane fragment structures of amyloid precursor protein depend on membrane surface curvature. *Journal of the American Chemical Society*, 136:854–857, 2014.

[113] L. Dominguez, L. Foster, S. C. Meredith, J. E. Straub, and D. Thirumalai. Structural heterogeneity in transmembrane Amyloid Precursor Protein homodimer is a consequence of environmental selection. *Journal of the American Chemical Society*, 136:9619–9626, 2014.

[114] L. Dominguez, L. Foster, J. E. Straub, and D. Thirumalai. Impact of membrane lipid composition on the structure and stability of the transmembrane domain of amyloid precursor protein. *Proceedings of the National Academy of Sciences*, 113:E5281–E5287, 2016.

[115] S. Viswanath, L. Dominguez, L. S. Foster, J. E. Straub, and R. Elber. Extension of a protein docking algorithm to membranes and applications to amyloid precursor protein dimerization. *Proteins: Structure, Function, and Bioinformatics*, 83:2170–2185, 2015.

[116] M. Audagnotto, T. Lemmin, A. Barducci, and M. Dal Peraro. Effect of the Synaptic Plasma Membrane on the Stability of the Amyloid Precursor Protein Homodimer. *The Journal of Physical Chemistry Letters*, 7:3572–3578, 2016.

[117] S. Weggen and D. Beher. Molecular consequences of amyloid precursor protein and presenilin mutations causing autosomal-dominant Alzheimer's disease. *Alzheimer's research and therapy*, 4:9, 2012.

[118] Y. Yan, T. H. Xu, K. G. Harikumar, L. J. Miller, K. Melcher, and H. E. Xu. Dimerization of the transmembrane domain of amyloid precursor protein is determined by residues around the γ-secretase cleavage sites. *Journal of Biological Chemistry*, 292:15826–15837, 2017.

[119] M. Dimitrov, J.-R. Alattia, T. Lemmin, R. Lehal, A. Fligier, J. Houacine, I. Hussain, F. Radtke, M. Dal Peraro, D. Beher, and P. C. Fraering. Alzheimer's disease mutations in APP but not γ-secretase modulators affect epsilon-cleavage-dependent AICD production. *Nature Communications*, 4: 2246, 2013.

[120] T. L. Kukar, T. B. Ladd, P. Robertson, S. A. Pintchovski, B. Moore, M. A. Bann, Z. Ren, K. Jansen-West, K. Malphrus, S. Eggert, H. Maruyama, B. A. Cottrell, P. Das, G. S. Basi, E. H. Koo, and T. E. Golde. Lysine 624 of the Amyloid Precursor Protein (APP) Is a Critical Determinant of Amyloid β Peptide Length. *Journal of Biological Chemistry*, 286:39804–39812, 2011.

[121] J. H. Goo and W. J. Park. Elucidation of the Interactions between C99, Presenilin, and Nicastrin by the Split-Ubiquitin Assay. *DNA and Cell Biology*, 23:59–65, 2004.

[122] Y. Tian, B. Bassit, D. Chau, and Y. M. Li. An APP inhibitory domain containing the Flemish mutation residue modulates γ-secretase activity for Aβ production. *Nature Structural and Molecular Biology*, 17:151–158, 2010.

[123] G. A. Pantelopulos, A. Panahi, and J. E. Straub. Impact of Cholesterol Concentration and Lipid Phase on Structure and Fluctuation of Amyloid Precursor Protein. *Journal of Physical Chemistry B*, 124:10173–10185, 2020.

[124] M. Citron, T. Oltersdorf, C. Haass, L. McConlogue, a. Y. Hung, P. Seubert, C. Vigo-Pelfrey, I. Lieberburg, and D. J. Selkoe. Mutation of the beta-amyloid precursor protein in familial Alzheimer's disease increases beta-protein production. *Nature*, 360:672–674, 1992.

[125] D. Kaden, A. Harmeier, C. Weise, L. M. Munter, V. Althoff, B. R. Rost, P. W. Hildebrand, D. Schmitz, M. Schaefer, R. Lurz, S. Skodda, R. Yamamoto, S. Arlt, U. Finckh, and G. Multhaup. Novel APP/Aβ mutation K16N produces highly toxic heteromeric Aβ oligomers. *EMBO Molecular Medicine*, 4: 647–659, 2012.

[126] L. Hendriks, C. M. van Duijn, P. Cras, M. Cruts, W. Van Hul, F. van Harskamp, A. Warren, M. G. McInnis, S. E. Antonarakis, J.-J. Martin, A. Hofman, and C. Van Broeckhoven. Presenile dementia and cerebral haemorrhage linked to a mutation at codon 692 of the β–amyloid precursor protein gene. *Nature Genetics*, 1:218–221, 1992.

[127] E. Levy, M. Carman, I. Fernandez-Madrid, M. Power, I. Lieberburg, S. van Duinen, G. Bots, W. Luyendijk, and B. Frangione. Mutation of the Alzheimer's disease amyloid gene in hereditary cerebral hemorrhage, Dutch type. *Science*, 248:1124–1126, 1990.

[128] O. Bugiani, A. Padovani, M. Magoni, G. Andora, M. Sgarzi, M. Savoiardo, A. Bizzi, G. Giaccone, G. Rossi, and F. Tagliavini. An Italian type of HCHWA. *Neurobiol Aging*, 19:S238, 1998.

[129] C. Nilsberth, A. Westlind-Danielsson, C. B. Eckman, M. M. Condron, K. Axelman, C. Forsell, C. Stenh, J. Luthman, D. B. Teplow, S. G. Younkin, J. Näslund, and L. Lannfelt. The 'Arctic' APP mutation (E693G) causes Alzheimer's disease by enhanced Aβ protofibril formation. *Nature Neuroscience*, 4:887–893, 2001.

[130] T. Tomiyama, T. Nagata, H. Shimada, R. Teraoka, A. Fukushima, H. Kanemitsu, H. Takuma, R. Kuwano, M. Imagawa, S. Ataka, Y. Wada, E. Yoshioka, T. Nishizaki, Y. Watanabe, and H. Mori. A new amyloid beta variant favoring oligomerization in Alzheimer's-type dementia. *Annals of Neurology*, 63: 377–387, 2008.

[131] T. J. Grabowski, H. S. Cho, J. P. G. Vonsattel, G. William Rebeck, and S. M. Greenberg. Novel amyloid precursor protein mutation in an Iowa family with dementia and severe cerebral amyloid angiopathy. *Annals of Neurology*, 49: 697–705, 2001.

[132] L. Zhou, N. Brouwers, I. Benilova, A. Vandersteen, M. Mercken, K. Van Laere, P. Van Damme, D. Demedts, F. Van Leuven, K. Sleegers, K. Broersen, C. Van Broeckhoven, R. Vandenberghe, and B. De Strooper. Amyloid precursor protein mutation E682K at the alternative β-secretase cleavage β'-site increases Aβ generation. *EMBO Molecular Medicine*, 3:291–302, 2011.

[133] M. Oishi, A. C. Nairn, A. J. Czernik, G. S. Lim, T. Isohara, S. E. Gandy, P. Greengard, and T. Suzuki. The cytoplasmic domain of Alzheimer's amyloid precursor protein is phosphorylated at Thr654, Ser655, and Thr668 in adult rat brain and cultured cells. *Molecular Medicine*, 3:111–23, 1997.

[134] Y. Wakutani. Novel amyloid precursor protein gene missense mutation (D678N) in probable familial Alzheimer's disease. *Journal of Neurology, Neurosurgery and Psychiatry*, 75:1039–1042, 2004.

[135] G. Di Fede, M. Catania, M. Morbin, G. Rossi, S. Suardi, G. Mazzoleni, M. Merlin, A. R. Giovagnoli, S. Prioni, A. Erbetta, C. Falcone, M. Gobbi, L. Colombo, A. Bastone, M. Beeg, C. Manzoni, B. Francescucci, A. Spagnoli, L. Cantu, E. Del Favero, E. Levy, M. Salmona, and F. Tagliavini. A Recessive Mutation in the APP Gene with Dominant-Negative Effect on Amyloidogenesis. *Science*, 323:1473–1477, 2009.

[136] C. J. Maynard, A. I. Bush, C. L. Masters, R. Cappai, and Q.-X. Li. Metals and amyloid-beta in Alzheimer's disease. *International journal of experimental pathology*, 86:147–159, 2005.

[137] G. M. Shaked, M. P. Kummer, D. C. Lu, V. Galvan, D. E. Bredesen, and E. H. Koo. Abeta induces cell death by direct interaction with its cognate

extracellular domain on APP (APP 597-624). *FASEB journal : official publication of the Federation of American Societies for Experimental Biology*, 20:1254–1246, 2006.

[138] N. Zambrano, P. Bruni, G. Minopoli, R. Mosca, D. Molino, C. Russo, G. Schettini, M. Sudol, and T. Russo. The β-Amyloid Precursor Protein APP is Tyrosine-Phosphorylated in Cells Expressing a Constitutively Active Form of the Abl Protoncogene. *The Journal of Biological Chemistry*, 276:19787–19792, 2001.

[139] S. I. Vieira, S. Rebelo, S. C. Domingues, E. F. Cruz e Silva, and O. A. B. Cruz e Silva. S655 phosphorylation enhances APP secretory traffic. *Molecular and Cellular Biochemistry*, 328:145–154, 2009.

[140] C. Feyt, N. Pierrot, B. Tasiaux, J. Van Hees, P. Kienlen-Campard, P. J. Courtoy, and J. N. Octave. Phosphorylation of APP695 at Thr668 decreases gamma-cleavage and extracellular Abeta. *Biochemical and Biophysical Research Communications*, 357:1004–1010, 2007.

[141] E. T. Poulsen, F. Iannuzzi, H. F. Rasmussen, T. J. Maier, J. J. Enghild, A. L. Jørgensen, and C. Matrone. An Aberrant Phosphorylation of Amyloid Precursor Protein Tyrosine Regulates Its Trafficking and the Binding to the Clathrin Endocytic Complex in Neural Stem Cells of Alzheimer's Disease Patients. *Frontiers in Molecular Neuroscience*, 10:59, 2017.

[142] Y. Sano, T. Nakaya, S. Pedrini, S. Takeda, K. Iijima-Ando, K. Iijima, P. M. Mathews, S. Itohara, S. Gandy, and T. Suzuki. Physiological Mouse Brain Aβ Levels Are Not Related to the Phosphorylation State of Threonine-668 of Alzheimer's APP. *PLoS ONE*, 1:e51, 2006.

[143] T. Suzuki, M. Oishi, D. R. Marshak, A. J. Czernik, A. C. Nairn, and P. Greengard. Cell Cycle-Dependent Regulation of the Phosphorylation and Metabolism of the Alzheimer Amyloid Precursor Protein. *The EMBO Journal*, 13:1114–1122, 1994.

[144] T. A. Ramelot, L. N. Gentile, and L. K. Nicholson. Transient structure of the amyloid precursor protein cytoplasmic tail indicates preordering of structure for binding to cytosolic factors. *Biochemistry*, 39:2714–2725, 2000.

[145] U. Giambarella, T. Yamatsuji, T. Okamoto, T. Matsui, T. Ikezu, Y. Murayama, M. A. Levine, A. Katz, N. Gautam, and I. Nishimoto. G protein beta gamma complex-mediated apoptosis by familial Alzheimer's disease mutant of APP. *EMBO Journal*, 16:4897–4907, 1997.

[146] T. Russo, R. Faraonio, G. Minopoli, P. De Candia, S. De Renzis, and N. Zambrano. Fe65 and the protein network centered around the cytosolic domain of the Alzheimer's beta-amyloid precursor protein. *FEBS Letters*, 434:1–7, 1998.

[147] Z. Zhang, C. H. Lee, V. Mandiyan, J. P. Borg, B. Margolis, J. Schlessinger, and J. Kuriyan. Sequence-specific recognition of the internalization motif of the Alzheimer's amyloid precursor protein by the X11 PTB domain. *EMBO Journal*, 16:6141–6150, 1997.

[148] L. Parisiadou and S. Efthimiopoulos. Expression of mDab1 promotes the stability and processing of amyloid precursor protein and this effect is counteracted by X11alpha. *Neurobiology of Aging*, 28:377–388, 2007.

[149] M. H. Scheinfeld, R. Roncarati, P. Vito, P. A. Lopez, M. Abdallah, and L. D'Adamio. Jun NH2-terminal kinase (JNK) interacting protein 1 (JIP1) binds the cytoplasmic domain of the Alzheimer's β-amyloid precursor protein (APP). *Journal of Biological Chemistry*, 277:3767–3775, 2002.

[150] D. C. Lu, S. Rabizadeh, S. Chandra, R. F. Shayya, L. M. Ellerby, X. Ye, G. S. Salvesen, E. H. Koo, and D. E. Bredesen. A second cytotoxic proteolytic peptide derived from amyloid β-protein precursor. *Nature Medicine*, 6:397–404, 2000.

[151] D. C. Lu, S. Soriano, D. E. Bredesen, and E. H. Koo. Caspase cleavage of the amyloid precursor protein modulates amyloid β-protein toxicity. *Journal of Neurochemistry*, 87:733–741, 2003.

[152] S. Staubach and F. G. Hanisch. Lipid rafts: Signaling and sorting platforms of cells and their roles in cancer. *Expert Review of Proteomics*, 8:263–277, 2011.

[153] M. Edidin. Lipid microdomains in cell surface membranes. *Current Opinion in Structural Biology*, 7:528–532, 1997.

[154] C. Eggeling, C. Ringemann, R. Medda, G. Schwarzmann, K. Sandhoff, S. Polyakova, V. N. Belov, B. Hein, C. von Middendorff, A. Schönle, and S. W. Hell. Direct observation of the nanoscale dynamics of membrane lipids in a living cell. *Nature*, 457:1159–1162, 2009.

[155] A. Toulmay and W. A. Prinz. Direct imaging reveals stable, micrometer-scale lipid domains that segregate proteins in live cells. *Journal of Cell Biology*, 202:35–44, 2013.

[156] R. Koynova and M. Caffrey. Phases and phase transitions of the phosphatidylcholines. *Biochimica et Biophysica Acta (BBA) - Reviews on Biomembranes*, 1376:91–145, 1998.

[157] R. Ehehalt, P. Keller, C. Haass, C. Thiele, and K. Simons. Amyloidogenic processing of the Alzheimer β-amyloid precursor protein depends on lipid rafts. *Journal of Cell Biology*, 160:113–123, 2003.

[158] J. M. Cordy, J. M. Cordy, N. M. Hooper, and A. J. Turner. The involvement of lipid rafts in Alzheimer's disease (Review). *Molecular Membrane Biology*, 23:111–122, 2006.

[159] D. R. Taylor and N. M. Hooper. Role of lipid rafts in the processing of the pathogenic prion and Alzheimer's amyloid-β proteins. *Seminars in Cell & Developmental Biology*, 18:638–648, 2007.

[160] J.-Y. Hur, H. Welander, H. Behbahani, M. Aoki, J. Frånberg, B. Winblad, S. Frykman, and L. O. Tjernberg. Active γ-secretase is localized to detergent-resistant membranes in human brain. *FEBS Journal*, 275:1174–1187, 2008.

[161] K. S. Vetrivel, X. Meckler, Y. Chen, P. D. Nguyen, N. G. Seidah, R. Vassar, P. C. Wong, M. Fukata, M. Z. Kounnas, and G. Thinakaran. Alzheimer disease Aβ production in the absence of S-palmitoylation-dependent targeting of BACE1 to lipid rafts. *Journal of Biological Chemistry*, 284:3793–3803, 2009.

[162] J. V. Rushworth and N. M. Hooper. Lipid Rafts: Linking Alzheimer's Amyloid-β Production, Aggregation, and Toxicity at Neuronal Membranes. *International Journal of Alzheimer's Disease*, 2011:1–14, 2011.

[163] J. H. Lorent, B. Diaz-Rohrer, X. Lin, K. Spring, A. A. Gorfe, K. R. Levental, and I. Levental. Structural determinants and functional consequences of protein affinity for membrane rafts. *Nature Communications*, 8:1219, 2017.

[164] R. Bhattacharyya, C. Barren, and D. M. Kovacs. Palmitoylation of Amyloid Precursor Protein Regulates Amyloidogenic Processing in Lipid Rafts. *Journal of Neuroscience*, 33:11169–11183, 2013.

[165] R. Bhattacharyya, R. H. Fenn, C. Barren, R. E. Tanzi, and D. M. Kovacs. Palmitoylated APP forms dimers, cleaved by BACE1. *PLoS ONE*, 11:1–25, 2016.

[166] F. M. Brodsky, C.-y. Chen, C. Knuehl, M. C. Towler, and D. E. Wakeham. Biological Basket Weaving: Formation and Function of Clathrin-Coated Vesicles. *Annual Review of Cell and Developmental Biology*, 17:517–568, 2001.

[167] V. Haucke and M. M. Kozlov. Membrane remodeling in clathrin-mediated endocytosis. *Journal of Cell Science*, 131:1–10, 2018.

[168] R. G. Parton, V. Tillu, K.-A. McMahon, and B. M. Collins. Key phases in the formation of caveolae. *Current Opinion in Cell Biology*, 71:7–14, 2021.

[169] J. Lee, C. Retamal, L. Cuitiño, A. Caruano-Yzermans, J. E. Shin, P. Van Kerkhof, M. P. Marzolo, and G. Bu. Adaptor protein sorting nexin 17 regulates amyloid precursor protein trafficking and processing in the early endosomes. *Journal of Biological Chemistry*, 283:11501–11508, 2008.

[170] P. V. Burgos, G. A. Mardones, A. L. Rojas, L. L. DaSilva, Y. Prabhu, J. H. Hurley, and J. S. Bonifacino. Sorting of the Alzheimer's Disease Amyloid Precursor Protein Mediated by the AP-4 Complex. *Developmental Cell*, 18: 425–436, 2010.

[171] C. Hattori, M. Asai, H. Onishi, N. Sasagawa, Y. Hashimoto, T. C. Saido, K. Maruyama, S. Mizutani, and S. Ishiura. BACE1 interacts with lipid raft proteins. *Journal of Neuroscience Research*, 84:912–917, 2006.

[172] M. R. Vist and J. H. Davis. Phase equilibria of cholesterol/dipalmitoylphosphatidylcholine mixtures: 2H nuclear magnetic resonance and differential scanning calorimetry. *Biochemistry*, 29:451–464, 1990.

[173] J. Hjort Ipsen, G. Karlström, O. G. Mourtisen, H. Wennerström, and M. J. Zuckermann. Phase equilibria in the phosphatidylcholine-cholesterol system. *BBA - Biomembranes*, 905:162–172, 1987.

[174] Y. W. Hsueh, M. Zuckermann, and J. Thewalt. Phase diagram determination for phospholipid/sterol membranes using deuterium NMR. *Concepts in Magnetic Resonance Part A: Bridging Education and Research*, 26:35–46, 2005.

[175] A. Ivankin, I. Kuzmenko, and D. Gidalevitz. Cholesterol-phospholipid interactions: New insights from surface x-ray scattering data. *Physical Review Letters*, 104:1–4, 2010.

[176] A. Keyvanloo, M. Shaghaghi, M. J. Zuckermann, and J. L. Thewalt. The Phase Behavior and Organization of Sphingomyelin/Cholesterol Membranes: A Deuterium NMR Study. *Biophysical Journal*, 114:1344–1356, 2018.

[177] L. Miao, M. Nielsen, J. Thewalt, J. H. Ipsen, M. Bloom, M. J. Zuckermann, and O. G. Mouritsen. From Lanosterol to Cholesterol: Structural Evolution and Differential Effects on Lipid Bilayers. *Biophysical Journal*, 82:1429–1444, 2002.

[178] A. J. Sodt, M. L. Sandar, K. Gawrisch, R. W. Pastor, and E. Lyman. The Molecular Structure of the Liquid-Ordered Phase of Lipid Bilayers. *Journal of the American Chemical Society*, 136:725–732, 2014.

[179] M. Javanainen, H. Martinez-Seara, and I. Vattulainen. Nanoscale Membrane Domain Formation Driven by Cholesterol. *Scientific Reports*, 7:1143, 2017.

[180] N. Bezlyepkina, R. Gracià, P. Shchelokovskyy, R. Lipowsky, and R. Dimova. Phase Diagram and Tie-Line Determination for the Ternary Mixture DOPC /eSM/Cholesterol. *Biophysical Journal*, 104:1456–1464, 2013.

[181] J. V. Bleecker, P. A. Cox, R. N. Foster, J. P. Litz, M. C. Blosser, D. G. Castner, and S. L. Keller. Thickness Mismatch of Coexisting Liquid Phases in Noncanonical Lipid Bilayers. *Journal of Physical Chemistry B*, 120:2761–2770, 2016.

[182] E. R. Farkas and W. W. Webb. Precise and millidegree stable temperature control for fluorescence imaging: Application to phase transitions in lipid membranes. *Review of Scientific Instruments*, 81:093704, 2010.

[183] F. A. Heberle, J. Wu, S. L. Goh, R. S. Petruzielo, and G. W. Feigenson. Comparison of three ternary lipid bilayer mixtures: FRET and ESR reveal nanodomains. *Biophysical Journal*, 99:3309–3318, 2010.

[184] A. R. Honerkamp-Smith, B. B. Machta, and S. L. Keller. Experimental Observations of Dynamic Critical Phenomena in a Lipid Membrane. *Physical Review Letters*, 108:265702, 2012.

[185] A. R. Honerkamp-Smith, P. Cicuta, M. D. Collins, S. L. Veatch, M. den Nijs, M. Schick, and S. L. Keller. Line Tensions, Correlation Lengths, and Critical Exponents in Lipid Membranes Near Critical Points. *Biophysical Journal*, 95:236–246, 2008.

[186] M. H. Jensen, E. J. Morris, and A. C. Simonsen. Domain shapes, coarsening, and random patterns in ternary membranes. *Langmuir*, 23:8135–8141, 2007.

[187] T. M. Konyakhina and G. W. Feigenson. Phase diagram of a polyunsaturated lipid mixture: Brain sphingomyelin/1-stearoyl-2-docosahexaenoyl-sn-glycero-3-phosphocholine/cholesterol. *Biochimica et Biophysica Acta (BBA) - Biomembranes*, 1858:153–161, 2016.

[188] T. K. M. Nyholm, D. Lindroos, B. Westerlund, and J. P. Slotte. Construction of a DOPC/PSM/Cholesterol Phase Diagram Based on the Fluorescence Properties of trans-Parinaric Acid. *Langmuir*, 27:8339–8350, 2011.

[189] A. Radhakrishnan. Phase Separations in Binary and Ternary Cholesterol-Phospholipid Mixtures. *Biophysical Journal*, 98:L41–L43, 2010.

[190] B. M. Stott, M. P. Vu, C. O. McLemore, M. S. Lund, E. Gibbons, T. J. Brueseke, H. A. Wilson-Ashworth, and J. D. Bell. Use of fluorescence to determine the effects of cholesterol on lipid behavior in sphingomyelin liposomes and erythrocyte membranes. *Journal of Lipid Research*, 49:1202–1215, 2008.

[191] A. Tian, C. Johnson, W. Wang, and T. Baumgart. Line tension at fluid membrane domain boundaries measured by micropipette aspiration. *Physical Review Letters*, 98:208102, 2007.

[192] R. D. Usery, T. A. Enoki, S. P. Wickramasinghe, M. D. Weiner, W. C. Tsai, M. B. Kim, S. Wang, T. L. Torng, D. G. Ackerman, F. A. Heberle, J. Katsaras, and G. W. Feigenson. Line Tension Controls Liquid-Disordered + Liquid-Ordered Domain Size Transition in Lipid Bilayers. *Biophysical Journal*, 112:1431–1443, 2017.

[193] S. L. Veatch, P. Cicuta, P. Sengupta, A. Honerkamp-Smith, D. Holowka, and B. Baird. Critical fluctuations in plasma membrane vesicles. *ACS Chemical Biology*, 3:287–293, 2008.

[194] S. L. Veatch and S. L. Keller. Separation of Liquid Phases in Giant Vesicles of Ternary Mixtures of Phospholipids and Cholesterol. *Biophysical Journal*, 85:3074–3083, 2003.

[195] S. L. Veatch and S. L. Keller. Miscibility phase diagrams of giant vesicles containing sphingomyelin. *Physical Review Letters*, 94:3–6, 2005.

[196] S. L. Veatch and S. L. Keller. Seeing spots: Complex phase behavior in simple membranes. *Biochimica et Biophysica Acta - Molecular Cell Research*, 1746: 172–185, 2005.

[197] S. L. Veatch, K. Gawrisch, and S. L. Keller. Closed-Loop Miscibility Gap and Quantitative Tie-Lines in Ternary Membranes Containing Diphytanoyl PC. *Biophysical Journal*, 90:4428–4436, 2006.

[198] P. Heftberger, B. Kollmitzer, A. A. Rieder, H. Amenitsch, and G. Pabst. In situ determination of structure and fluctuations of coexisting fluid membrane domains. *Biophysical Journal*, 108:854–862, 2015.

[199] J. Pencer, T. Mills, V. Anghel, S. Krueger, R. M. Epand, and J. Katsaras. Detection of submicron-sized raft-like domains in membranes by small-angle neutron scattering. *European Physical Journal E*, 18:447–458, 2005.

[200] L. Toppozini, S. Meinhardt, C. L. Armstrong, Z. Yamani, N. Kučerka, F. Schmid, M. C. Rheinstädter, N. Kucerka, F. Schmid, and M. C. Rheinstaedter. Structure of Cholesterol in Lipid Rafts. *Physical Review Letters*, 113:228101, 2014.

[201] J. Zhao, J. Wu, F. A. Heberle, T. T. Mills, P. Klawitter, G. Huang, G. Costanza, and G. W. Feigenson. Phase studies of model biomembranes: Complex behavior of DSPC/DOPC/Cholesterol. *Biochimica et Biophysica Acta - Biomembranes*, 1768:2764–2776, 2007.

[202] R. Ziblat, L. Leiserowitz, and L. Addadi. Crystalline domain structure and cholesterol crystal nucleation in single hydrated DPPC: Cholesterol: POPC bilayers. *Journal of the American Chemical Society*, 132:9920–9927, 2010.

[203] S. D. Connell, G. Heath, P. D. Olmsted, and A. Kisil. Critical point fluctuations in supported lipid membranes. *Faraday discussions*, 161:91–111; discussion 113–50, 2013.

[204] N. K. Khadka, C. S. Ho, and J. Pan. Macroscopic and Nanoscopic Heterogeneous Structures in a Three-Component Lipid Bilayer Mixtures Determined by Atomic Force Microscopy. *Langmuir*, 31:12417–12425, 2015.

[205] J. H. Davis, J. J. Clair, and J. Juhasz. Phase equilibria in DOPC/DPPC-d62/cholesterol mixtures. *Biophysical Journal*, 96:521–539, 2009.

[206] S. L. Veatch, O. Soubias, S. L. Keller, and K. Gawrisch. Critical fluctuations in domain-forming lipid mixtures. *Proceedings of the National Academy of Sciences*, 104:17650–17655, 2007.

[207] H.-M. Wu, Y.-H. Lin, T.-C. Yen, and C.-L. Hsieh. Nanoscopic substructures of raft-mimetic liquid-ordered membrane domains revealed by high-speed single-particle tracking. *Scientific Reports*, 6:20542, 2016.

[208] J. Ando, M. Kinoshita, J. Cui, H. Yamakoshi, K. Dodo, K. Fujita, M. Murata, and M. Sodeoka. Sphingomyelin distribution in lipid rafts of artificial monolayer membranes visualized by Raman microscopy. *Proceedings of the National Academy of Sciences*, 112:4558–4563, 2015.

[209] J. Huang, J. T. Buboltz, and G. W. Feigenson. Maximum solubility of cholesterol in phosphatidylcholine and phosphatidylethanolamine bilayers. *Biochimica et Biophysica Acta - Biomembranes*, 1417:89–100, 1999.

[210] A. Parker, K. Miles, K. H. Cheng, and J. Huang. Lateral Distribution of Cholesterol in Dioleoylphosphatidylcholine Lipid Bilayers: Cholesterol-Phospholipid Interactions at High Cholesterol Limit. *Biophysical Journal*, 86:1532–1544, 2004.

[211] M. M. Stevens, A. R. Honerkamp-Smith, and S. L. Keller. Solubility limits of cholesterol, lanosterol, ergosterol, stigmasterol, and β-sitosterol in electroformed lipid vesicles. *Soft Matter*, 6:5882–5890, 2010.

[212] S. R. Wassall, M. R. Brzustowicz, S. R. Shaikh, V. Cherezov, M. Caffrey, and W. Stillwell. Order from disorder, corralling cholesterol with chaotic lipids: The role of polyunsaturated lipids in membrane raft formation. *Chemistry and Physics of Lipids*, 132:79–88, 2004.

[213] I. Solomonov, M. J. Weygand, K. Kjaer, H. Rapaport, and L. Leiserowitz. Trapping crystal nucleation of cholesterol monohydrate: Relevance to pathological crystallization. *Biophysical Journal*, 88:1809–1817, 2005.

[214] D. Borchman and M. C. Yappert. Lipids and the ocular lens. *Journal of Lipid Research*, 51:2473–2488, 2010.

[215] F. Schmid. Physical mechanisms of micro- and nanodomain formation in multicomponent lipid membranes. *Biochimica et Biophysica Acta (BBA) - Biomembranes*, 1859:509–528, 2017.

[216] D. Marsh. Cholesterol-induced fluid membrane domains: A compendium of lipid-raft ternary phase diagrams. *Biochimica et Biophysica Acta - Biomembranes*, 1788:2114–2123, 2009.

[217] P. Losada-Pérez, N. Mertens, B. de Medio-Vasconcelos, E. Slenders, J. Leys, M. Peeters, B. van Grinsven, J. Gruber, C. Glorieux, H. Pfeiffer, P. Wagner, and J. Thoen. Phase Transitions of Binary Lipid Mixtures: A Combined Study by Adiabatic Scanning Calorimetry and Quartz Crystal Microbalance with Dissipation Monitoring. *Advances in Condensed Matter Physics*, 2015: 1–14, 2015.

[218] H. Pfeiffer, G. Klose, K. Heremans, and C. Glorieux. Thermotropic phase behaviour of the pseudobinary mixtures of DPPC/C12E5 and DMPC/C12E5 determined by differential scanning calorimetry and ultrasonic velocimetry. *Chemistry and Physics of Lipids*, 139:54–67, 2006.

[219] H. Y. Sun, F. G. Wu, Z. H. Li, G. Deng, Y. Zhou, and Z. W. Yu. Phase behavior of a binary lipid system containing long- and short-chain phosphatidylcholines. *RSC Advances*, 7:5715–5724, 2017.

[220] F.-G. Wu, H.-Y. Sun, Y. Zhou, G. Deng, and Z.-W. Yu. Molecular-level pictures of the phase transitions of saturated and unsaturated phospholipid binary mixtures. *RSC Advances*, 5:726–733, 2015.

[221] J. H. Davis and M. L. Schmidt. Critical behaviour in DOPC/DPPC/cholesterol mixtures: Static 2H NMR line shapes near the critical point. *Biophysical Journal*, 106:1970–1978, 2014.

[222] A. R. Honerkamp-Smith, S. L. Veatch, and S. L. Keller. An introduction to critical points for biophysicists; observations of compositional heterogeneity in lipid membranes. *Biochimica et Biophysica Acta - Biomembranes*, 1788: 53–63, 2009.

[223] J. Risbo, M. M. Sperotto, and O. G. Mouritsen. Theory of phase equilibria and critical mixing points in binary lipid bilayers. *The Journal of Chemical Physics*, 103:3643–3656, 1995.

[224] Z. Zhang, M. M. Sperotto, M. J. Zuckermann, and O. G. Mouritsen. A microscopic model for lipid/protein bilayers with critical mixing. *BBA - Biomembranes*, 1147:154–160, 1993.

[225] O. Engberg, H. Nurmi, T. K. Nyholm, and J. P. Slotte. Effects of cholesterol and saturated sphingolipids on Acyl chain order in 1-palmitoyl-2-oleoyl- Sn -Glycero-3-phosphocholine bilayers-A comparative study with phase-selective fluorophores. *Langmuir*, 31:4255–4263, 2015.

[226] M. K. Ratajczak, E. Y. Chi, S. L. Frey, K. D. Cao, L. M. Luther, K. Y. C. Lee, J. Majewski, and K. Kjaer. Ordered nanoclusters in lipid-cholesterol membranes. *Physical Review Letters*, 103:1–4, 2009.

[227] R. Ziblat, L. Leiserowitz, and L. Addadi. Crystalline lipid domains: Characterization by X-ray diffraction and their relation to biology. *Angewandte Chemie - International Edition*, 50:3620–3629, 2011.

[228] A. Bandara, A. Panahi, G. A. Pantelopulos, and J. E. Straub. Exploring the structure and stability of cholesterol dimer formation in multicomponent lipid bilayers. *Journal of Computational Chemistry*, 38:1479–1488, 2017.

[229] M. R. Elkins, A. Bandara, G. A. Pantelopulos, J. E. Straub, and M. Hong. Direct Observation of Cholesterol Dimers and Tetramers in Lipid Bilayers. *The Journal of Physical Chemistry B*, 125:1825–1837, 2021.

[230] J. Dai, M. Alwarawrah, and J. Huang. Instability of Cholesterol Clusters in Lipid Bilayers and The Cholesterol's Umbrella Effect. *The Journal of Physical Chemistry B*, 114:840–848, 2010.

[231] V. A. Frolov, Y. A. Chizmadzhev, F. S. Cohen, and J. Zimmerberg. "Entropic traps" in the kinetics of phase separation in multicomponent membranes stabilize nanodomains. *Biophysical Journal*, 91:189–205, 2006.

[232] I. Basu and C. Mukhopadhyay. In silico phase separation in the presence of GM1 in ternary and quaternary lipid bilayers. *Phys. Chem. Chem. Phys.*, 17:17130–17139, 2015.

[233] M. Yanagisawa, M. Imai, T. Masui, S. Komura, and T. Ohta. Growth Dynamics of Domains in Ternary Fluid Vesicles. *Biophysical Journal*, 92:115–125, 2007.

[234] D. Saeki, T. Hamada, and K. Yoshikawa. Domain-growth kinetics in a cell-sized liposome. *Journal of the Physical Society of Japan*, 75:26–28, 2006.

[235] J. Grouleff, S. J. Irudayam, K. K. Skeby, and B. Schiøtt. The influence of cholesterol on membrane protein structure, function, and dynamics studied by molecular dynamics simulations. *Biochimica et Biophysica Acta - Biomembranes*, 1848:1783–1795, 2015.

[236] Y. Ma, S. K. Ghosh, D. A. Dilena, S. Bera, L. B. Lurio, A. N. Parikh, and S. K. Sinha. Cholesterol Partition and Condensing Effect in Phase-Separated Ternary Mixture Lipid Multilayers. *Biophysical Journal*, 110:1355–1366, 2016.

[237] M. Simons, P. Keller, B. De Strooper, K. Beyreuther, C. G. Dotti, and K. Simons. Cholesterol depletion inhibits the generation of beta-amyloid in hippocampal neurons. *Proceedings of the National Academy of Sciences*, 95: 6460–6464, 1998.

[238] L. M. Refolo, M. A. Pappolla, B. Malester, J. LaFrancois, T. Bryant-Thomas, R. Wang, G. Tint, K. Sambamurti, and K. Duff. Hypercholesterolemia Accelerates the Alzheimer's Amyloid Pathology in a Transgenic Mouse Model. *Neurobiology of Disease*, 7:321–331, 2000.

[239] L. Refolo, M. Pappolla, J. LaFrancois, B. Malester, S. Schmidt, T. Thomas-Bryant, G. Tint, R. Wang, M. Mercken, S. Petanceska, and K. Duff. A Cholesterol-Lowering Drug Reduces β-Amyloid Pathology in a Transgenic Mouse Model of Alzheimer's Disease. *Neurobiology of Disease*, 8:890–899, 2001.

[240] F.-S. Shie, L.-W. Jin, D. G. Cook, J. B. Leverenz, and R. C. LeBoeuf. Diet-induced hypercholesterolemia enhances brain Aβ accumulation in transgenic mice. *Neuroreport*, 13:455–459, 2002.

[241] L. Puglielli, R. E. Tanzi, and D. M. Kovacs. Alzheimer's disease: the cholesterol connection. *Nature Neuroscience*, 6:345–351, 2003.

[242] E. G. Zinser, T. Hartmann, and M. O. Grimm. Amyloid beta-protein and lipid metabolism. *Biochimica et Biophysica Acta - Biomembranes*, 1768: 1991–2001, 2007.

[243] J. Yan, Y. Xu, C. Zhu, L. Zhang, A. Wu, Y. Yang, Z. Xiong, C. Deng, X. F. Huang, M. A. Yenari, Y. G. Yang, W. Ying, and Q. Wang. Simvastatin prevents dopaminergic neurodegeneration in experimental parkinsonian models: The association with anti-inflammatory responses. *PLoS ONE*, 6:e20945, 2011.

[244] G. W. Wood, L. Ling, W. Muller, and G. Eckert. Cholesterol as a causative agent in Alzheimer disease: a debatable hypothesis. *J Neurochem*, 129: 559–572, 2014.

[245] C. Marquer, V. Devauges, J.-C. Cossec, G. Liot, S. Lécart, F. Saudou, C. Duyckaerts, S. Lévêque-Fort, and M.-C. Potier. Local cholesterol increase triggers amyloid precursor protein-Bace1 clustering in lipid rafts and rapid endocytosis. *The FASEB Journal*, 25:1295–1305, 2011.

[246] E. S. Feldblum and I. T. Arkin. Strength of a bifurcated H bond. *Proceedings of the National Academy of Sciences*, 111:4085–4090, 2014.

[247] Q. Gao, G. Wu, and K. W. C. Lai. Cholesterol Modulates the Formation of the Aβ Ion Channel in Lipid Bilayers. *Biochemistry*, 59:992–998, 2020.

[248] N. Kandel, J. O. Matos, and S. A. Tatulian. Structure of amyloid β 25–35 in lipid environment and cholesterol-dependent membrane pore formation. *Scientific Reports*, 9:1–12, 2019.

[249] J. Fantini, N. Yahi, and N. Garmy. Cholesterol accelerates the binding of Alzheimer's β-amyloid peptide to ganglioside GM1 through a universal hydrogen-bond-dependent sterol tuning of glycolipid conformation. *Frontiers in Physiology*, 4:1–10, 2013.

[250] J. A. Hamilton. Fast flip-flop of cholesterol and fatty acids in membranes: implications for membrane transport proteins. *Current opinion in lipidology*, 14:263–271, 2003.

[251] W. F. D. Bennett, J. L. MacCallum, M. J. Hinner, S. J. Marrink, and D. P. Tieleman. Molecular view of cholesterol flip-flop and chemical potential in different membrane environments. *Journal of the American Chemical Society*, 131:12714–12720, 2009.

[252] M. N. Melo, H. I. Ingólfsson, and S. J. Marrink. Parameters for Martini sterols and hopanoids based on a virtual-site description. *The Journal of Chemical Physics*, 143:243152, 2015.

[253] R. X. Gu, S. Baoukina, and D. P. Tieleman. Cholesterol Flip-Flop in Heterogeneous Membranes. *Journal of Chemical Theory and Computation*, 15: 2064–2070, 2019.

[254] Y. Oh, E. S. Song, and B. J. Sung. The effects of the lipid type on the spatial arrangement and dynamics of cholesterol in binary component lipid membranes. *The Journal of Chemical Physics*, 154:135101, 2021.

[255] M. Camesasca, M. Kaufman, and I. Manas-Zloczower. Quantifying Fluid Mixing with the Shannon Entropy. *Macromolecular Theory and Simulations*, 15: 595–607, 2006.

[256] G. B. Brandani, M. Schor, C. E. MacPhee, H. Grubmüller, U. Zachariae, and D. Marenduzzo. Quantifying Disorder through Conditional Entropy: An Application to Fluid Mixing. *PLoS ONE*, 8:e65617, 2013.

[257] K. Kim, S. Q. Choi, Z. A. Zell, T. M. Squires, and J. A. Zasadzinski. Effect of cholesterol nanodomains on monolayer morphology and dynamics. *Proceedings of the National Academy of Sciences*, 110:E3054–E3060, 2013.

[258] P. J. Quinn and C. Wolf. The liquid-ordered phase in membranes. *Biochimica et Biophysica Acta - Biomembranes*, 1788:33–46, 2009.

[259] B. I. Halperin and D. R. Nelson. Theory of Two-Dimensional melting. *Physical Review Letters*, 41:121–124, 1978.

[260] E. P. Bernard and W. Krauth. Two-Step Melting in Two Dimensions: First-Order Liquid-Hexatic Transition. *Physical Review Letters*, 107:155704, 2011.

[261] R. Koynova and B. Tenchov. Lipids: Phase Transitions. In *Wiley Encyclopedia of Chemical Biology*. John Wiley & Sons, Inc., Hoboken, NJ, USA, 2008.

[262] L. Onsager. The Effects Of Shape On The Interaction Of Colloidal Particles. *Annals of the New York Academy of Sciences*, 51:627–659, 1949.

[263] T. J. Piggot, J. R. Allison, R. B. Sessions, and J. W. Essex. On the Calculation of Acyl Chain Order Parameters from Lipid Simulations. *Journal of Chemical Theory and Computation*, 13:5683–5696, 2017.

[264] J. Seelig. Deuterium magnetic resonance: theory and application to lipid membranes. *Quarterly Reviews of Biophysics*, 10:353–418, 1977.

[265] M. Hong, K. Schmidt-Rohr, and A. Pines. NMR Measurement of Signs and Magnitudes of C-H Dipolar Couplings in Lecithin. *Journal of the American Chemical Society*, 117:3310–3311, 1995.

[266] J. C. Gower and G. J. S. Ross. Minimum Spanning Trees and Single Linkage Cluster Analysis. *Applied Statistics*, 18:54, 1969.

[267] C. A. Stanich, A. R. Honerkamp-Smith, G. G. Putzel, C. S. Warth, A. K. Lamprecht, P. Mandal, E. Mann, T. A. D. Hua, and S. L. Keller. Coarsening dynamics of domains in lipid membranes. *Biophysical Journal*, 105:444–454, 2013.

[268] L. Li, I. Vorobyov, and T. W. Allen. The Different Interactions of Lysine and Arginine Side Chains with Lipid Membranes. *The Journal of Physical Chemistry B*, 117:11906–11920, 2013.

[269] T. Oroguchi and M. Nakasako. Influences of lone-pair electrons on directionality of hydrogen bonds formed by hydrophilic amino acid side chains in molecular dynamics simulation. *Scientific Reports*, 7:3–14, 2017.

[270] D. Matsuoka and M. Nakasako. Probability distributions of hydration water molecules around polar protein atoms obtained by a database analysis. *Journal of Physical Chemistry B*, 113:11274–11292, 2009.

[271] G. Grigoryan and W. F. Degrado. Probing designability via a generalized model of helical bundle geometry. *Journal of Molecular Biology*, 405:1079–1100, 2011.

[272] W. Im, M. Feig, and C. L. Brooks. An Implicit Membrane Generalized Born Theory for the Study of Structure, Stability, and Interactions of Membrane Proteins. *Biophysical Journal*, 85:2900–2918, 2003.

[273] R. B. Best, X. Zhu, J. Shim, P. E. Lopes, J. Mittal, M. Feig, and A. D. MacKerell. Optimization of the additive CHARMM all-atom protein force field targeting improved sampling of the backbone ϕ, ψ and side-chain $\chi1$ and $\chi2$ Dihedral Angles. *Journal of Chemical Theory and Computation*, 8:3257–3273, 2012.

[274] J. B. Klauda, R. M. Venable, J. A. Freites, J. W. O'Connor, D. J. Tobias, C. Mondragon-Ramirez, I. Vorobyov, A. D. MacKerell, and R. W. Pastor. Update of the CHARMM All-Atom Additive Force Field for Lipids: Validation on Six Lipid Types. *Journal of Physical Chemistry B*, 114:7830–7843, 2010.

[275] J. Huang, S. Rauscher, G. Nawrocki, T. Ran, M. Feig, B. L. De Groot, H. Grubmüller, and A. D. MacKerell. CHARMM36m: An improved force field for folded and intrinsically disordered proteins. *Nature Methods*, 14:71–73, 2016.

[276] S. Pronk, S. Páll, R. Schulz, P. Larsson, P. Bjelkmar, R. Apostolov, M. R. Shirts, J. C. Smith, P. M. Kasson, D. van der Spoel, B. Hess, and E. Lindahl. GROMACS 4.5: a high-throughput and highly parallel open source molecular simulation toolkit. *Bioinformatics*, 29:845–854, 2013.

[277] M. J. Abraham, T. Murtola, R. Schulz, S. Páll, J. C. Smith, B. Hess, and E. Lindahl. GROMACS: High performance molecular simulations through multi-level parallelism from laptops to supercomputers. *SoftwareX*, 1-2:19–25, 2015.

[278] B. R. Brooks, C. L. Brooks, A. D. Mackerell, L. Nilsson, R. J. Petrella, B. Roux, Y. Won, G. Archontis, C. Bartels, S. Boresch, A. Caflisch, L. Caves, Q. Cui, A. R. Dinner, M. Feig, S. Fischer, J. Gao, M. Hodoscek, W. Im, K. Kuczera, T. Lazaridis, J. Ma, V. Ovchinnikov, E. Paci, R. W. Pastor, C. B. Post, J. Z. Pu, M. Schaefer, B. Tidor, R. M. Venable, H. L. Woodcock, X. Wu, W. Yang, D. M. York, and M. Karplus. CHARMM: The biomolecular simulation program. *Journal of Computational Chemistry*, 30:1545–1614, 2009.

[279] J. Jung, T. Mori, C. Kobayashi, Y. Matsunaga, T. Yoda, M. Feig, and Y. Sugita. GENESIS: A hybrid-parallel and multi-scale molecular dynamics simulator with enhanced sampling algorithms for biomolecular and cellular simulations. *Wiley Interdisciplinary Reviews: Computational Molecular Science*, 5:310–323, 2015.

[280] C. Kobayashi, J. Jung, Y. Matsunaga, T. Mori, T. Ando, K. Tamura, M. Kamiya, and Y. Sugita. GENESIS 1.1: A hybrid-parallel molecular dynamics simulator with enhanced sampling algorithms on multiple computational platforms. *Journal of Computational Chemistry*, 38:2193–2206, 2017.

[281] S. van der Walt, S. C. Colbert, and G. Varoquaux. The NumPy Array: A Structure for Efficient Numerical Computation. *Computing in Science & Engineering*, 13:22–30, 2011.

[282] R. Gowers, M. Linke, J. Barnoud, T. Reddy, M. Melo, S. Seyler, J. Domański, D. Dotson, S. Buchoux, I. Kenney, and O. Beckstein. MDAnalysis: A Python Package for the Rapid Analysis of Molecular Dynamics Simulations. In *Proceedings of the 15th Python in Science Conference*, pages 98–105. Scipy, 2016.

[283] N. Michaud-Agrawal, E. J. Denning, T. B. Woolf, and O. Beckstein. MDAnalysis: A toolkit for the analysis of molecular dynamics simulations. *Journal of Computational Chemistry*, 32:2319–2327, 2011.

[284] S. Behnel, R. Bradshaw, C. Citro, L. Dalcin, D. S. Seljebotn, and K. Smith. Cython: The Best of Both Worlds. *Computing in Science & Engineering*, 13:31–39, 2011.

[285] J. D. Hunter. Matplotlib: A 2D graphics environment. *Computing In Science & Engineering*, 9:90–95, 2007.

[286] W. Humphrey, A. Dalke, and K. Schulten. VMD - Visual Molecular Dynamics. *Journal of Molecular Graphics*, 14:33–38, 1996.

[287] J. Stone. *An Efficient Library for Parallel Ray Tracing and Animation*. PhD thesis, Computer Science Department, University of Missouri-Rolla, 1998.

[288] Y. Sugita and Y. Okamoto. Replica-exchange molecular dynamics method for protein folding. *Chemical Physics Letters*, 314:141–151, 1999.

[289] Y. Sugita, M. Kamiya, H. Oshima, and S. Re. Replica-Exchange Methods for Biomolecular Simulations. In *Biomolecular Simulations*, chapter 7, pages 155–177. Humana, New York, NY, 2019.

[290] P. Liu, B. Kim, R. a. Friesner, and B. J. Berne. Replica exchange with solute tempering: A method for sampling biological systems in explicit water. *Proceedings of the National Academy of Sciences*, 102:13749–13754, 2005.

[291] H. Wang, L. Barreyro, D. Provasi, I. Djemil, C. Torres-Arancivia, M. Filizola, and I. Ubarretxena-Belandia. Molecular determinants and thermodynamics of the amyloid precursor protein transmembrane domain implicated in alzheimer's disease. *Journal of Molecular Biology*, 408:879–895, 2011.

[292] M. Kamiya and Y. Sugita. Flexible selection of the solute region in replica exchange with solute tempering: Application to protein-folding simulations. *The Journal of Chemical Physics*, 149:072304, 2018.

[293] D. Matsuoka, M. Kamiya, T. Sato, and Y. Sugita. Role of the N-Terminal Transmembrane Helix Contacts in the Activation of FGFR3. *Journal of Computational Chemistry*, 41:561–572, 2020.

[294] I.-C. Yeh. System-Size Dependence of Diffusion Coefficients and Viscosities from Molecular Dynamics Simulations with Periodic Boundary Conditions. *Journal of Physical Chemistry B*, 108:15873–15879, 2004.

[295] K. Takemura and A. Kitao. Effects of water model and simulation box size on protein diffusional motions. *The journal of physical chemistry. B*, 111: 11870–11872, 2007.

[296] B. Chandramouli, C. Zazza, G. Mancini, and G. Brancato. Boundary condition effects on the dynamic and electric properties of hydration layers. *Journal of Physical Chemistry A*, 119:5465–5475, 2015.

[297] J. B. Klauda, B. R. Brooks, and R. W. Pastor. Dynamical motions of lipids and a finite size effect in simulations of bilayers. *The Journal of Chemical Physics*, 125:144710, 2006.

[298] F. Castro-Román, R. W. Benz, S. H. White, and D. J. Tobias. Investigation of Finite System-Size Effects in Molecular Dynamics Simulations of Lipid Bilayers. *The Journal of Physical Chemistry B*, 110:24157–24164, 2006.

[299] B. A. Camley, M. G. Lerner, R. W. Pastor, and F. L. H. Brown. Strong influence of periodic boundary conditions on lateral diffusion in lipid bilayer membranes. *The Journal of Chemical Physics*, 143:243113, 2015.

[300] W. Scott, F. Müller-Plathe, and W. Van Gunsteren. Molecular dynamics study of the mixing and demixing of a binary Lennard-Jones fluid. *Molecular Physics*, 82:1049–1062, 1994.

[301] J. Huang and G. W. Feigenson. Monte Carlo simulation of lipid mixtures: finding phase separation. *Biophys J*, 65:1788–1794, 1993.

[302] S. L. Duncan, I. S. Dalal, and R. G. Larson. Molecular dynamics simulation of phase transitions in model lung surfactant monolayers. *Biochimica et biophysica acta*, 1808:2450–2465, 2011.

[303] T. Nagai, R. Ueoka, and Y. Okamoto. Phase behavior of a lipid bilayer system studied by a replica-exchange molecular dynamics simulation. *Journal of the Physical Society of Japan*, 81:1–9, 2012.

[304] S. J. Marrink, H. J. Risselada, S. Yefimov, D. P. Tieleman, and A. H. de Vries. The MARTINI Force Field: Coarse Grained Model for Biomolecular Simulations. *The Journal of Physical Chemistry B*, 111:7812–7824, 2007.

[305] S. V. Dvinskikh, V. Castro, and D. Sandström. Probing segmental order in lipid bilayers at variable hydration levels by amplitude- and phase-modulated cross-polarization NMR. *Phys Chem Chem Phys*, 7:3255–3257, 2005.

[306] T. A. Wassenaar, H. I. Ingólfsson, R. A. Böckmann, D. P. Tieleman, and S. J. Marrink. Computational Lipidomics with insane : A Versatile Tool for Generating Custom Membranes for Molecular Simulations. *Journal of Chemical Theory and Computation*, 11:2144–2155, 2015.

[307] D. H. De Jong, S. Baoukina, H. I. Ingólfsson, and S. J. Marrink. Martini straight: Boosting performance using a shorter cutoff and GPUs. *Computer Physics Communications*, 199:1–7, 2016.

[308] L. V. Schafer, D. H. de Jong, A. Holt, A. J. Rzepiela, A. H. de Vries, B. Poolman, J. A. Killian, and S. J. Marrink. Lipid packing drives the segregation of transmembrane helices into disordered lipid domains in model membranes. *Proceedings of the National Academy of Sciences*, 108:1343–1348, 2011.

[309] J. D. Perlmutter and J. N. Sachs. Interleaflet Interaction and Asymmetry in Phase Separated Lipid Bilayers: Molecular Dynamics Simulations. *Journal of the American Chemical Society*, 133:6563–6577, 2011.

[310] J. Domański, S. J. Marrink, and L. V. Schäfer. Transmembrane helices can induce domain formation in crowded model membranes. *Biochimica et Biophysica Acta (BBA) - Biomembranes*, 1818:984–994, 2012.

[311] D. Hakobyan and A. Heuer. Phase Separation in a Lipid/Cholesterol System: Comparison of Coarse-Grained and United-Atom Simulations. *The Journal of Physical Chemistry B*, 117:3841–3851, 2013.

[312] R. S. Davis, P. B. Sunil Kumar, M. M. Sperotto, and M. Laradji. Predictions of Phase Separation in Three-Component Lipid Membranes by the MARTINI Force Field. *The Journal of Physical Chemistry B*, 117:4072–4080, 2013.

[313] Q. Liang, Q.-Y. Wu, and Z.-Y. Wang. Effect of hydrophobic mismatch on domain formation and peptide sorting in the multicomponent lipid bilayers in the presence of immobilized peptides. *The Journal of Chemical Physics*, 141:074702, 2014.

[314] D. G. Ackerman and G. W. Feigenson. Multiscale Modeling of Four-Component Lipid Mixtures: Domain Composition, Size, Alignment, and Properties of the Phase Interface. *The Journal of Physical Chemistry B*, 119:4240–4250, 2015.

[315] D. L. Parton, A. Tek, M. Baaden, and M. S. P. Sansom. Formation of Raft-Like Assemblies within Clusters of Influenza Hemagglutinin Observed by MD Simulations. *PLoS Computational Biology*, 9:e1003034, 2013.

[316] C. Rosetti and C. Pastorino. Polyunsaturated and Saturated Phospholipids in Mixed Bilayers: A Study from the Molecular Scale to the Lateral Lipid Organization. *The Journal of Physical Chemistry B*, 115:1002–1013, 2011.

[317] S. Komura, H. Shirotori, P. D. Olmsted, and D. Andelman. Lateral phase separation in mixtures of lipids and cholesterol. *Europhysics Letters (EPL)*, 67:321–327, 2004.

[318] S. Komura, H. Shirotori, and P. D. Olmsted. Phase behaviour of three-component lipid mixtures. *Journal of Physics: Condensed Matter*, 17:S2951–S2956, 2005.

[319] T. Idema, J. M. J. van Leeuwen, and C. Storm. Phase coexistence and line tension in ternary lipid systems. *Physical Review E*, 80:041924, 2009.

[320] A. Radhakrishnan and H. McConnell. Condensed complexes in vesicles containing cholesterol and phospholipids. *Proceedings of the National Academy of Sciences of the United States of America*, 102:12662–6, 2005.

[321] H. M. McConnell and M. Vrljic. Liquid-Liquid Immiscibility in Membranes. *Annual Review of Biophysics and Biomolecular Structure*, 32:469–492, 2003.

[322] P. J. Flory. Thermodynamics of High Polymer Solutions. *The Journal of Chemical Physics*, 10:51–61, 1942.

[323] S. J. Marrink, J. Risselada, and A. E. Mark. Simulation of gel phase formation and melting in lipid bilayers using a coarse grained model. *Chemistry and Physics of Lipids*, 135:223–244, 2005.

[324] E. M. Curtis, X. Xiao, S. Sofou, and C. K. Hall. Phase separation behavior of mixed lipid systems at neutral and low pH: Coarse-grained simulations with DMD/LIME. *Langmuir*, 31:1086–1094, 2015.

[325] C. Hong, D. P. Tieleman, and Y. Wang. Microsecond Molecular Dynamics Simulations of Lipid Mixing. *Langmuir*, 30:11993–12001, 2014.

[326] C. M. MacDermaid, H. K. Kashyap, R. H. DeVane, W. Shinoda, J. B. Klauda, M. L. Klein, and G. Fiorin. Molecular dynamics simulations of cholesterol-rich membranes using a coarse-grained force field for cyclic alkanes. *The Journal of Chemical Physics*, 143:243144, 2015.

[327] C. Rosetti and C. Pastorino. Comparison of Ternary Bilayer Mixtures with Asymmetric or Symmetric Unsaturated Phosphatidylcholine Lipids by Coarse Grained Molecular Dynamics Simulations. *The Journal of Physical Chemistry B*, 116:3525–3537, 2012.

[328] G. W. G. Feigenson. Phase boundaries and biological membranes. *Annual review of biophysics and biomolecular structure*, 36:63–77, 2007.

[329] G. W. Feigenson. Phase diagrams and lipid domains in multicomponent lipid bilayer mixtures. *Biochimica et Biophysica Acta (BBA) - Biomembranes*, 1788:47–52, 2009.

[330] E. Winkler, A. Julius, H. Steiner, and D. Langosch. Homodimerization protects the amyloid precursor protein C99 fragment from cleavage by gamma-secretase. *Biochemistry*, 54:6149–6152, 2015.

[331] G. van Meer, D. R. Voelker, and G. W. Feigenson. Membrane lipids: where they are and how they behave. *Nature Reviews Molecular Cell Biology*, 9: 112–124, 2008.

[332] G. van Meer and A. I. P. M. de Kroon. Lipid map of the mammalian cell. *Journal of Cell Science*, 124:5–8, 2011.

[333] A. Y. Abramov, M. Ionov, E. Pavlov, and M. R. Duchen. Membrane cholesterol content plays a key role in the neurotoxicity of beta-amyloid: Implications for Alzheimer's disease. *Aging Cell*, 10:595–603, 2011.

[334] W. Wood, F. Schroeder, U. Igbavboa, N. Avdulov, and S. Chochina. Brain membrane cholesterol domains, aging and amyloid beta-peptides. *Neurobiology of Aging*, 23:685–694, 2002.

[335] G. A. Pantelopulos, T. Nagai, A. Bandara, A. Panahi, and J. E. Straub. Critical size dependence of domain formation observed in coarse-grained simulations of bilayers composed of ternary lipid mixtures. *Journal of Chemical Physics*, 147:095101, 2017.

[336] M. C. Blosser, A. R. Honerkamp-Smith, T. Han, M. Haataja, and S. L. Keller. Transbilayer Colocalization of Lipid Domains Explained via Measurement of Strong Coupling Parameters. *Biophysical Journal*, 109:2317–2327, 2015.

[337] M. P. Haataja. Lipid Domain Co-localization Induced by Membrane Undulations. *Biophysical Journal*, 112:655–662, 2017.

[338] P. B. S. Kumar, G. Gompper, and R. Lipowsky. Modulated phases in multicomponent fluid membranes. *Physical Review E*, 60:4610–4618, 1999.

[339] S. Leibler and D. Andelman. Ordered and curved meso-structures in membranes and amphiphilic films. *J. Physique*, 48:2013–2018, 1987.

[340] M. Schick. Membrane heterogeneity: Manifestation of a curvature-induced microemulsion. *Physical Review E - Statistical, Nonlinear, and Soft Matter Physics*, 85:1–4, 2012.

[341] M. Schick. Strongly Correlated Rafts in Both Leaves of an Asymmetric Bilayer. *The Journal of Physical Chemistry B*, 122:3251–3258, 2018.

[342] F. Schmid, S. Dolezel, O. Lenz, and S. Meinhardt. On ripples and rafts: Curvature induced nanoscale structures in lipid membranes. *Journal of Physics: Conference Series*, 487:012004, 2014.

[343] R. Shlomovitz and M. Schick. Model of a raft in both leaves of an asymmetric lipid bilayer. *Biophysical Journal*, 105:1406–1413, 2013.

[344] J. J. Williamson and P. D. Olmsted. Registered and Antiregistered Phase Separation of Mixed Amphiphilic Bilayers. *Biophysical Journal*, 108:1963–1976, 2015.

[345] V. Kiessling, C. Wan, and L. K. Tamm. Domain coupling in asymmetric lipid bilayers. *Biochimica et Biophysica Acta - Biomembranes*, 1788:64–71, 2009.

[346] J. D. Nickels, J. C. Smith, and X. Cheng. Lateral organization, bilayer asymmetry, and inter-leaflet coupling of biological membranes. *Chemistry and Physics of Lipids*, 192:87–99, 2015.

[347] C. Wan, V. Kiessling, and L. K. Tamm. Coupling of cholesterol-rich lipid phases in asymmetric bilayers. *Biochemistry*, 47:2190–2198, 2008.

[348] B. Kollmitzer, P. Heftberger, M. Rappolt, and G. Pabst. Monolayer spontaneous curvature of raft-forming membrane lipids. *Soft Matter*, 9:10877, 2013.

[349] D. Stelter and T. Keyes. Enhanced Sampling of Phase Transitions in Coarse-Grained Lipid Bilayers. *Journal of Physical Chemistry B*, 121:5770–5780, 2017.

[350] P. W. Fowler, J. J. Williamson, M. S. Sansom, and P. D. Olmsted. Roles of Interleaflet Coupling and Hydrophobic Mismatch in Lipid Membrane Phase-Separation Kinetics. *Journal of the American Chemical Society*, 138:11633–11642, 2016.

[351] S. He and L. Maibaum. Identifying the Onset of Phase Separation in Quaternary Lipid Bilayer Systems from Coarse-Grained Simulations. *ArXiv e-prints*, 2018.

[352] S. O. Yesylevskyy, a. P. Demchenko, S. Kraszewski, and C. Ramseyer. Cholesterol Induces Uneven Curvature of Asymmetric Lipid Bilayers. *The Scientific World Journal*, 2013:1–10, 2013.

[353] G. Bussi and M. Parrinello. Accurate sampling using Langevin dynamics. *Physical Review E - Statistical, Nonlinear, and Soft Matter Physics*, 75:1–7, 2007.

[354] J. Towns, T. Cockerill, M. Dahan, I. Foster, K. Gaither, A. Grimshaw, V. Hazlewood, S. Lathrop, D. Lifka, G. D. Peterson, R. Roskies, J. R. Scott, and N. Wilkens-Diehr. XSEDE: Accelerating Scientific Discovery. *Computing in Science & Engineering*, 16:62–74, 2014.

[355] W. Wang, L. Yang, and H. W. Huang. Evidence of Cholesterol Accumulated in High Curvature Regions: Implication to the Curvature Elastic Energy for Lipid Mixtures. *Biophysical Journal*, 92:2819–2830, 2007.

[356] K. Bacia, P. Schwille, and T. Kurzchalia. Sterol structure determines the separation of phases and the curvature of the liquid-ordered phase in model membranes. *Proceedings of the National Academy of Sciences of the United States of America*, 102:3272–7, 2005.

[357] Y. Wang, P. Gkeka, J. E. Fuchs, K. R. Liedl, and Z. Cournia. DPPC-cholesterol phase diagram using coarse-grained Molecular Dynamics simulations. *Biochimica et Biophysica Acta - Biomembranes*, 1858:2846–2857, 2016.

[358] S. Katira, K. K. Mandadapu, S. Vaikuntanathan, B. Smit, and D. Chandler. Pre-transition effects mediate forces of assembly between transmembrane proteins. *eLife*, 5:1–8, 2016.

[359] D. T. Moore, B. W. Berger, and W. F. DeGrado. Protein-Protein Interactions in the Membrane: Sequence, Structural, and Biological Motifs. *Structure*, 16:991–1001, 2008.

[360] B. K. Mueller, S. Subramaniam, and A. Senes. A frequent, GxxxG-mediated, transmembrane association motif is optimized for the formation of interhelical C -H hydrogen bonds. *Proceedings of the National Academy of Sciences*, 111: E888–E895, 2014.

[361] Ł. Nierzwicki and J. Czub. Specific binding of cholesterol to the amyloid precursor protein: Structure of the complex and driving forces characterized in molecular detail. *Journal of Physical Chemistry Letters*, 6:784–790, 2015.

[362] M. Benčina. Illumination of the spatial order of intracellular pH by genetically encoded pH-sensitive sensors. *Sensors (Switzerland)*, 13:16736–16758, 2013.

[363] J. Montesinos, M. Pera, D. Larrea, C. Guardia-Laguarta, R. R. Agrawal, K. R. Velasco, T. D. Yun, I. G. Stavrovskaya, Y. Xu, S. Y. Koo, A. M. Snead, A. A. Sproul, and E. Area-Gomez. The Alzheimer's disease-associated C99 fragment of APP regulates cellular cholesterol trafficking. *The EMBO Journal*, 39:1–16, 2020.

[364] I. Levitan, D. K. Singh, and A. Rosenhouse-Dantsker. Cholesterol binding to ion channels. *Frontiers in Physiology*, 5:65, 2014.

[365] D. Sengupta and A. Chattopadhyay. Molecular dynamics simulations of GPCR-cholesterol interaction: An emerging paradigm. *Biochimica et Biophysica Acta - Biomembranes*, 1848:1775–1782, 2015.

[366] G. Hedger and M. S. Sansom. Lipid interaction sites on channels, transporters and receptors: Recent insights from molecular dynamics simulations. *Biochimica et Biophysica Acta - Biomembranes*, 1858:2390–2400, 2016.

[367] J. Fantini, C. Di Scala, L. S. Evans, P. T. F. Williamson, and F. J. Barrantes. A mirror code for protein-cholesterol interactions in the two leaflets of biological membranes. *Scientific Reports*, 6:21907, 2016.

[368] S. Genheden, J. W. Essex, and A. G. Lee. G protein coupled receptor interactions with cholesterol deep in the membrane. *Biochimica et Biophysica Acta - Biomembranes*, 1859:268–281, 2017.

[369] E. Rouviere, C. Arnarez, L. Yang, and E. Lyman. Identification of Two New Cholesterol Interaction Sites on the A2A Adenosine Receptor. *Biophysical Journal*, 113:2415–2424, 2017.

[370] N. Barbera, M. A. Ayee, B. S. Akpa, and I. Levitan. Molecular Dynamics Simulations of Kir2.2 Interactions with an Ensemble of Cholesterol Molecules. *Biophysical Journal*, 115:1264–1280, 2018.

[371] W. Song, H. Y. Yen, C. V. Robinson, and M. S. Sansom. State-dependent Lipid Interactions with the A2a Receptor Revealed by MD Simulations Using In Vivo-Mimetic Membranes. *Structure*, 27:392–403.e3, 2019.

[372] G. Hedger, H. Koldsø, M. Chavent, C. Siebold, R. Rohatgi, and M. S. Sansom. Cholesterol Interaction Sites on the Transmembrane Domain of the Hedgehog Signal Transducer and Class F G Protein-Coupled Receptor Smoothened. *Structure*, 27:549–559.e2, 2019.

[373] S. N. Fatakia, P. Sarkar, and A. Chattopadhyay. A collage of cholesterol interaction motifs in the serotonin1A receptor: An evolutionary implication for differential cholesterol interaction. *Chemistry and Physics of Lipids*, 221: 184–192, 2019.

[374] A. G. Lee. Interfacial binding sites for cholesterol on G protein coupled receptors. *Biophysical Journal*, pages 1–12, 2019.

[375] H. Li and V. Papadopoulos. Peripheral-type benzodiazepine receptor function in cholesterol transport. Identification of a putative cholesterol recognition/interaction amino acid sequence and consensus pattern. *Endocrinology*, 139:4991–4997, 1998.

[376] C. J. Baier, J. Fantini, and F. J. Barrantes. Disclosure of cholesterol recognition motifs in transmembrane domains of the human nicotinic acetylcholine receptor. *Scientific Reports*, 1:69, 2011.

[377] F. Massi, J. W. Peng, J. P. Lee, and J. E. Straub. Simulation study of the structure and dynamics of the Alzheimer's amyloid peptide congener in solution. *Biophysical Journal*, 80:31–44, 2001.

[378] K. D. Nadezhdin, O. V. Bocharova, E. V. Bocharov, and A. S. Arseniev. Dimeric structure of transmembrane domain of amyloid precursor protein in micellar environment. *FEBS Letters*, 586:1687–1692, 2012.

[379] S. Jo, T. Kim, and W. Im. Automated builder and database of protein/membrane complexes for molecular dynamics simulations. *PLoS ONE*, 2, 2007.

[380] S. Jo, T. Kim, V. G. Iyer, and W. Im. CHARMM-GUI: A web-based graphical user interface for CHARMM. *Journal of Computational Chemistry*, 29:1859–1865, 2008.

[381] E. L. Wu, X. Cheng, S. Jo, H. Rui, K. C. Song, E. M. Dávila-Contreras, Y. Qi, J. Lee, V. Monje-Galvan, R. M. Venable, J. B. Klauda, and W. Im. CHARMM-GUI membrane builder toward realistic biological membrane simulations. 35:1997–2004, 2014.

[382] J. Lee, X. Cheng, J. M. Swails, M. S. Yeom, P. K. Eastman, J. A. Lemkul, S. Wei, J. Buckner, J. C. Jeong, Y. Qi, S. Jo, V. S. Pande, D. A. Case, C. L. Brooks, A. D. MacKerell, J. B. Klauda, and W. Im. CHARMM-GUI Input Generator for NAMD, GROMACS, AMBER, OpenMM, and CHARMM /OpenMM Simulations Using the CHARMM36 Additive Force Field. *Journal of Chemical Theory and Computation*, 12:405–413, 2016.

[383] S. Miyamoto and P. A. Kollman. Settle: An analytical version of the SHAKE and RATTLE algorithm for rigid water models. *Journal of Computational Chemistry*, 13:952–962, 1992.

[384] M. Di Pierro, R. Elber, and B. Leimkuhler. A Stochastic Algorithm for the Isobaric–Isothermal Ensemble with Ewald Summations for All Long Range Forces. *Journal of Chemical Theory and Computation*, 11:5624–5637, 2015.

[385] A. Cheng and K. M. Merz. Application of the Nosé-Hoover Chain Algorithm to the Study of Protein Dynamics. *The Journal of Physical Chemistry*, 100: 1927–1937, 1996.

[386] M. Parrinello and A. Rahman. Polymorphic transitions in single crystals: A new molecular dynamics method. *Journal of Applied Physics*, 52:7182–7190, 1981.

[387] M. Wang, T. Jing, X. Wang, and D. Yao. Beta-secretase/BACE1 promotes APP endocytosis and processing in the endosomes and on cell membrane. *Neuroscience Letters*, 685:63–67, 2018.

[388] M. A. Castro, A. Hadziselimovic, and C. R. Sanders. The vexing complexity of the amyloidogenic pathway. *Protein Science*, 28:1177–1193, 2019.

[389] G. A. Pantelopulos and J. E. Straub. Regimes of Complex Lipid Bilayer Phases Induced by Cholesterol Concentration in MD Simulation. *Biophysical Journal*, 115:2167–2178, 2018.

[390] J. Yoo and A. Aksimentiev. New tricks for old dogs: Improving the accuracy of biomolecular force fields by pair-specific corrections to non-bonded interactions. *Physical Chemistry Chemical Physics*, 20:8432–8449, 2018.

[391] J. H. Lorent, K. R. Levental, L. Ganesan, G. Rivera-Longsworth, E. Sezgin, M. Doktorova, E. Lyman, and I. Levental. Plasma membranes are asymmetric in lipid unsaturation, packing and protein shape. *Nature Chemical Biology*, 16:644–652, 2020.

[392] B. Tarus, J. E. Straub, and D. Thirumalai. Dynamics of Asp23-Lys28 Salt-Bridge Formation in Abeta 10-35 Monomers. *Journal of the American Chemical Society*, 128:16159–16168, 2006.

[393] N. L. Fawzi, A. H. Phillips, J. Z. Ruscio, M. Doucleff, D. E. Wemmer, and T. Head-Gordon. Structure and Dynamics of the Aβ 21–30 Peptide from the Interplay of NMR Experiments and Molecular Simulations. *Journal of the American Chemical Society*, 130:6145–6158, 2008.

[394] N. Miyashita, J. E. Straub, and D. Thirumalai. Structures of β-Amyloid Peptide 1-40, 1-42, and 1-55—the 672-726 Fragment of APP—in a Membrane Environment with Implications for Interactions with γ-Secretase. *Journal of the American Chemical Society*, 131:17843–17852, 2009.

[395] Y. Shen, F. Delaglio, G. Cornilescu, and A. Bax. TALOS+: A hybrid method for predicting protein backbone torsion angles from NMR chemical shifts. *Journal of Biomolecular NMR*, 44:213–223, 2009.

[396] M. V. Shapovalov and R. L. Dunbrack. A smoothed backbone-dependent rotamer library for proteins derived from adaptive kernel density estimates and regressions. *Structure*, 19:844–858, 2011.

[397] E. F. Pettersen, T. D. Goddard, C. C. Huang, G. S. Couch, D. M. Greenblatt, E. C. Meng, and T. E. Ferrin. UCSF Chimera - A visualization system for exploratory research and analysis. *Journal of Computational Chemistry*, 25: 1605–1612, 2004.

[398] J. Huang and A. D. MacKerell. CHARMM36 all-atom additive protein force field: Validation based on comparison to NMR data. *Journal of Computational Chemistry*, 34:2135–2145, 2013.

[399] C. M. Siwy, C. Lockhart, and D. K. Klimov. Is the Conformational Ensemble of Alzheimer's Aβ10-40 Peptide Force Field Dependent? *PLoS Computational Biology*, 13:1–26, 2017.

[400] B. Han, Y. Liu, S. W. Ginzinger, and D. S. Wishart. SHIFTX2: Significantly improved protein chemical shift prediction. *Journal of Biomolecular NMR*, 50:43–57, 2011.

[401] A. Altis, P. H. Nguyen, R. Hegger, and G. Stock. Dihedral angle principal component analysis of molecular dynamics simulations. *Journal of Chemical Physics*, 126:1–10, 2007.

[402] A. P. Dempster, N. M. Laird, and D. B. Rubin. Maximum Likelihood from Incomplete Data via the EM Algorithm. *Journal of the Royal Statistical Society. Series B (Methodological)*, 39:1–38, 1977.

[403] T. Mori, N. Miyashita, W. Im, M. Feig, and Y. Sugita. Molecular dynamics simulations of biological membranes and membrane proteins using enhanced conformational sampling algorithms. *Biochimica et Biophysica Acta (BBA) - Biomembranes*, 1858:1635–1651, 2016.

[404] N. Kučerka, M. P. Nieh, and J. Katsaras. Fluid phase lipid areas and bilayer thicknesses of commonly used phosphatidylcholines as a function of temperature. *Biochimica et Biophysica Acta - Biomembranes*, 1808:2761–2771, 2011.

[405] S. Vivekanandan, J. R. Brender, S. Y. Lee, and A. Ramamoorthy. A partially folded structure of amyloid-beta(1–40) in an aqueous environment. *Biochemical and Biophysical Research Communications*, 411:312–316, 2011.

[406] S. Furlan, C. Hureau, P. Faller, and G. La Penna. Modeling the Cu+ Binding in the 1-16 Region of the Amyloid-β Peptide Involved in Alzheimer's Disease. *The Journal of Physical Chemistry B*, 114:15119–15133, 2010.

[407] S. Furlan, C. Hureau, P. Faller, and G. La Penna. Modeling copper binding to the amyloid-β peptide at different pH: Toward a molecular mechanism for Cu reduction. *Journal of Physical Chemistry B*, 116:11899–11910, 2012.

[408] P. H. Nguyen, A. Ramamoorthy, B. R. Sahoo, J. Zheng, P. Faller, J. E. Straub, L. Dominguez, J. E. Shea, N. V. Dokholyan, A. de Simone, B. Ma, R. Nussinov, S. Najafi, S. T. Ngo, A. Loquet, M. Chiricotto, P. Ganguly, J. McCarty, M. S. Li, C. Hall, Y. Wang, Y. Miller, S. Melchionna, B. Habenstein, S. Timr, J. Chen, B. Hnath, B. Strodel, R. Kayed, S. Lesné, G. Wei, F. Sterpone, A. J. Doig, and P. Derreumaux. Amyloid oligomers: A joint experimental/computational perspective on Alzheimer's disease, Parkinson's disease, type II diabetes, and amyotrophic lateral sclerosis. *Chemical Reviews*, 121: 2545–2647, 2021.

[409] H. Zheng and E. H. Koo. Biology and pathophysiology of the amyloid precursor protein. *Molecular Neurodegeneration*, 6:1–16, 2011.

[410] T. A. Caldwell, S. Baoukina, A. T. Brock, R. C. Oliver, K. T. Root, J. K. Krueger, K. J. Glover, D. P. Tieleman, and L. Columbus. Low-q Bicelles Are Mixed Micelles. *The Journal of Physical Chemistry Letters*, 9:4469–4473, 2018.

[411] A. Piai, Q. Fu, J. Dev, and J. J. Chou. Optimal Bicelle Size q for Solution NMR Studies of the Protein Transmembrane Partition. *Chemistry - A European Journal*, 23:1361–1367, 2017.

[412] T. L. Hwang, S. Mori, A. J. Shaka, and P. C. M. Van Zijl. Application of phase-modulated CLEAN chemical EXchange spectroscopy (CLEANEX-PM) to detect water - Protein proton exchange and intermolecular NOEs. *Journal of the American Chemical Society*, 119:6203–6204, 1997.

[413] J. J. Skinner, W. K. Lim, S. Bédard, B. E. Black, and S. W. Englander. Protein hydrogen exchange: Testing current models. *Protein Science*, 21:987–995, 2012.

[414] R. Capone, A. Tiwari, A. Hadziselimovic, Y. Peskova, J. M. Hutchison, C. R. Sanders, and A. K. Kenworthy. The C99 domain of the amyloid precursor protein resides in the disordered membrane phase. *Journal of Biological Chemistry*, 296:100652, 2021.

[415] M. Tuckerman, B. J. Berne, and G. J. Martyna. Reversible multiple time scale molecular dynamics. *The Journal of Chemical Physics*, 97:1990–2001, 1992.

[416] J. Jung, C. Kobayashi, and Y. Sugita. Kinetic energy definition in velocity Verlet integration for accurate pressure evaluation. *The Journal of Chemical Physics*, 148:164109, 2018.

[417] W. L. Jorgensen, J. Chandrasekhar, J. D. Madura, R. W. Impey, and M. L. Klein. Comparison of simple potential functions for simulating liquid water. *The Journal of Chemical Physics*, 79:926–935, 1983.

[418] J. Domański, M. S. Sansom, P. J. Stansfeld, and R. B. Best. Balancing Force Field Protein-Lipid Interactions to Capture Transmembrane Helix-Helix Association. *Journal of Chemical Theory and Computation*, 14:1706–1715, 2018.

[419] U. Essmann, L. Perera, M. L. Berkowitz, T. Darden, H. Lee, and L. G. Pedersen. A smooth particle mesh Ewald method. *The Journal of Chemical Physics*, 103:8577–8593, 1995.

[420] H. C. Andersen. Rattle: A "velocity" version of the shake algorithm for molecular dynamics calculations. *Journal of Computational Physics*, 52:24–34, 1983.

[421] J. P. Ryckaert, G. Ciccotti, and H. J. Berendsen. Numerical integration of the cartesian equations of motion of a system with constraints: molecular dynamics of n-alkanes. *Journal of Computational Physics*, 23:327–341, 1977.

[422] G. Bussi, T. Zykova-Timan, and M. Parrinello. Isothermal-isobaric molecular dynamics using stochastic velocity rescaling. *Journal of Chemical Physics*, 130, 2009.

[423] J. H. W. Jr. Hierarchical Grouping to Optimize an Objective Function. *Journal of the American Statistical Association*, 58:236–244, 1963.

[424] P. J. Rousseeuw. Silhouettes: A graphical aid to the interpretation and validation of cluster analysis. *Journal of Computational and Applied Mathematics*, 20:53–65, 1987.

[425] D. Thirumalai, R. D. Mountain, and T. R. Kirkpatrick. Ergodic behavior in supercooled liquids and in glasses. *Physical Review A*, 39:3563–3574, 1989.

[426] D. Thirumalai and R. D. Mountain. Ergodic convergence properties of supercooled liquids and glasses. *Physical Review A*, 42:4574–4587, 1990.

[427] J. E. Straub and D. Thirumalai. Exploring the energy landscape in proteins. *Proceedings of the National Academy of Sciences of the United States of America*, 90:809–813, 1993.

[428] U. Baul, D. Chakraborty, M. L. Mugnai, J. E. Straub, and D. Thirumalai. Sequence Effects on Size, Shape, and Structural Heterogeneity in Intrinsically Disordered Proteins. *Journal of Physical Chemistry B*, 123:3462–3474, 2019.

[429] A. Bandara, A. Panahi, G. A. Pantelopulos, T. Nagai, and J. E. Straub. Exploring the impact of proteins on the line tension of a phase-separating ternary lipid mixture. *The Journal of Chemical Physics*, 150:204702, 2019.

[430] R. S. Taylor, L. X. Dang, and B. C. Garrett. Molecular dynamics simulations of the liquid/vapor interface of SPC/E water. *Journal of Physical Chemistry*, 100:11720–11725, 1996.

[431] G. L. Dignon, W. Zheng, Y. C. Kim, R. B. Best, and J. Mittal. Sequence determinants of protein phase behavior from a coarse-grained model. *PLoS Computational Biology*, 14:1–23, 2018.

[432] S. Park, M. S. Yeom, O. S. Andersen, R. W. Pastor, and W. Im. Quantitative Characterization of Protein–Lipid Interactions by Free Energy Simulation between Binary Bilayers. *Journal of Chemical Theory and Computation*, 15: 6491–6503, 2019.

[433] S. Schott-Verdugo and H. Gohlke. PACKMOL-Memgen: A Simple-To-Use, Generalized Workflow for Membrane-Protein–Lipid-Bilayer System Building. *Journal of Chemical Information and Modeling*, 59:2522–2528, 2019.